SURFACE MODIFICATION AND MULTIPLE EXCITON GENERATION STUDIES

OF PbS NANOPARTICLES

by

JENNIFER M. ZEMKE

A DISSERTATION

Presented to the Department of Chemistry
and the Graduate School of the University of Oregon
in partial fulfillment of the requirements
for the degree of
Doctor of Philosophy

September 2011

DISSERTATION APPROVAL PAGE

Student: Jennifer M. Zemke

Title: Surface Modification and Multiple Exciton Generation Studies of PbS Nanoparticles

This dissertation has been accepted and approved in partial fulfillment of the requirements for the Doctor of Philosophy degree in the Department of Chemistry by:

Dr. Geraldine L. Richmond	Chairperson
Dr. David R. Tyler	Advisor
Dr. Mark C. Lonergan	Member
Dr. Catherine J. Page	Member
Dr. Hailin Wang	Outside Member

and

Kimberly Andrews Espy	Vice President for Research & Innovation/Dean of the Graduate School

Original approval signatures are on file with the University of Oregon Graduate School.

Degree awarded September 2011

DISSERTATION ABSTRACT

Jennifer M. Zemke

Doctor of Philosophy

Department of Chemistry

September 2011

Title: Surface Modification and Multiple Exciton Generation Studies of PbS
Nanoparticles

Approved: _____
David R. Tyler

Solar energy is a green alternative to fossil fuels but solar technologies to date have been plagued by low conversion efficiencies and high input costs making solar power inaccessible to much of the developing world. Semiconductor nanoparticles (NPs) may provide a route to efficient, economical solar devices through a phenomenon called multiple exciton generation (MEG). Through MEG, semiconductor NPs use a high-energy input photon to create more than one exciton (electron-hole pair) per photon absorbed, thereby exhibiting large photoconversion efficiencies.

While MEG has been studied in many NP systems, and we understand some of the factors that affect MEG, a rigorous analysis of the NP-ligand interface with respect to MEG is missing. This dissertation describes how the NP ligand shell directly affects MEG and subsequent charge carrier recombination. Chapter I describes the motivation for studying MEG with respect to NP surface chemistry. Chapter II provides an in-depth overview of the transient absorption experiment used to measure MEG in the NP samples.

Chapter III highlights the effect of oleic acid and sodium 2, 3-dimercaptopropane sulfonate on MEG in PbS NPs. The differences in carrier recombination were accounted for by two differences between these ligands: the coordinating atom and/or the secondary structure of the ligand. Because of these hypotheses, experiments were designed to elucidate the origin of these effects by controlling the NP ligand shell. Chapter IV details a viable synthetic route to thiol and amine-capped PbS NPs using sodium 3-mercaptopropane sulfonate as an intermediate ligand. With the versatile ligand exchange described in Chapter IV, the MEG yield and carrier recombination was investigated for ligands with varying headgroups but the same secondary structure. The correlation of ligand donor atom to MEG is outlined in Chapter V. Finally, Chapter VI discusses the conclusions and future outlook of the research reported in this dissertation.

This dissertation includes previously published and unpublished co-authored material.

CURRICULUM VITAE

NAME OF AUTHOR: Jennifer M. Zemke

GRADUATE AND UNDERGRADUATE SCHOOLS ATTENDED:

University of Oregon, Eugene, OR
Winona State University, Winona, MN

DEGREES AWARDED:

Doctor of Philosophy, Chemistry, 2011, University of Oregon
Master of Science, Chemistry, 2007, University of Oregon
Bachelor of Science, Chemistry, 2005, Winona State University

AREAS OF SPECIAL INTEREST:

Physical chemistry
Materials science
Chemical education
Cheesemaking

PROFESSIONAL EXPERIENCE:

Research Assistant, Department of Chemistry, University of Oregon, Eugene, OR,
    2006 – 2011

Teaching Assistant, Department of Chemistry, University of Oregon, Eugene,
    OR, 2005 – 2008

Research Assistant, Department of Chemistry, Winona State University, Winona,
    MN, 2002 – 2005

Teaching Assistant, Department of Chemistry, Winona State University, Winona,
    MN, 2001 – 2005

GRANTS, AWARDS, AND HONORS:

National Science Foundation IGERT Fellowship, 2009 – 2011

Department of Education GAANN Fellowship, UO Graduate k-12 Fellow 2008

Engineering and Technology Industry Council Fellowship, UO Graduate k-12
    Program 2007

American Institute of Chemists Award, 2005

PUBLICATIONS:

Shultz, G. V.; Zemke, J. M.; Tyler, D. R. *Macromolecules*, **2009**, 42 (20), 7644–
7649.

Zemke, J. M.; Novet, T. E.; Tyler, D. R. *Can. J. Chem.* **2011,** 89 (3), 339-346.

Zemke, J. M.; Daglen, B. C.; Tyler, D. T.; Tachiya, M. *Macromolecules* **2011,**
Accepted for publication.

ACKNOWLEDGMENTS

There are a number of people to whom I owe a great deal of gratitude to for this achievement. First, I would like to thank my advisor, Dr. David Tyler for taking in the stray Pchemist that wandered up to his lab. Without his mentorship and encouragement through the past 6 years, I definitely would not be where I am today. It was an unplanned excursion for me to end up in a predominately synthetic inorganic lab, but Dave welcomed me in and gave me the tools necessary to put this dissertation together. I thank him for his time, scientific input, guidance, patience, and renewal of the laser service contract.

I must give thanks to my wonderful parents, Dennis and Paula, and my little brother, Chris. They need to be thanked first and foremost for putting up with me for the past 28 years and for giving me endless amounts of encouragement and support. It is truly wonderful to be part of such a loving family. Even though I may not say it enough, I love all of you and wish you all the happiness in the world. Oh, I guess I should probably thank Major here under the family envelope as well…too bad he can't read.

I have shared many great conversations, bike rides, walks, hikes, meals, beers, karaoke nights, and plenty of happy hours (no, not *that* kind) with so many people that I just don't know where to start the list of names. You have been my sounding board, my refuge and my sanity. To all of my friends and family, you are all wonderful, and I am better to have known all of you.

I would feel terrible if I didn't thank past and present Tyler lab group members: Dr. Alan Oelkers for leaving me the laser legacy; Dr. Bevin Daglen, Dr. Takiya Ahmed, and Dr. Ginger Shultz for paving the way and making sure I didn't fall to the wayside;

Sarah Brady and Chantal Balesdent for laughter over many things including celery root and amazing dance moves; and Dr. Charlie Swor, Dr. Brandy Fox, Spring Knapp, Emma Downs and Bryan Nell for their support in lab and their friendship outside of lab. Additionally, Patrick Blower, Dr. Stephanie Ota and Dr. Larry Scatena deserve some praise for helping me with oddball laser questions. Dr. David Schut, Dr. Thomas Novet, Stefan Arteaga, Ian Moody, Thomas Allen, Laura McWilliams, Chris Weber and Ben Brinnich have all collaborated with me in one way or another concerning my research. I thank you all for your scientific input.

Lastly, I need to acknowledge all of the educators in my life. This includes teachers and professors in all stages of my life both in and out of school. Teaching and learning are two passions that I would be without had all of you not stepped into my life. Thank you so much for everything you have taught me. I hope I can be as effective in others' lives as you have been in mine.

To my family and friends…you know who you are.

TABLE OF CONTENTS

LIST OF FIGURES

LIST OF TABLES

LIST OF SCHEMES

CHAPTER I

SOLAR ENERGY CONVERSION IN BULK AND CONFINED SEMICONDUCTORS: MULTIPLE EXCITON GENERATION AND THE MANIPULATION OF SEMICONDUCTOR NANOPARTICLES FOR GREEN ENERGY

1.1. INTRODUCTION

The world's energy demands are ever increasing; however, our resources for meeting these demands with our fossil fuel-based energy infrastructure are diminishing rapidly. In fact the world's marketed energy consumption is expected to nearly double from 2007 to the year 2035 with a significant increase in energy consumption due primarily to the energy requirements of developing nations.[1] A breakdown of the current resources for meeting the world's energy needs reveals that roughly 35% of current energy use results from combustion of liquid fuels, namely oil, followed closely by coal an natural gas.[1] It is expected that the dependence on such nonrenewable fuels will decrease over the next few decades due to rising production costs[1]; however, a decrease in fossil fuel use places added pressure on other fuel types to fill the energy gap.

Despite a projected reduction in fossil fuel use there is still an extremely large dependence on petroleum-based fuel. Additionally, petroleum, coal and natural gas reserves are becoming more difficult to mine requiring new technologies to meet projected production values.[1] The fuel obtained from these reserves is also not as clean

1

burning leading to increased concern for problems including increased emission of greenhouse gases such as CO_x, NO_x, and SO_x compounds into our atmosphere. Technologies to solve these problems must be developed in order to cleanly meet the energy needs of our growing planet. With green alternatives to energy in mind, solar energy emerges as one of the greenest technologies available. Sunlight is a ubiquitous energy source for the foreseeable future, thus it stands to reason that solar technology is a heavily pursued avenue of research. In particular, nanomaterials have emerged as likely candidates for enhancing solar conversion while keeping solar devices cost effective due primarily to their high absorbances through the solar spectrum with limited amounts of material.

This chapter serves to introduce traditional solar cells based on bulk semiconductor materials and the inherent limitations surrounding photoconversion in such systems. Additionally, this chapter introduces technologies, namely those based on nanoparticles (NPs) that aim to surpass efficiencies of traditional solar cells. Finally, the manipulation of NPs, namely the NP surface, for optimal device performance is highlighted.

1.2. SOLAR ENERGY CONVERSION IN BULK P-N JUNCTION SOLAR CELLS

The basic idea of a solar cell is simple: convert the sun's energy into electrical energy. The realization of an efficient solar device, however, is a bit more complicated. Although enough of the sun's energy hits the earth in one hour to meet the population's energy requirements for 1 year[2], current devices cannot capture and convert all of this

energy into useable electric energy.[3] With this in mind, it is important to understand the

inherent limitations of solar energy conversion in order to improve upon existing

technologies or to develop new solar technologies that can meet the world's ever

increasing energy demands.

At the most basic level, solar devices are built from semiconductor materials. All

semiconductors have an inherent energy gap (bandgap, E_g), which is a forbidden energy

zone where electrons or holes cannot reside. Because of this band structure, the

promotion of electrons across the bandgap gives rise to carriers that can then contribute to

current in a device. With respect to solar converters, this carrier generation occurs with

the absorption of a photon whose energy is $\geq E_g$. In relation to the idealized solar

spectrum depicted in Figure 1.1, only photons in the shaded region can generate charge

carriers (for a hypothetical semiconductor with bandgap E_g). Contrarily, photons in the

non-shaded region of Figure 1.1 cannot generate charge carriers due to energy

conservation. It is fairly easy to see, then, that one primary issue with solar

photoconversion deals with capturing photons throughout the entire solar spectrum.
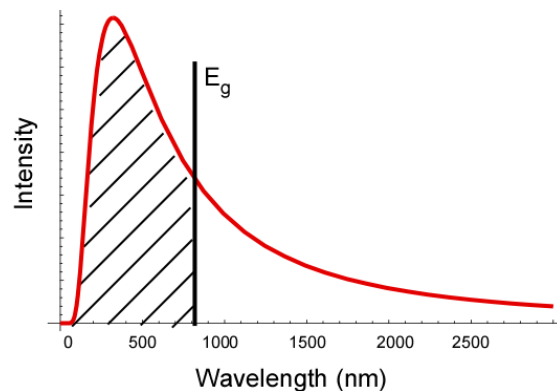
Figure 1.1. Idealized solar spectrum indicating the photons available to create charge
carriers (shaded region) for a semiconductor with a bandgap corresponding to E_g.

With this in mind, it is imperative to discuss further losses incurred in solar

energy conversion. In a bit more detail, a typical solar device relies on a semiconductor

p-n junction. The junction is created by placing differently doped semiconductor

materials together. For clarity, a p-type semiconductor has electron vacancies (positively

biased) and the n-type semiconductor has excess free electrons (negatively biased).[4] This

p-n junction provides a driving force for the much-needed separation of charge carriers in

the device. A general schematic of a working p-n junction solar cell is shown in Figure

1.2. In this figure, the absorption of a photon, typical loss mechanisms, and the function

of the solar cell are outlined. Primary loss mechanisms are phonon emission, or the

relaxation of charge carriers to the band edge and release of energy as heat, and charge

carrier recombination.[4,5] The useable energy for this type of cell is indicated by qV.
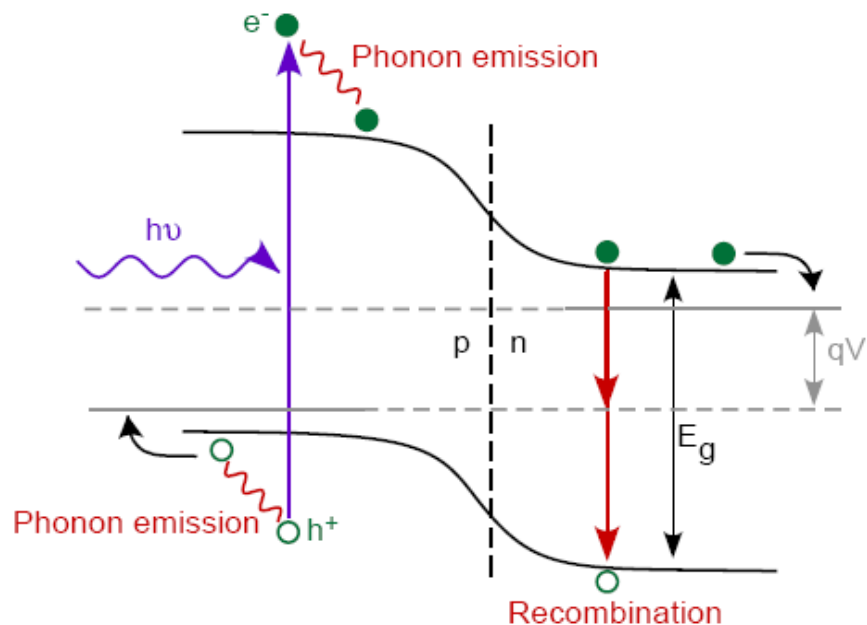
Figure 1.2. General schematic of a p-n junction solar cell showing major energy loss mechanisms (red) and usable photovoltage (qV) upon photoexcitation with above-gap photons.

Already in 1961, William Shockley and Hans Queisser developed a theoretical description of how these loss mechanisms translate to photoconversion efficiency in a single junction solar cell. The Shockley-Queisser limit dictates that the highest efficiency a single junction solar cell may attain under 1 sun's illumination is approximately 33%.[3] This calculation utilized the bandgap of silicon (1.12 eV at 300K[4]) and takes the blackbody radiation of the cell, spectral losses and recombination losses into account. The Shockley-Queisser limit is revered as one of the most important contributions to the field of solar technology and remains an inherent hurdle for current solar technology.

In practice, the current best reported research efficiencies of single junction solar cells lie near 25% with the highest conversion efficiency reported at 26.4% for a GaAs cell.[6] Because developing nations are major contributors to the world's growing energy concerns, energy must be delivered to these nations cheaply?   In order for solar energy to compete with fossil fuel derived energy, the cost-per-watt of a solar device must be fairly low. One way to achieve this is to use cheaper materials (or scale back the amount of materials used in a cell). The other way to achieve this goal is to make solar cells much more efficient.

1.3. BYPASSING THE SHOCKLEY-QUEISSER LIMIT

As described in the previous section, bulk semiconductor solar cells are limited in efficiency to the calculated Shockley-Queisser limit of ~33% because of the associated loss mechanisms involved with the single p-n junction cell.[3] Due to this inherent

photoconversion limitation, the high cost associated with production of these devices and the high demand for marketable green energy alternatives, methods of bypassing the Shockley-Queisser have become increasingly popular topics of research in the past few decades. Described below are a few alternatives to the traditional p-n junction solar cell that are designed to overcome the Shockley-Queisser photoconversion limit.

1.3.1. Infinite Stack Solar Cells

Perhaps the most obvious way to bypass the Shockley-Queisser limit is to create what are called multijunction or infinite stack solar cells. In these cells, individual single junction cells with varying bandgap energies are stacked on top of one another in a single module to better capture all of the photons in the incoming solar spectrum. In this manner, higher energy photons are absorbed first by the largest bandgap materials (Figure 1.3). One can also imagine that if not all generated charge carriers are collected and radiative recombination occurs, the smaller bandgap materials may absorb the emission from the larger bandgap materials leading to increased photoconversion efficiencies. For example, triple junction cells have shown efficiencies of up to 41%.[6] A truly infinite stack solar cell could achieve a theoretical conversion efficiency of nearly 68% of unconcentrated sunlight.[7] Current multijunction cells exist for photovoltaic applications such as space exploration; however, they are inherently quite expensive to produce. For this reason, implementation of such photovoltaic cells on a large scale is not feasible.
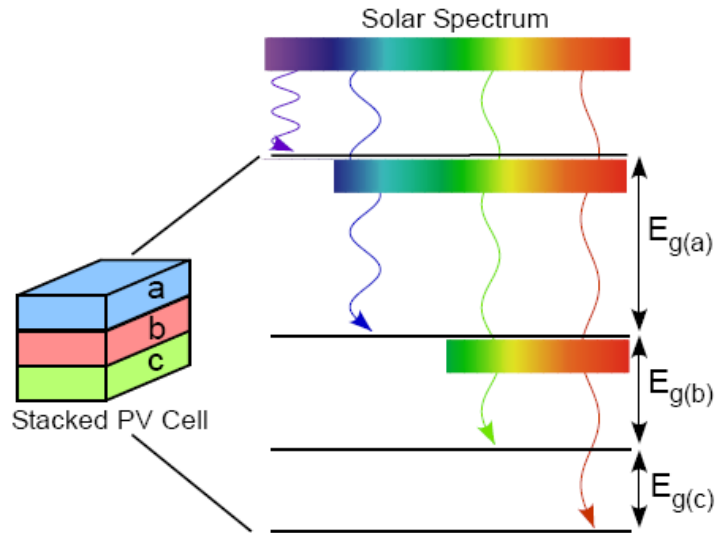
Figure 1.3. Schematic of a stacked solar cell where semiconductors with successively increasing band gap energies are stacked on top of one another allowing for much of the solar spectrum to be absorbed.

1.3.2. Hot Carrier Extraction

Yet another avenue of research determined to bypass the Shockley-Queisser limit deals with extracting charge carriers into a device while they still have an appreciable amount of energy (i.e. before the charge carriers cool to the band edges). This type of process is termed hot carrier extraction. The idea here is that hot, or highly-excited, carriers form a Boltzmann distribution of temperature T, defined by the number of carriers generated and the total energy given to each carrier (note that holes and electrons can be defined by different temperatures).[8] If a high-energy photon is used to excite the carriers an appreciable amount of energy exists in the carrier Boltzmann distribution. This energy is typically unusable due to the rapid cooling of carriers to their respective band edges via collisions of the hot carriers with lattice atoms.[9] If the carriers could be

extracted without thermal losses, however, a hot carrier device could theoretically exhibit photoconversion efficiencies of up to 67%.[10]

While the idea of extracting hot carriers in solar cells has been around since the early 1980s[10], little work other than a few theoretical and dynamical studies had been pursued in the area of hot carrier cells.[9,11] The small distances needed for the carriers to travel to minimize cooling require materials with negligible dimensions. Because of this requirement, the device architecture envisioned for a hot carrier cell typically uses a quantum dot (or nanoparticle, NP) to act as an effective energy filter. When the NP is placed next to an electrical contact in the device as in Figure 1.4, the hot carriers would be able to pass through the NP energy filter without cooling resulting in higher photovoltages. Because this requires precise control in synthesizing NPs and coupling nanoscale and mesoscale subunits, the technology needed to pursue such a device had been lacking when the idea was first proposed. Thus hot carrier cells were abandoned in favor of other ideas. However, with current advances in the synthesis and characterization of nanomaterials and their integration into working devices, the idea of hot carrier solar cells is experiencing a revival of interest in the research community.[12-15]
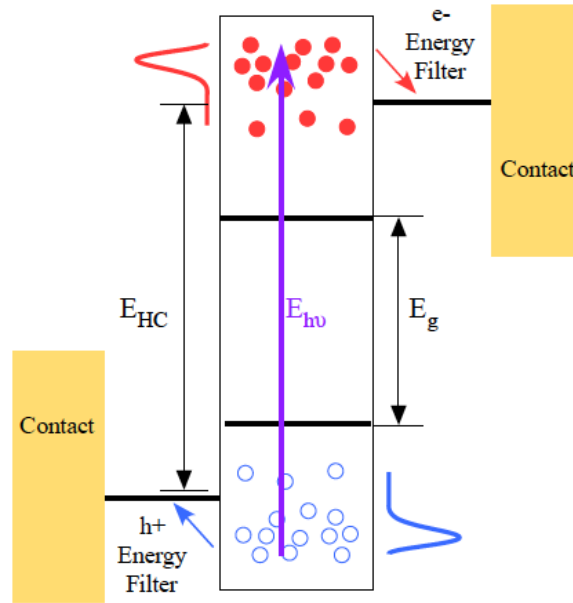
Figure 1.4. Energy structure of a hot carrier solar cell where a selective energy filter allows energetic electrons and holes to pass to the contacts without cooling.

1.4. MULTIPLE EXCITON GENERATION

The methods described above are feasible routes to bypassing the inherent limitations of single junction solar converters; however, the main phenomenon discussed in this dissertation surrounds the implementation of nanomaterials as solar energy harvesters. Nanomaterials have received an incredible amount of attention for their propensity to be extremely efficient and low cost solar materials. This propensity for enhanced performance in solar cells stems primarily from the phenomenon called multiple exciton generation (MEG) whereby a single photon can create more than one electron-hole pair (exciton) within the nanomaterial leading to increased photocurrent.[5,16-18]

9

In particular, the MEG process is proposed to be highly efficient in semiconductor nanoparticles, NPs. MEG arises from the properties brought on by quantum confinement in semiconductor NPs. Quantum confinement in NPs is manifested primarily in the appearance of discrete energy levels and increased energy level spacing as the dimensions of a crystal become increasingly smaller.[19] Figure 1.5 shows the relative energy diagrams for bulk semiconductors, semiconductor NPs and a general molecule.
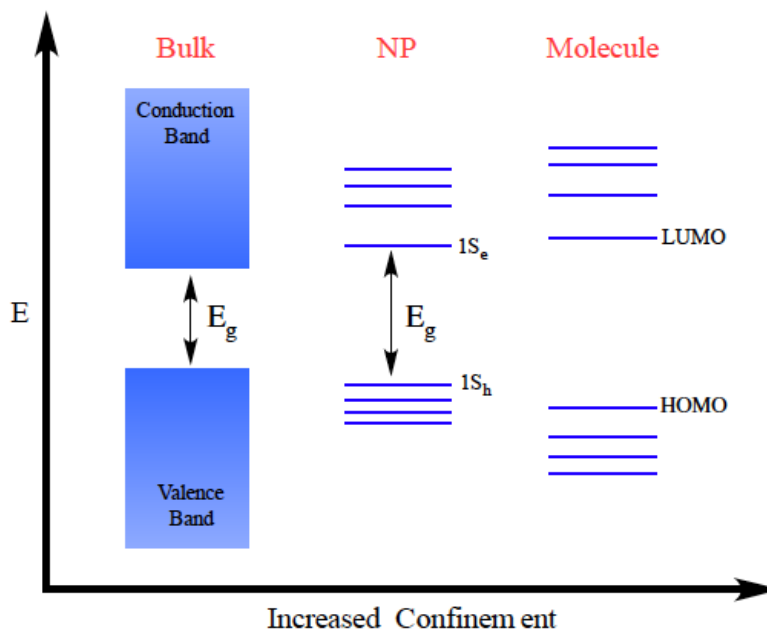
Figure 1.5. Schematic of the energy level diagrams of materials as a function of increased confinement.

Before discussing MEG further, it is perhaps easier to discuss an analogous process that occurs in bulk semiconductors. It has been shown in bulk semiconductors that excess charge carrier generation occurs through a process called impact ionization (II). During II, there is a transfer of energy from a hot electron or hole as it cools to the band edge, which promotes another carrier across the bandgap. It is important to note,

10

however, that the II process is fairly inefficient in bulk semiconductors. II also occurs at a higher energy threshold ($> 5E_g$[20]) than has been seen for semiconductor nanomaterials. The excess energy required to observe II in bulk structures is presumably due to the necessity of momentum conservation in the bulk material. Figure 1.6 shows the II process using a parabolic model to approximate the valence and conduction band structures.
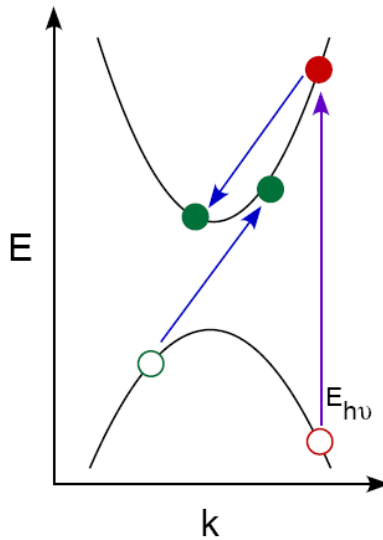
Figure 1.6.   Impact ionization in bulk semiconductors showing conservation of momentum (k).

While II is the accepted mechanism of excess carrier generation in bulk systems, the mechanism of MEG has undergone some scrutiny. II was the original proposed mechanism for the enhancement of MEG seen in NPs. This stems from the fact that II relies on the cooling of carriers to the band edge resulting in a transfer of energy to another carrier, promoting it across the bandgap. In NPs, it was assumed that because of the lack of coupling to lattice phonons in NPs, the cooling of carriers would result in the transfer of larger packets of discrete amounts of energy translating into a slower rate of

hot electron (or hole) cooling.[16,20] Additionally, conservation of momentum is relaxed in NPs. These effects coupled with the strong Coulomb interaction between electrons and holes in semiconductor NPs should lead to enhancements of Auger-type processes including II, the inverse of Auger recombination.

While II seemed to be an efficient mechanism for MEG, experiments performed by Klimov, *et. Al.* showed that the development of multiexcitons occurs nearly instantaneously.[18,21,22] These population build-up experiments on CdSe and PbSe NPs showed that the evolution of biexcitons occurred within the development of the laser pulse. Because of the instantaneous development of multiexcitons, Klimov *et. Al.* proposed an alternative mechanism to MEG termed carrier multiplication (CM).[21,23] Carrier multiplication is derived from the coupling of a highly excited, virtual single exciton state to a biexciton state. Figure 1.7 shows the typical carrier processes for bulk semiconductors and semiconductor NPs under CM with excitation energies $>2E_g$. Note that coupling to lattice phonons in the bulk systems results in a loss of excess carrier energy as heat; however, in the semiconductor NP systems, the excess carrier energy results in the generation of excess charge carriers. While the mechanism of MEG is still somewhat disputed (and termed accordingly), the existence of MEG at lower excitation energies than in the bulk has been repeatedly observed.[21,24,25] Whether the mechanism for MEG is II or CM, the enhancement of MEG in NP systems over bulk systems likely stems specifically from the larger Coulomb interaction in NPs and the relaxation of momentum conservation and can still have direct application to the future of photovoltaic devices.

a) Bulk Semiconductor
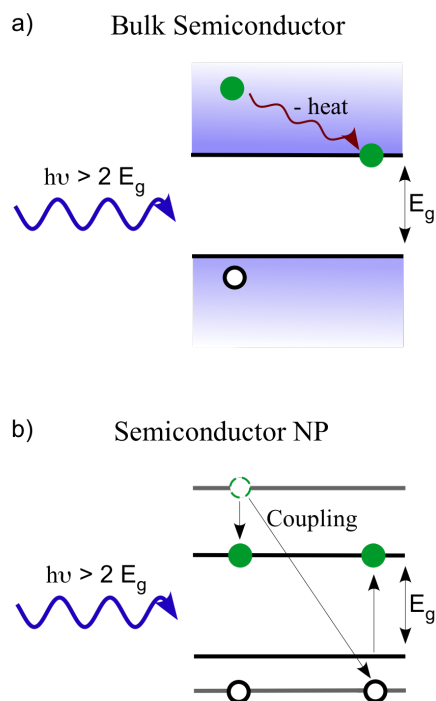
b) Semiconductor NP

Figure 1.7. Excitation of carriers in bulk semiconductors (a) and in a semiconductor NP (b). In bulk semiconductors, excess energy is lost as heat by excitation of lattice phonons; however, in a semiconductor NP, that excess energy is translated into a second exciton (MEG). Bulk semiconductors are capable of generating excess charge carriers but at typically higher energy costs than in semiconductor NPs.

1.5. PARAMETERS AFFECTING MEG IN NP SYSTEMS

Because of the enhanced generation of excess charge carriers and the implications of MEG to solar energy conversion, MEG has been studied in a variety of NP systems. While there have been many reports of efficient MEG in NPs, these reports are not necessarily consistent. Differences in the MEG behavior of various NP systems can be accounted for by a number of parameters providing some clear trends in MEG. For

example, the size, shape, composition, and surface chemistry of NPs all have the capacity to affect MEG.

Chemical composition and surface quality of the NPs are perhaps the two most widely investigated parameters affecting MEG. For example, MEG has been measured to varying degrees in various types of NPs including CdS, CdSe, and CdTe NPs as well as the analogous Pb-based NP structures.[26-37] MEG has even been investigated in InAs NPs though inconsistencies exist for these types of NPs.[38,39] For example, core/shell particles of InAs/ZnSe have shown appreciable MEG yields with a low MEG energy threshold of $2E_g$ by Schaller, Pietryga and Klimov[40], whereas core/shell/shell nanostructures of InAs/CdSe/ZnSe structures have exhibited negligible carrier multiplication yields.[41] These discrepancies have been speculated to arise from differences in the overlap of single and biexciton states high above the bandgap that could be altered by the presence of shells of varying thicknesses on the NPs.[41] Lastly and most recently, MEG has even been reported in single wall carbon nanotubes giving credence to the generality of enhanced MEG in nanostructures.[42]

Lastly, due to the large surface-to-volume ratio inherent to NPs, it is hypothesized that the NP surface plays a significant role in the electron dynamics of the system.[43,44] Thus, a key component in designing NP-based solar cells is understanding the role of the stabilizing ligand shell. A few studies have begun to elucidate the role of the NP surface with regard to MEG.[26,37,45] Provided that electron dynamics are not influenced by a large density of surface trap states[45], different surface treatments of PbSe NP films with various ligands and solvents have yielded very different recombination dynamics and MEG efficiencies.[37] Additionally, as was mentioned previously, the addition of a shell onto

14

core NPs shows varying degrees of MEG signature strengths. Recently, Tyagi and Kambhampati have shown that the addition of a ZnS shell onto CdSe NPs yields a dramatic decrease in the biexciton signature of the NPs.[46] The authors also uncovered that phototreated CdSe NPs show enhanced MEG-type signatures over untreated CdSe NPs. They attribute their results to the presence of surface trap states on the NPs owing the suppressed (true) MEG behavior of the ZnS-capped NPs followed by the untreated NPs to the better passivation of the CdSe core.[46]

1.6. TRADITIONAL ANALYSIS OF MEG

In order to measure MEG, ultrafast laser measurements are used to probe time-dependent exciton dynamics. Transient absorption (TA), time-resolved terahertz spectroscopy (TRTS) and time-resolved photoluminescence (TRPL) have been used to probe the MEG process in semiconductor NPs. The basis for measurement of MEG in the TA technique is to pump the NP samples (i.e. induce a photobleach of the 1st exciton state) and probe the time-dependent recovery of the ground state.

For the TA experiments in this dissertation, the treatment of the data was adopted from the analysis of Ellingson, *et. Al.*[36] Raw kinetic data is obtained for a set of NPs over a variety of input pump fluences (# of photons/unit area). These kinetic traces are obtained both above and below the energy threshold of MEG in the NPs, which is based on the pump photon energies. Multiexciton behavior can be seen when the NPs are forced to absorb > 1 photon (with sub-threshold excitation energies) and in the case of the absorption of one above-threshold photon. Because the dynamics of multiphoton

absorption at low input energies are more straight-forward than in the case of MEG, the sub-threshold experiments are used to model the exciton dynamics of the system. Figure 1.8 shows an idealized set of kinetic traces with varying pump fluences. Note that as the pump fluence increases, the transient signal also increases consistent with a larger photobleach response of the 1S exciton state.
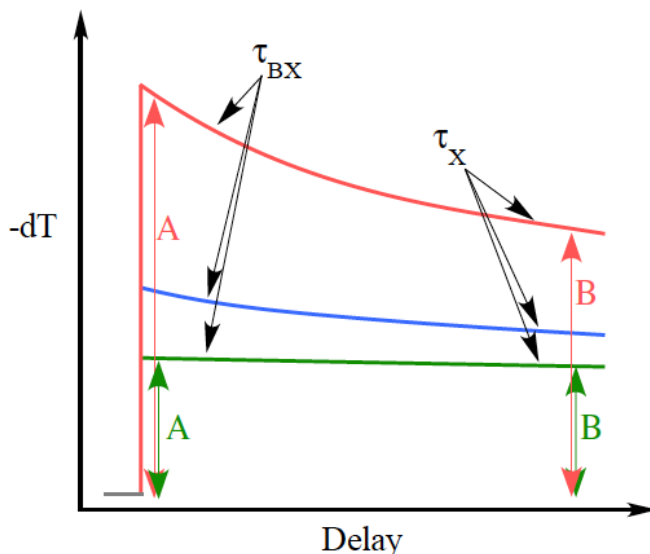
Figure 1.8. Idealized kinetic traces and relevant parameters of the sub-threshold excitation of generalized semiconductor NPs. Three traces are depicted as a function of varying pump fluence (green < blue < red).

For simplification, Figure 1.8 shows three traces and depicts the decay of a biexciton and a single exciton that include Auger recombination. The decay rates for these processes are independent of pump fluence and are thus extracted from the transients as global parameters. The decay rate of a biexciton is described by τ_{BX} while the much longer-lived single exciton decay rate is given by τ_X. The physical description of these processes will be discussed later. In addition to extracting time constants for

16

exciton dynamics, the amplitudes of the transients provide necessary information regarding absolute populations of multi and single excitons (A and B for each trace in Figure 1.8).   From Figure 1.8 it is clear that under low fluence sub-MEG threshold excitation that flat, single exciton dynamics are observed. However, as the fluence is increased, NPs within the excitation volume experience a higher probability of absorbing multiple photons from the excitation pulse. The probability of multi-photon absorption leading to the generation of multiple excitons follows Poisson statistics and is described by Equations 1 and 2. In Equations 1 and 2, P is the probability of creating n excitons, N_{abs} is the number of photons absorbed per NP, J_{pump} is the pump photon fluence and σ is the NP absorption cross section.

$$P = \frac{N_{abs}^{n}}{n!} e^{-N_{abs}} \qquad\qquad 1$$

$$N_{abs} = J_{pump} \cdot \sigma \qquad\qquad 2$$

Because multi-photon absorption translates into the creation of more than one exciton, the below threshold traces can be used to extract the relevant time constants for single excitons, biexcitons, triexcitons, etc… depending on the input photon fluence. For reference, a typical single exciton recombination rate is on the order of 100 ns whereas multi excitons decay faster (on the order of 10s or 100s of ps). The procedure for fitting the decay curves follows a physical model where excitons recombine through an Auger-type process in a sequential order as shown in Figure 1.9
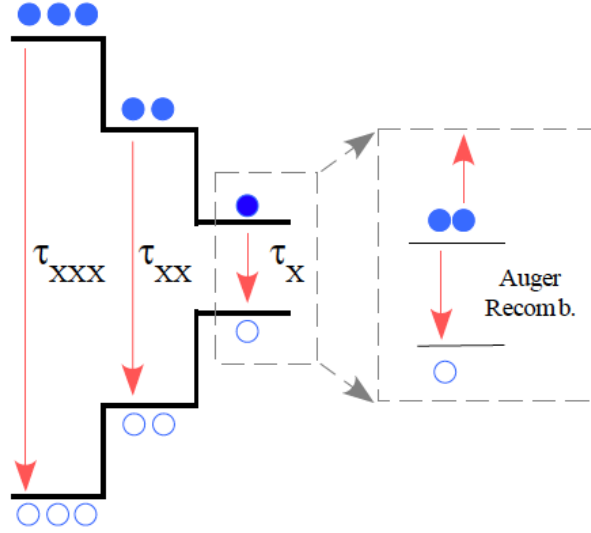
Figure 1.9.   Stepwise recombination of multiexcitons and recombination of single excitons through an Auger recombination process.   Multiexcitons recombine on timescales that are much shorter than that of the longer-lived recombination of single excitons.

Because of the stepwise recombination of multiexcitons and the rapid decay of multiple excitons versus single excitons (the limit of $\tau_{n+1} \ll \tau_n$), the decay curves can be fit to a series of exponential functions (Equation 3).[5] In Equation 3, A_n denotes the amplitudes associated with the generation of n excitons and τ_n reflects the time constant for decay of the nth exciton.

$$f(t) = \sum_{n=1}^{\infty} A_n \exp\left(-\frac{t}{\tau_n}\right) \qquad\qquad 3$$

The amplitudes, A_n, in Equation 3 are proportional to the population of generated excitons in the NP sample and follow Poisson statistics as stated previously. Thus the

amplitudes are the Poisson amplitudes (P as in equation 1 above) for the measurement of sub-MEG threshold exciton populations.

In the case of MEG measurements, however, the amplitudes of the transients at early times are no longer Poissonian. Added contributions to the amplitudes for the generation of multiple excitons can be used to extract the efficiency of MEG (or MEG yields) for samples of NPs. For a single exciton excited under MEG conditions, the amplitude A_1 is still the Poisson amplitude, P_1. Amplitudes for generated multiexcitons (n > 1) carry excess contribution due to the probability of a highly excited electron or hole causing the excitation of excess charge carriers. The amplitudes with MEG probabilities for biexcitons (n=2) and triexcitons (n=3) generated in the energy range of $3E_g < h\omega < 4E_g$ (the pump energy regime of the experiments in this dissertation) are reflected in Equations 4 and 5.[5,36]

$$A_2 = \sum_{n=1}^{\infty} P(n) + P(1)*\left(2\eta(1-\eta) + \eta^2\right) \qquad\qquad 4$$

$$A_3 = \sum_{n=1}^{\infty} P(n) + P(2)*\sum_{j=1}^{4} \eta^j(1-\eta)^{4-j}\left({}_4C_j\right) \qquad\qquad 5$$

The probability of an exciton producing an additional exciton through the MEG process is defined as η in Equations 4 and 5. Additionally, ${}_4C_j$ is a function of the form ${}_nC_r = n!/(r!(n-r)!)$. The above amplitude equations are derived from accounting for all of the MEG events that could occur for a NP absorbing one or photons with energies between 3 and $4E_g$ and have been described in detail elsewhere.[36] The quantum yield (QY) for the $3E_g < h\omega < 4E_g$ pump energy regime is then given by Equation 6.

19

$$QY = 1 + 2\eta \qquad\qquad\qquad 6$$

Perhaps a more convenient method of obtaining the MEG QY is that of modeling the ratios of the populations of excitons at early and late times (A/B) as a function of input pump fluence. In this case, early times are typically 2-5 ps and late times are ~1500 ps or after the decay of all other processes has transpired. Described by Ellingson, *et. Al,* the relationship for this ratio is given by Equation 7.

$$\frac{A}{B} = \frac{J_{pump}\sigma_{pump}\delta QY}{\left(1 - \exp\left(-J_{pump}\sigma_{pump}\right)\right)} \qquad\qquad 7$$

In Equation 7, J_{pump} and σ_{pump} are the input pump fluence and the absorption cross section per NP at the pump wavelength respectively. δ is a parameter that takes into account the decay of the single exciton, and the overall MEG QY is determined by results from both sub-MEG threshold and above threshold measurements. The absolute MEG yield is a consequence of extrapolating the curves given by and taking the ratio of the QYs as determined by Equation 7 at nearly zero photon fluences.

The overall MEG QY and the time constants of the single and multiexciton recombination events are parameters that can be used as benchmarks to tune the NPs for optimal device performance. More specifically, enhancing the MEG yield while generating long-lived biexcitons could lead to appreciably enhanced photocurrents in NP-based devices.

1.7. MODIFICATIONS TO MEG MEASUREMENTS AND ANALYSIS

Recently, there has been some controversy over MEG in nanoparticle systems. In particular, it has been argued that MEG is less efficient than what was previously reported.[27,30,31,41] For example, a re-examination of CdSe and CdTe NPs led to the conclusion that MEG efficiency is negligible in these systems, contrary to prior results and contrary to the general idea that MEG is enhanced in quantum confined systems.[31]

Differences in apparent MEG efficiencies have been reported in different preparative batches of supposedly identical nanoparticles.[28,47] Because of this, controversy has developed over the existence of photocharging of the NPs leading to a misinterpretation of true MEG yields; however, stirring of the solutions to sample a fresh volume of NPs with each laser pulse greatly reduces the probability of photoionization and allows for the observation of true MEG yields.[47] Additionally, the extent of ligand coverage and oxidation of a NP surface may lead to increased carrier trapping, thus requiring additional considerations in analyzing the carrier dynamics.[28]

The original analysis of MEG assumes that any change in amplitude for a TA or TRPL trace is strictly due to the generation or recombination of excitons and the probability of an electron or hole generating an extra charge carrier. While this is an ideal assumption, other processes can lead to the appearance of false MEG-type signatures in the kinetic traces requiring more careful experimental methods or a more rigorous analysis of MEG. Trapping of an electron or hole by a surface state can lead to a false interpretation of MEG yields.[46,48] Additionally, as mentioned above, photocharging of the NP samples or oxidation of the NP surface can lead to overestimation of MEG

yields if not properly accounted for.[28,33,47,49] An illustration of how trapping and

photocharging affect MEG is shown in Figure 1.10.
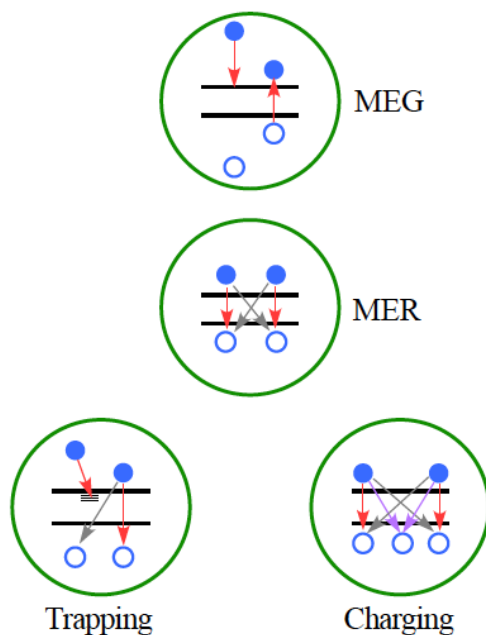
Figure 1.10. Possible mechanisms of MEG (a) and recombination (MER) in a NP with an uncharged biexciton (b), in the case of electron trapping (c) and with a charged biexciton (d).

When an electron or hole is trapped by a surface state, it is no longer available in

the traditional ground or excited state to probe in a TA experiment (or to radiatively

recombine in a TPL experiment). Because of this, the probe signal in a TA experiment

for a trapped electron (or hole) overestimates the actual contribution of multiexcitons to

the short time amplitudes of the kinetic traces. In a similar manner, long-lived

photocharging can lead to the misinterpretation of MEG yields as has been observed.[33]

The above scenarios lead to inconsistencies in measuring the true MEG yields of

NP systems; however, experimental considerations and a modification to the traditional

MEG analysis can be used to uncover true MEG yields. In the case of experimental

considerations, it has been shown that vigorously stirring or spinning the NPs during the TA or TRPL experiments is necessary to remove unwanted effects due to photocharging.[33] Presumably, spinning or stirring the samples results in a "refreshment" of the sample volume with each laser shot. As long as each laser pulse is sampling a new volume of NPs, transient signatures due to long-lived NP charging (typically seen after multiple laser shots) is severely reduced or eliminated. In fact, it has been shown that saturation of photocharging occurs within 10% of the NP sample volume, thus if 10% of the sample volume is refreshed between laser shots, the probability of photocharging signatures arising in the TA or TPL traces drops to zero.[33]

Even though simple experimental precautions can reduce or eliminate processes leading to false MEG signatures, adjustments to the analysis of MEG yields can still be made to ensure the extraction of true MEG yields. For example, if trapping is seen for low fluence excitation in sub-threshold experiments, a trapping factor may be added into the analysis during the fitting routine. In a recent publication outlining the effect of oxygen adsorption onto the surface of NPs, an increase in surface-mediated charge trapping was observed.[48] However, by accounting for this trapping factor, reasonable and comparable MEG yields were obtained between samples exposed to oxygen and those kept in inert atmosphere.

1.8. SURFACE MODIFICATION OF NPs

1.8.1. Ligand Exchange on Metal and Semiconductor NPs

While the surface of a NP is important to the optical and electronic properties of the NP, systematically modifying the surface of a NP is not trivial. It has been hypothesized that ligands on NPs exist in an equilibrium with their bound and unbound forms. Thus, by Le Chatelier's principle, reaction conditions with excess desired ligand in solution should promote ligand exchange. While this has been observed, there are some subtle nuances of NP ligand exchanges that need to be discussed. For this reason, a brief overview of some ligand exchanges of both metal and semiconductor NPs is presented here.

A typical route of NP ligand exchange involves the use of NPs capped with phosphines or phosphine oxides (trioctylphosphine, TOP and trioctylphosphine oxide, TOPO), which are fairly labile ligands. Exchanging these ligands for tighter binding moieties has yielded some success. For example, in a recent JACS paper, Knowles, *et. Al.* used phosphine-capped CdSe NPs for ligand exchange with various *p*-substituted aniline ligands. Although amine terminated ligands also bind relatively weakly to metals, excess ligand in solution promotes the coordination of the desired aniline to the CdSe NP. The ligand equilibrium of the exchange reactions was monitored by photoluminescence (PL) spectroscopy. The reactions were assumed to be at equilibrium when the PL intensities remained steady after roughly 24 hours. To this avail, the NPs were never

isolated for characterization regarding the ligand exchange but the extent of ligand exchange was thought to correspond to the changes seen in PL intensity.[50]

A versatile ligand exchange route was presented by Dubois, *et. Al.* for CdSe NPs where carbon disulfide was added to various amine ligands forming dithiocarbamate ligand precursors for exchange reactions. Again, this exchange procedure used TOPO-capped CdSe as starting materials whereby the bidentate binding of the dithiocarbamate ligands can easily displace the TOPO ligands. A variety of capping agents bearing secondary functionalities (carboxylic acids, aromatic pendant groups, alkyl chains) were attached to the CdSe particles using this synthetic scheme, but the exchange can only access ligands bound through the dithiocarbamate headgroup. Thus exchanging the coordinating atom, which could prove useful in device applications, is not feasible through this route.[51]

Both homometallic and heterometallic NPs have been subjected to ligand exchanges.[52-54] In one instance, triphenylphosphine (TPP)-capped gold NPs were exchanged for a variety of thiol ligands. In this case, the phosphine was also fairly labile, and the exchange reactions exploited the strong binding of sulfur to gold. Monitoring of the ^{31}P NMR shifts indicated the release of TPP during exchange. Both monophasic and biphasic reaction conditions were used for the exchange of the variety of thiols in this study. It should be noted that large excesses of thiol ligand promoted the formation of disulfides in this investigation. Additionally, the pH of the biphasic reactions had to be thoroughly controlled (kept near neutral) to avoid the decomposition of the Au-TPP precursor NPs or excessive disulfide formation.[53]

Lastly, in some cases, ligand exchange reactions seem to require harsh reaction conditions for the exchange to occur. For example, ligand exchanges on hydrophobic CdSe/ZnS core-shell NPs for various thioalkyl acid ligands were sonicated and refluxed in excess deprotonated ligand or run under biphasic conditions at elevated temperatures (62 °C). While the reaction conditions seem inordinately harsh in this instance, ligand exchange did occur as indicated by changes in solubility, photoluminescence lifetimes and steady-state photoluminescence shifts.[55]

1.8.2. Ligand Exchanges on PbX NPs

In cases of ligand exchange with Pb-based NPs, literature precedent for versatile methods of ligand exchange is even more limited. In particular very few solution-phase reactions with a variety of ligands have been attempted. Because PbS and PbSe NPs are attractive for solid-state device applications, many ligand exchange reactions thus far have been on films of NPs. For example, in one instance, oleic acid was removed from films of PbSe NPs by various surface treatments. Ethanedithiol, hydrazine, and methylamine in various solvents were used to presumably displace the oleic acid from the films. A measure of the ligand displacement on these films manifested itself in changes in photoluminescence quantum yields and in measured interparticle distances. Presumably, the removal of oleic acid and the substitution of a short chain ligand results in decreasing the distance between NPs. The results of this investigation showed that there was an appreciable difference in MEG in these variously treated NP films. Thus

this study proved that the surface of NPs is important when considering NPs for solar devices, but the solid-state exchange is not optimal for industrial scale-up.[56]

In another ligand exchange on PbS NPs, reactions with mercaptopropionic acid (MPA) yielded MPA-capped NPs for examination of multiple exciton collection (MEC). In this instance, Sambur *et. Al.* used dried PbS NPs capped with oleic acid. The exchange occurred with a large excess of mercaptopropionic acid that had been deprotonated in base. The reaction products of this exchange were trapped onto a TiO_2 substrate via the carboxylic acid functionality of the ligand. The ligand exchanged NP films produced from this method showed the first reports of MEC where photocurrent efficiencies exceeded 100% indicating the contribution of biexcitons to the photocurrent. While this is an extraordinary result, the ligand exchange procedure requires the trapping of NPs onto the TiO_2 substrate in order to avoid ripening of the NPs by the harsh reaction conditions (high pH).[57]

Solution-phase ligand exchanges reactions have yielded solution processable PbX NPs. Results of these exchanges are limited to octylamine (or shorter chain amines) and sodium salts of mercaptopropane sulfonates. For exchange with shorter chain amines, dried NPs were suspended in large excesses of ligand (sometimes neat) and allowed to stir at room temperature and at elevated temperatures to promote the ligand exchange. For 3-mercaptopropane sulfonate and 2, 3-dimercaptopropane sulfonate, however, biphasic reactions were run which resulted in the visible migration of the NPs between phases and more facile characterization of the exchange.[58]

27

1.9. CONCLUSIONS

This chapter serves as an introduction to the process of multiple exciton generation (MEG) in nanoparticle (NP) systems and the relevance of MEG to current energy technologies. The motivation behind studying MEG in various NP systems arises from the need to find greener alternatives to meeting the world's energy demands. While solar technology is one of the greenest alternatives to a fossil fuel-based energy infrastructure, there are inherent limitations in converting the sun's energy into useable electrical energy. Such limitations, namely the Shockley-Queisser limit can be theoretically bypassed by employing the process of MEG in a solar device. This is accomplished by creating excess charge carriers per photon absorbed, the fundamental outcome of MEG.

While MEG is of considerable practical use to the solar industry, there are many experimental factors that can contribute to MEG yields and to carrier recombination dynamics. This chapter discusses the parameters that affect MEG leading to the conclusion that one important parameter to consider when envisioning NP-based solar devices is the NP surface (typically a ligand shell).

In addition to giving an overview of MEG and the experimental factors that influence MEG, the traditional measurements and analyses of MEG were discussed at length in order to illuminate the data analysis used in Chapters III and V of this dissertation regarding NP ligand effects on MEG and subsequent multiple exciton recombination (MER). These traditional analyses have been rigorously challenged in recent publications in light of some controversy surrounding inconsistent reports of MEG

primarily due to factors that contribute to the overestimation of MEG yields. Because of this controversy, modifications to the analysis of MEG and the experimental considerations that are key to understanding the true nature of MEG were discussed. Finally, a brief overview of the current state of semiconductor NP surface modification was presented. This serves to indicate the intricacies of NP ligand exchange and characterization while providing significant background for Chapter IV in this dissertation.

Before experimental results are presented in this dissertation, a second introductory chapter is necessary. The next chapter, Chapter II, provides a detailed description of the transient absorption experiment used to collect all of the time-resolved MEG data in Chapter III and Chapter V.

The material in Chapters III, IV and V is coauthored with Dr. David Tyler who was my advisor during those investigations. Additionally, Chapter III was coauthored with Dr. Thomas Novet who provided starting materials for the investigation. The data and results in Chapter III have been previously published in Volume 89 of the *Canadian Journal of Chemistry*, and the material is represented herein with permission from the NRC Research Press. Lastly, the material in Appendix A was coauthored with Dr. David Tyler, Dr. Bevin Daglen and Dr. Masanori Tachiya. The manuscript derived from the Appendix has been submitted to the journal *Macromolecules*.

CHAPTER II

EXPERIMENTAL DESIGN: A TRANSIENT ABSORPTION EXPERIMENT TO DETERMINE EXCITON DYNAMICS IN SEMICONDUCTOR NANOPARTICLES

2.1. INTRODUCTION

Spectroscopy is a powerful technique used in the investigation of chemical and physical phenomena where there is an interaction of photons with matter. Lasers were developed as useable light sources in the 1960s[1], and since then, laser spectroscopy has become an invaluable route to elucidate electronic, vibrational, structural and dynamical properties of chemical systems.[2-4] The first continuous wave lasers provided scientists with a facile method to probe fundamental interactions of light with matter; moreover, by the mid 1990s, the development of reliable pulsed laser systems opened up an entirely new avenue of spectroscopy.[2,5-9] With pulses of laser light shorter than 10^{-12} seconds, scientists were able to probe the dynamics of transient chemical species and for all intensive purposes "watch" chemical and physical events on the ultrafast timescale.[2,4,10] In particular, pump-probe spectroscopy has been developed as a powerful technique to determine the dynamical behavior of many systems with a time resolution of less than 50 fs.[5,11] This chapter outlines the principles behind pulsed laser sources and discusses the experimental design and considerations used in the remainder of this dissertation.

2.2. LASER SOURCES

2.2.1. The Laser Cavity

A functional laser cavity relies upon the process of stimulated emission—a fundamental interaction of photons with matter. In discussing fundamental interactions between light and matter, there are a few processes to consider. When incident radiation upon matter results in the transfer of light energy to an electron, the result is absorption. Incidentally, when that electron loses its absorbed energy and produces a corresponding photon, that process is termed spontaneous emission. The process of stimulated emission is much like spontaneous emission; however, in this case, an already excited electron responds to the interaction of another photon. These three processes are shown in Figure 2.1.
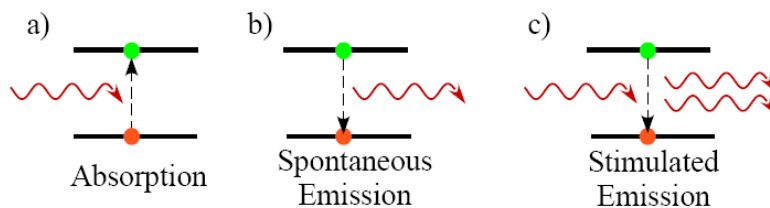
Figure 2.1. Three processes describing the fundamental interactions of light with matter: a) absorption b) spontaneous emission and c) stimulated emission.

Laser emission is the product of taking advantage of stimulated emission. This is accomplished by creating a cascading effect in a laser medium with a metastable excited state and a population inversion (> 50% excited state electrons) resulting in an amplified, collimated, coherent and monochromatic light source.[12] A generalized laser cavity can be

broken down into three main components: input radiation, a gain medium, and a resonant cavity.[12] For the laser to function as desired, the input radiation and gain medium work together to produce stimulated emission. In its simplest form, the resonant cavity is defined by two components: a high reflector (end mirror) and a partially reflective mirror (output coupler).[12] Stimulated emission generated in the gain medium is allowed to repeatedly propagate through the gain medium building power with each pass until the amplification process reaches the saturation point of the output coupler, a process described in Figure 2.2.[12]
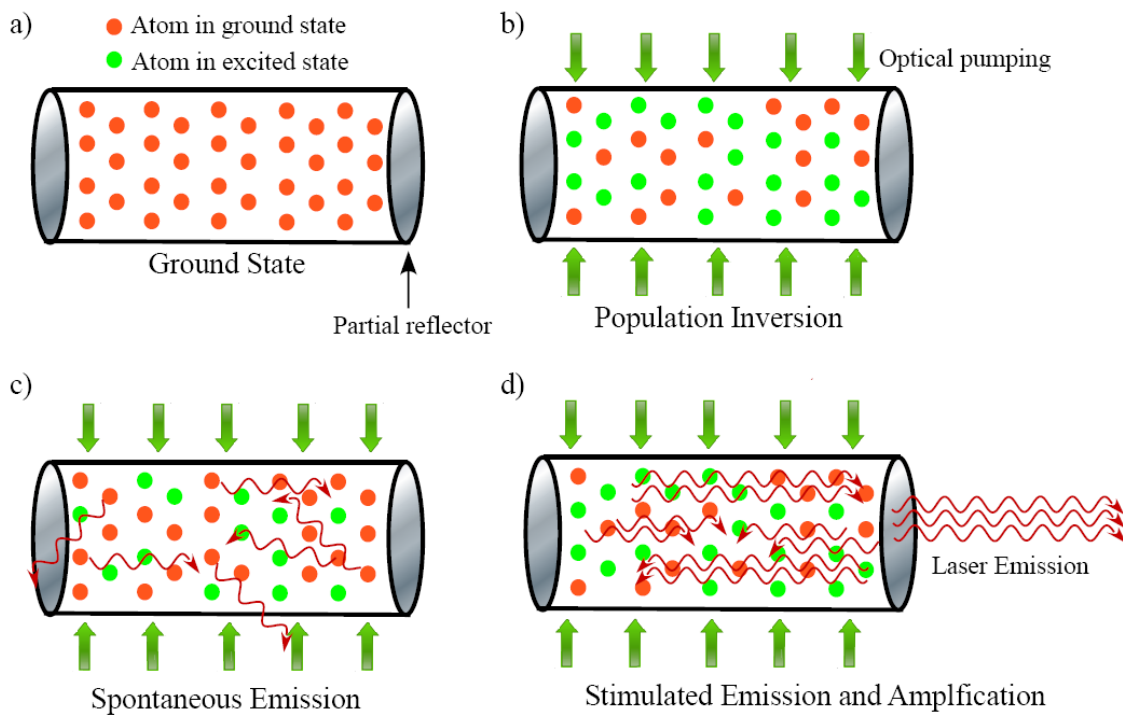
Figure 2.2. Example of a simple laser cavity showing the laser medium in the ground state (a), population inversion through optical excitation of the laser media (b), spontaneous emission (c) and stimulated emission with amplification (d).

2.2.2. The Ti:Sapphire Laser

There are numerous types of laser media available spanning wavelengths across the electromagnetic spectrum.[1,12,13] Laser media exist in all states of matter including liquid phase dye-sensitized lasers, gas phase lasers such as the classic helium-neon laser and solid state laser media including the Ti:Sapphire (or Ti:Sapph) laser to be described in detail here.[1,12-17] All types of laser media have a few things in common; however, the properties of a Ti:Sapph crystal make the Ti:Sapph laser a very versatile light source.

Ti:Sapphire crystals consist of a host crystal of Al_2O_3 where a small amount of the Al^{3+} ions are substituted for Ti^{3+} ions. In considering laser media, one advantageous property of Ti:Sapph crystals is that the Ti^{3+} ions impart a broad absorption spectrum through the blue-green wavelengths on the Ti:Sapph crystal (Figure 2.3).[13,18] This allows for the Ti:Sapph rod to be pumped at a number of optical wavelengths that correspond well to various commercially available lasers such as frequency-doubled Nd:YAG (Nd^{3+} doped yttrium aluminum garnett), Nd:YVO$_4$ (Nd^{3+} doped yttrium vanadate) and Nd:YLF (Nd^{3+} doped yttrium lithium fluoride) lasers with center frequencies near 532 nm.[17,16] Additionally, the emission profile for Ti:Sapph is broad allowing for a considerable amount of tunability in the near-infrared (NIR) from 650 nm to 1100 nm, a bandwidth of roughly 128 THz, with an optimal working efficiency near 800 nm.
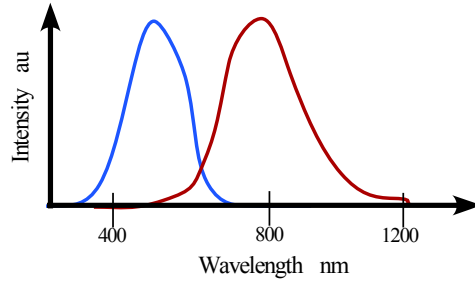
Figure 2.3. Generalized absorption and emission profile of a Ti:Sapphire laser crystal.

The respective transitions responsible for the broad absorption and emission profile of the Ti:Sapph crystal are d-d electronic and vibronic transitions (electronic transitions which emit or absorb phonons) of the Ti^{3+} ions. These transitions arise from the varying geometrical constraints of the Ti^{3+} ions in the Al_2O_3 crystal lattice that give rise to the vibrationally broadened ^2E_g and $^2T_{2g}$ states.[19-21] To put this into perspective, perhaps the best description of the broadened absorption and emission profile of the Ti:Sapph laser is through the use of a configuration coordinate diagram.[22] A simplified configuration coordinate diagram for Ti:Sapphire is shown in Figure 2.4.
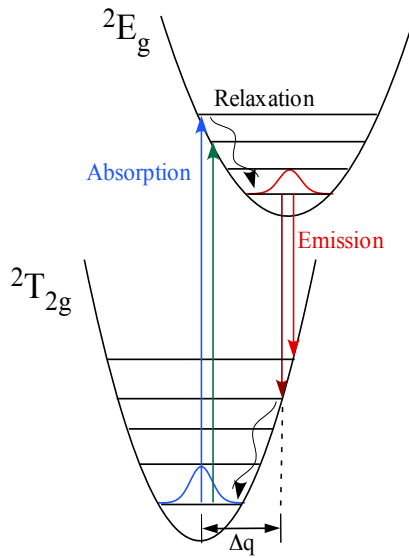
Figure 2.4. Configuration coordinate diagram showing absorption and emission in a Ti:Sapphire crystal.

In the above configuration coordinate diagram, the ground state ($^2T_{2g}$) and excited state (^2E_g) are shown with various vibrational energy levels that arise from coupling to lattice phonons of the Al_2O_3 crystal. Absorption occurs from the ground state to the excited state as shown in blue and green. If absorption occurs to a higher vibrational level within the excited state, relaxation to the lower vibrational levels within the excited state can occur through phonon emission. After relaxation, emission takes place from the lower vibrational levels back to the ground state. The parameter Δq denotes a coordinate displacement between the energy states that relates directly to the physical offset of the Ti^{3+} atoms with respect to the O^{2-} anions in the sapphire crystal.

2.2.3. Z-fold Ti:Sapphire Cavity

The oscillator cavity used in the transient absorption scheme of this dissertation is layed out in a z-fold cavity design. For the cavity to produce a continuous wave (CW) output, only one condition must be met: the CW gain has to be greater than any intracavity losses per cavity round trip. This condition is fairly easily met by assuring the correct dopant density of Ti^{3+} in the crystal and by utilizing a high pump intensity through an adequate length of laser rod. These considerations need only outweigh inherent losses within the Ti:Sapph crystal (proportional to rod length) and losses incurred from the optical coatings and reflective surfaces of the other optics within the laser cavity.

Because the cavity must produce pulses at a repetition rate of ~80 MHz, however, the cavity must be longer than that of a simple CW design. The z-fold cavity design allows for a maximization of space while meeting the requirements for operating as an oscillator with an appreciable pulse repetition rate. The cavity layout as seen in Figure 2.5 uses the output of a frequency-doubled Nd:YAG laser at 532 nm to pump the Ti:Sapphire crystal. An adjustable slit allows for wavelength selection over the broad tuning range of the Ti:Sapph laser while an acousto-optic modulator (AOM) is responsible for mode-locking and is discussed in the sections below. Note that the generalized components of a resonant laser cavity are also present in the z-fold cavity design (high reflector, output coupler, laser gain medium).
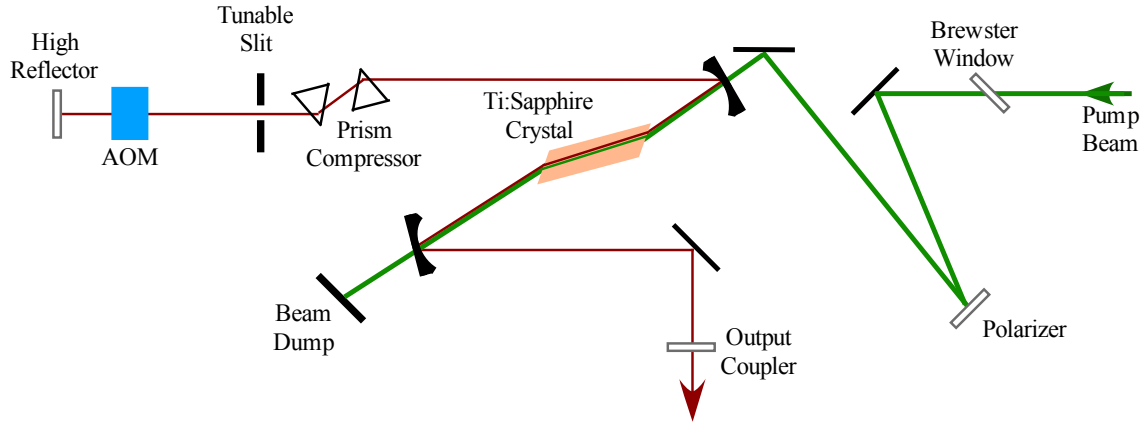
Figure 2.5. Schematic of the components of a simple mode-locked z-fold Ti:Sapphire laser cavity.

2.3. GENERATING LASER PULSES

In a typical laser cavity, the output is a continuously generated stream of photons, the previously mentioned CW output. While this is still an extremely valuable light source for some forms of spectroscopy, it is not useful for dynamical measurements. In trying to resolve dynamics, then, it is necessary to produce packets of light, or pulses, that have a shorter time component than the dynamics of the system being investigated. While there are a few ways to do generate pulsed laser sources, two methods that are used in the experiments of this dissertation will be briefly discussed: Q-switching and mode-locking.

2.3.1. Q-Switching

In Q-switching, the method of creating pulses relies on what is called a "quality" factor, or Q factor. Within the laser cavity, Q-switching effectively relies on switching the cavity in and out of its resonant condition, giving rise to the desired pulses of light. This technique delivers reliable pulses of light on the order of >10 nanoseconds in duration. In order to achieve pulses from the Q-switching technique, the use of electro-optic devices such as a Pockel's cell is necessary. A Pockel's cell is essentially a voltage-controlled waveplate, which utilizes the Pockels effect to act as a shutter when combined with an external polarizer. A Pockel's cell then operates on the principle that when an electric field is applied to the cell, the birefringence of the material changes thus rotating polarized light and acting as a wave plate (Figure 2.6). In combination with a polarizer, the electrical input is timed to create a nonresonant condition in the cavity. When the Pockel's cell is activated, the cavity becomes resonant and a pulse of correctly-polarized light is ejected from the cavity.
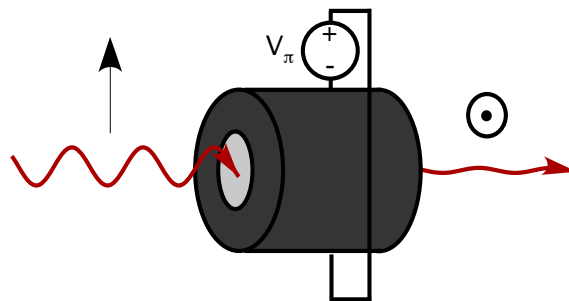
Figure 2.6. Simple description of a Pockel's cell acting as an optical rotation device. In the "off" position, no optical rotation is inflicted on the incoming polarized light (in the plane of the page). In the "on" position as shown above, rotation of the polarized light is induced and shown as a 90° rotation (perpendicular to the plane of the page).

38

A general scheme of Q-switching within a laser cavity would involve the placement of the polarizer and Pockel's cell between the cavity end mirrors. Figure 2.7 shows this scheme where the Pockel's cell acts as a ¼ waveplate within the cavity. In the on position, the laser cavity is in its resonant condition allowing for the ejection of a huge pulse. When the cell is switched into its off position, the cavity is meets its nonresonant condition with low cavity feedback. Relatively large pulses of up to 30 W at a repetition rate up up to 10 kHz can be achieved with this type of Q-switching layout.
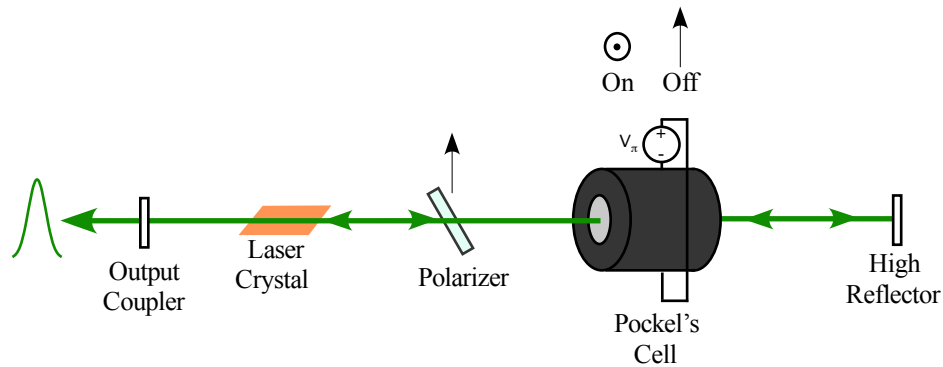
Figure 2.7. Schematic of the use of a Pockel's cell and polarizer to create resonant (on) and nonresonant (off) conditions within a laser cavity. When in the resonant condition, the cavity can eject a large pulse on the order of > 10 ns duration.

2.3.2. Mode-locking

While Q-switching represents a stable and useful way to create pulses of light, it is a limited technique that can generate roughly 10 nanosecond pulses (on the shortest timescale). Because the dynamics of many chemical and physical systems occur on a much faster timescale, other techniques to achieve shorter pulses are necessary. The theory of mode-locking was first proposed in 1964 and was experimentally reported

within the same year.[23,24] Mode-locking is another technique which makes use of the "locking" of relative phases of cavity modes together to create pulses by way of introducing an interference within the cavity. This interference must act both constructively and destructively at some point in the cavity to generate a propagating pulse.   When this intracavity pulse reaches the output coupler of the laser cavity, an output pulse is ejected from the laser cavity.

Within the laser system described in this dissertation, an acoutso-optic modulator (AOM) is used to achieve mode-locked pulses. The principle behind the AOM mode-locking technique is most closely related to active mode-locking. During active mode-locking, an optical element creates a sinusoidal modulation of the cavity losses or a periodic phase change that matches the pulse repetition rate. Active mode-locking by an acousto-optic device is perhaps most easily envisioned in the time domain. Figure 2.X shows how a precisely timed pulse of light is allowed to pass where the cavity losses are at a minimum.
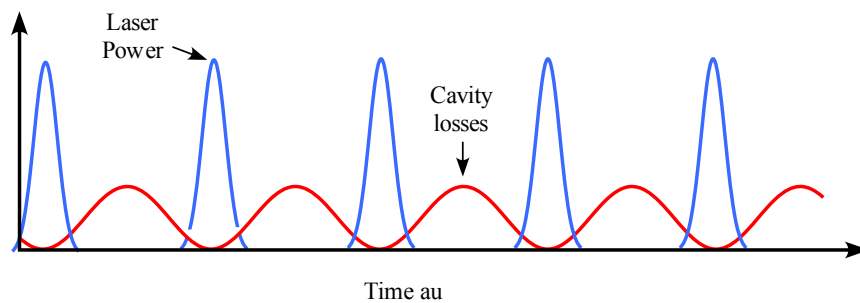
Figure 2.8. Sinusoidal modulation of laser cavity loses by an acousto-optic device and the corresponding optical pulses created via the active mode-locking technique.

In order to understand this efficiently, one must understand the AOM itself. An AOM operates on the acousto-optic effect where the refractive index of the material responds to a pressure wave (a sound wave). Similar to the above description of the operation of a Pockel's cell, an input signal drives a periodic change in birefringence of the AOM. The result of this acoustic change in the AOM is effectively a time dependent grating where the precisely timed diffraction of light through the AOM produces the necessary periodic cavity loss.

In the femtosecond laser system described here a regeneratively derived radio frequency (RF) signal drives the AOM creating stable pulses, a technique termed regenerative mode-locking. The RF signal used to drive the AOM is actually derived by the laser cavity itself. This is accomplished by monitoring the natural oscillations in the CW output of the Ti:Sapphire laser arising from the mode beating of partially phase locked modes within the cavity. This oscillation in output is captured on a photodiode, amplified, divided and fed back into the AOM to produce the oscillatory modulation of losses in the cavity necessary for mode-locking.

2.4. REGENERATIVE AMPLIFICATION

With respect to the laser system detailed in this chapter, the pulses ejected from the Ti:Sapphire oscillator cavity are of too little energy and at too high a repetition rate to be able to perform the desired pump-probe experiment. For example, in order to be able to generate the pump and probe pulses of the correct frequency, nonlinear optical techniques (which are inherently inefficient) are employed. In order to have enough

energy to perform these nonlinear processes and to reduce the pulse repetition rate to a useable range, a regenerative amplifier is used.

Regenerative amplification itself is a three-step process. Within a typical regenerative amplifier, there exists a stretcher, an amplifier cavity, and a compressor (Figure 2.9). In this configuration, a seed pulsetrain from the oscillator is directed into the amplifier. The seed pulses are stretched out in time and space to afford lower peak power to avoid damage to the amplifying Ti:Sapphire crystal. A stretched seed pulse is selected from the pulsetrain via injection into the amplifier cavity through a Pockel's cell and is allowed to propagate in a resonant amplifier cavity. Once amplified, the selected seed pulse is ejected at peak power into the compressor where it is compressed back to its original pulse width affording a high-energy, short-duration pulse.
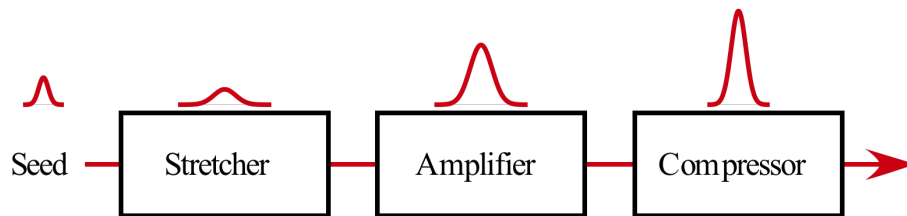
Figure 2.9. Schematic visualizing the three stages to regenerative amplification and the relative pulse properties at each stage.

In further detail, the stretcher and compressor units operate under the same principle. In both cases, a single pulse is stretched or compressed using chirp, or group velocity dispersion (GVD). To stretch a pulse, positive GVD is employed, and to compress a pulse, negative GVD is used.[25] For simplicity, only the stretcher will be discussed realizing that the compressor operates under the reverse process to the stretcher. In the optical layout of the stretcher, a 4-pass grating setup is used to introduce the positive GVD. A minimalistic schematic for this grating system is shown in Figure

2.10. GVD results when certain wavelengths within the pulse are required to travel over longer optical path lengths than other wavelengths. For positive GVD, the bluer components of the pulse take the longer path leading to a stretched time component of the pulse.
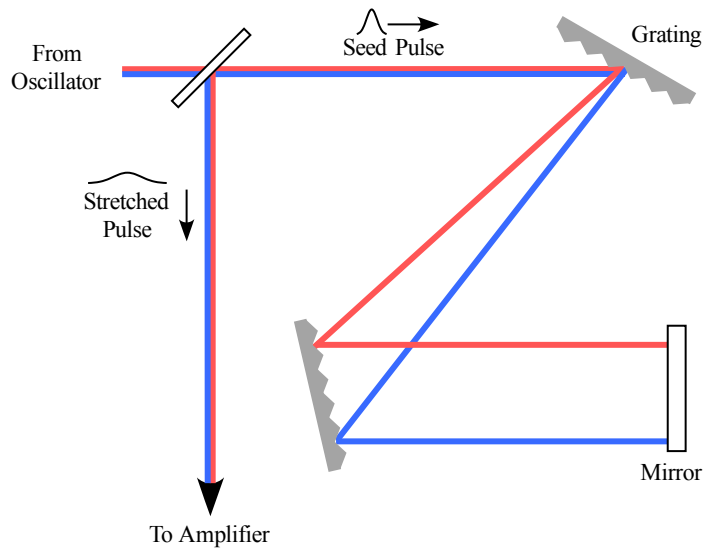
Figure 2.10. Minimalistic beam path of the regenerative amplifier stretcher. The figure shows positive GVD (chirp) whereby the blue wavelengths of the seed pulse must travel a slightly longer optical path length hence stretching the pulse in time along with the spectral dispersion of the pulse via passes over the optical gratings.

Once the seed pulses are stretched to reduce peak power, they are directed into the amplifier cavity. The amplifier cavity works to exploit synchronous spontaneous emission of the seed pulse overlapped with a large Q-switched pulse from a high-energy pump laser. This Q-switched pulse creates an appropriately timed population inversion within the Ti:Sapphire amplifier crystal which affords stimulated emission brought forth by the seed pulses. This results in amplified pulses with the same characteristics as the

seed pulses. A typical round trip of a picked pulse through the amplifier cavity is 10 ns. With each successive round trip, the pulse builds energy until gain saturation is reached. Because high-energy pulses are required for the pump-probe experiment, the pulses are ejected from the amplifier cavity at their peak power. While the pulses are now amplified, they are also still stretched in time and space. In order to restore the original temporal resolution of the pulses, they are passed through the compressor. This regenerative amplification process results in amplified pulses at nearly 3W with 100 fs duration and a pulse repetition rate of 1 KHz.

2.5. DESIRED FREQUENCY GENERATION

In order to probe exciton dynamics in the PbS nanoparticle samples as described in the latter chapters of this dissertation, pump and probe beams at specific frequencies are required. For a given nanoparticle sample, the pump pulses must be tuned to either 400 nm or 800 nm depending on the type of experiment run. Additionally, the probe pulses are tuned according to the interband absorbance (exciton absorbance) of each particular nanoparticle sample (Figure 2.11). There are separate but similar processes that govern the way the pump and probe are treated to obtain these frequencies.
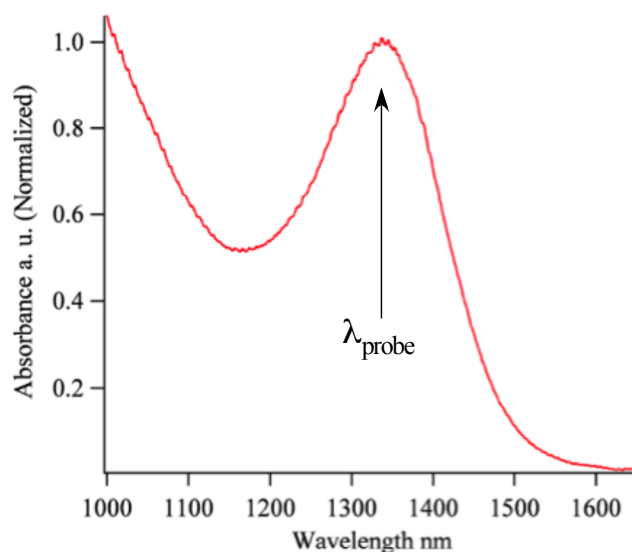
Figure 2.11. Examlple NIR absorbance spectrum for a population of NPs dispersed in solvent. The spectrum is normalized at the NP 1st exciton absorbance analogous to the semiconductor bandgap.

2.5.1. Pump Frequency Generation: 2nd Harmonic Generation

Pump pulses for the transient absorption experiments in which multiple exciton generation (MEG) is being investigated require the frequency doubling (or 2nd harmonic generation) of the 800 nm photons in the pump line. This ensures that the energy of the pump photons meets the energy requirements for MEG (ie. $h\nu \geq 2\ E_g$) in each particular nanoparticle sample investigated in this dissertation.

Frequency doubling or second harmonic generation (SHG) of the 800 nm photons is accomplished through nonlinear conversion in a non-centrosymmetric β-Barium borate crystal (BBO crystal). A physical representation of this process is thought of as taking two 800 nm photons and smashing them together to generate one 400 nm photon. In practice, this is achieved by utilizing a phasematching (or index matching) condition

within the BBO crystal. Since the BBO crystal is non-centrosymmetric, its index of

refraction varies with respect to the crystal's orientation on the optical axis. Practically

speaking, this is accomplished through orienting the crystal so that $n_\omega = n_{2\omega}$. This reduces

dispersion and allows for an appreciable amount of second harmonic radiation.

Mathematically, this is most efficiently described by recognizing the series

expansion of the electric polarization of an incident lightwave propagating through some

isotropic medium, Equations 1 and 2.[26]

$$P = \varepsilon_0 \chi E \qquad (1)$$

$$P = \varepsilon_0 (\chi_1 E + \chi_2 E^2 + \chi_3 E^3 + ...) \qquad (2)$$

In Equations 1 and 2, P denotes the electric polarization of the medium, ε_0 is the

electric permittivity in a vacuum, χ is the electric susceptibility and E is the electric field

of the propagating wave. Equation 1 shows that for low energy electric fields, the forces

placed on the valence electrons in the propagation medium (P) are proportional to the

incident electric field. It is conceivable, however, that for high energy fields, the electric

polarization may become saturated giving rise to the expanded polarization of Equation 2

(keeping in mind that P and E are travelling in the same direction). Applying the above

expansion on a generalized waveform (Equation 3) gives Equation 4, which can be

rearranged to Equation 5.[26]

$$E = E_0 \sin(\omega t) \qquad (3)$$

$$P = \varepsilon_0 \left(\chi_1 E_0 \sin(\omega t) + \chi_2 E_0^2 \sin^2(\omega t) + \chi_3 E_0^3 \sin^3(\omega t) + ... \right) \qquad (4)$$

$$P = \varepsilon_0 \chi_1 E_0 \sin(\omega t) + \frac{\varepsilon_0 \chi_2}{2} E_0^2 \left(1 - \cos(2\omega t)\right) + \frac{\varepsilon_0 \chi_3}{4} E_0^3 \left(3\sin(\omega t) - \sin(3\omega t)\right) + ... \qquad (5)$$

As shown in Equation 5, the cosine term of the electric polarization in Equation 5 oscillates at the frequency of 2ω or twice the fundamental frequency. Incidentally, any light reradiated from this medium has a frequency component of 2ω as well and is thus the second harmonic component of the input frequency. Of course while Equations 3 and 5 outline this process to a simple approximation, there is a good deal of complexity overlooked in the above description. In practical applications of SHG, the electric polarization in any one direction of an SHG crystal can affect the polarization in any other direction. Because of this, the susceptibility is not necessarily a simple scalar quantity, but rather a susceptibility tensor.

2.5.2. Probe Frequency Generation: Optical Parametric Amplification

Generation of the tunable NIR probe pulses is accomplished through an optical parametric amplifier (OPA), a Spectra-Physics OPA 800C. OPAs have been used to generate frequencies in the NIR, IR and with other extensions can be used to generate frequencies in the UV and visible spectrum.[27] The basic principal of operation in the OPA 800C is the mixing of photons in a similar nonlinear BBO crystal as the SHG process. To understand this to a first approximation, we again turn to the series expansion of the electric polarization (Equation 2 above). If we now consider a wave of the form described in Equation 6, we can collect the second order terms as Equation 7.[26]

47

$$E = E_{01}\sin(\omega_1 t) + E_{02}\sin(\omega_2 t) \tag{6}$$

$$P_{(2)} = \varepsilon_0 \chi_2 \left(E_{01}^2 \sin^2(\omega_1 t) + E_{02}^2 \sin^2(\omega_2 t) + 2E_{01}E_{02}\sin(\omega_1 t)\sin(\omega_2 t) \right) \tag{7}$$

The first two terms are represented as functions of $2\omega_1$ and $2\omega_2$ while the final

term yields an expression containing $\omega_1 + \omega_2$ and $\omega_1 - \omega_2$, the respective sum and

difference frequency mixing terms. This is shown explicitly by the rearrangement of the

final term in Equation 7 yielding Equation 8.

$$2E_{01}E_{02}\sin(\omega_1 t)\sin(\omega_2 t) = E_{01}E_{02}\left(\cos((\omega_1 - \omega_2)t) - \cos((\omega_1 + \omega_2)t)\right) \tag{8}$$

The optical parametric amplification process in the OPA is a two-photon mixing

process related to the above description, in particular to the difference frequency mixing

(so-called down conversion) term of Equation 8. For down conversion in the OPA, there

is a high-energy pump beam with frequency υ_1 as shown in Figure 2.12. This pump light

propagates collinearly through the BBO crystal with a small amount of signal to be

amplified (with frequency υ_2). The pump beam is converted into a difference frequency

wave called an idler wave with frequency $\upsilon_3 = \upsilon_1 - \upsilon_2$. If that idler beam is allowed to

propagate again through the crystal with the residual pump beam, the result is further

conversion of the pump frequency into signal and idler frequencies, known as optical

parametric amplification.
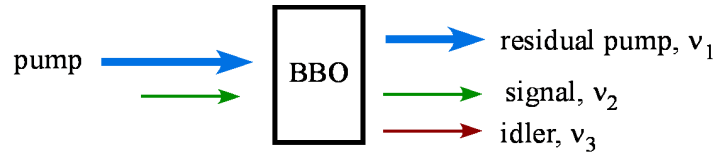
Figure 2.12. Schematic of the down conversion in a nonlinear BBO crystal. The seed beam of frequency ν_2 is overlapped through the BBO crystal with a selected higher frequency component of the broadband pump beam (ν_1) resulting in idler photons of frequency ν_3.

The optical layout of the OPA 800C is shown in Figure 2.13 where pulses from the regenerative amplifier are split into a white light generation stage and pre-amplification stage and a power amplification stage. To generate the white light, which acts as the seed beam in this first stage, a small portion (~ 5%) of the 800 nm input beam is focused tightly at the front face of a sapphire plate creating supercontinuum pulses. This white light seed beam is then overlapped temporally and spatially with the pre-amp (~15% of the input beam) in a Type II BBO crystal generating pre-amplified signal and idler beams. In Type II phasematching, the signal and pump photons are of opposite polarizations.[28] In this specific OPA configuration, the generated idler photons also polarizations of signal and idler photons enables easy separation of the two pulses with a simple polarizer

After the preamplification stage, a dichroic filter (D3) selects the idler component, which is then directed back through the BBO crystal as the new seed beam. On the return trip, the idler is overlapped with the power amplification beam (~80% of the input energy) to generate the desired signal and idler photons. By turning the orientation of the BBO crystal, the signal and idler pulses can be tuned from 1.1-1.6 μm and 1.6 to 2.0 μm, respectively.
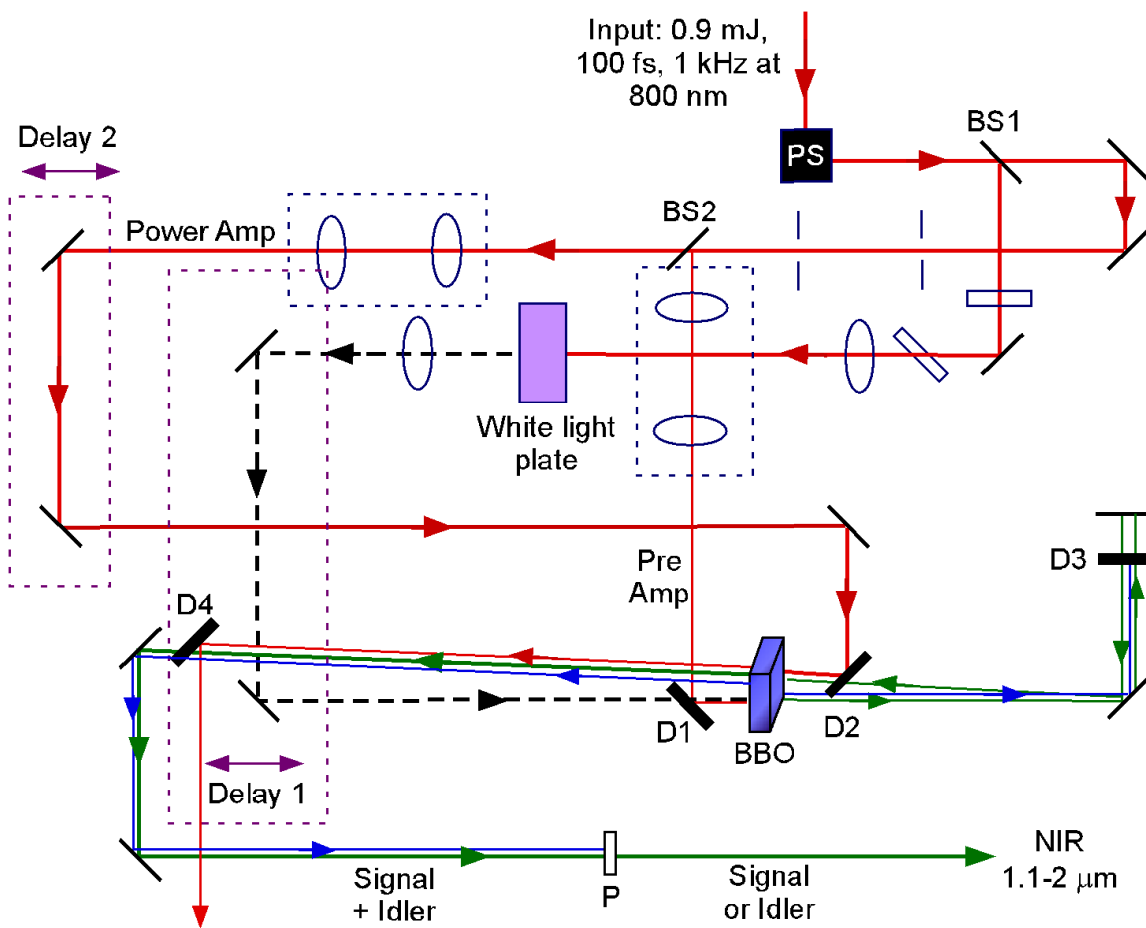
Figure 2.13. Optical layout of the OPA 800C used to generate tunable NIR pulses for matching the first exciton frequency of each nanoparticle sample.

Typical OPA output pulses through the NIR have a spectral width width in the range of 40-80 nm. The 1st exciton absorbance of the nanopartices of interest in these studies lie in the range of 1200—1600 nm which corresponds to the frequency range of the signal and idler output of the OPA in its original configuration. Figure 2.14 shows a representative sample of spectra obtained for the desired tuning range of the amplified signal or idler beams out of the OPA.
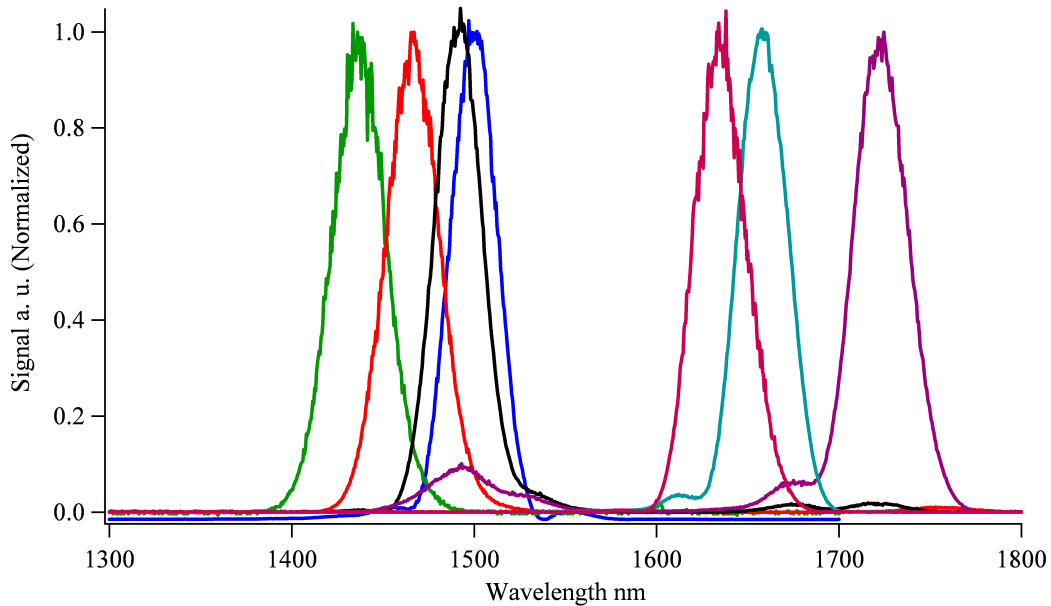
Figure 2.14. Examples of normalized OPA output spectra indicating the tunablility of the signal and idler pulses over the frequencies of interest in the NIR. Signal and idler pulses can be separated by polarization-specific optics due to the Type II phase matching of the BBO crystal.

2.6. TRANSIENT ABSORPTION OF PbS NANOPARTICLES

2.6.1. Optical Layout

The optical schematic of the femtosecond transient absorption experiment is shown in Figure 2.15. In this experiment, 750 mW, 100 fs seed pulses centered at 800 nm from a SpectraPhysics Tsunami oscillator (pumped with a 5 mW continuous wave Nd:YAG laser; SpectraPhysics Millenia) are amplified in a SpectraPhysics SpitfirePro regenerative amplifier (pumped by a q-switched, 30 W Nd:YLF laser; SpectraPhysics Empower). The amplified pulses have a repetition rate of 1 KHz and are split into pump and probe components.

51

The probe beam is directed into the SpectraPhysics OPA 800C where pulses are tuned to match the NIR 1st exciton absorbance of each nanoparticle sample as described previously. The probe is then collimated and steered down a optical delay line controlled by a micron-resolution stepper motor. Using a corner-cube retroreflector, the probe beam is directed back toward the sample interface. The probe is focused down and overlapped with the pump beam into the center of the sample cuvette.

The pump beam is collimated and directed along the optical layout with a few considerations. The pump path length must be equal to the probe path length where the delay stage is nearest to its home position where simultaneous excitation by the pump and probe pulses occurs (zero delay). The dynamical measurements are taken by moving the delay stage back thereby increasing the probe path length and subsequently increasing the time delay between pump and probe pulses at the sample interface. Additionally, the pump beam has two fundamental frequencies. In experiments where MEG is not being investigated, the wavelength of the pump remains at 800 nm as ejected from the regenerative amplifier; however, in the case where MEG is being studied, the wavelength of the pump is frequency-doubled to 400 nm which corresponds to $\geq 2E_g$ (where E_g is the band gap energy, or 1st exciton absorbance energy) of the nanoparticle sample.
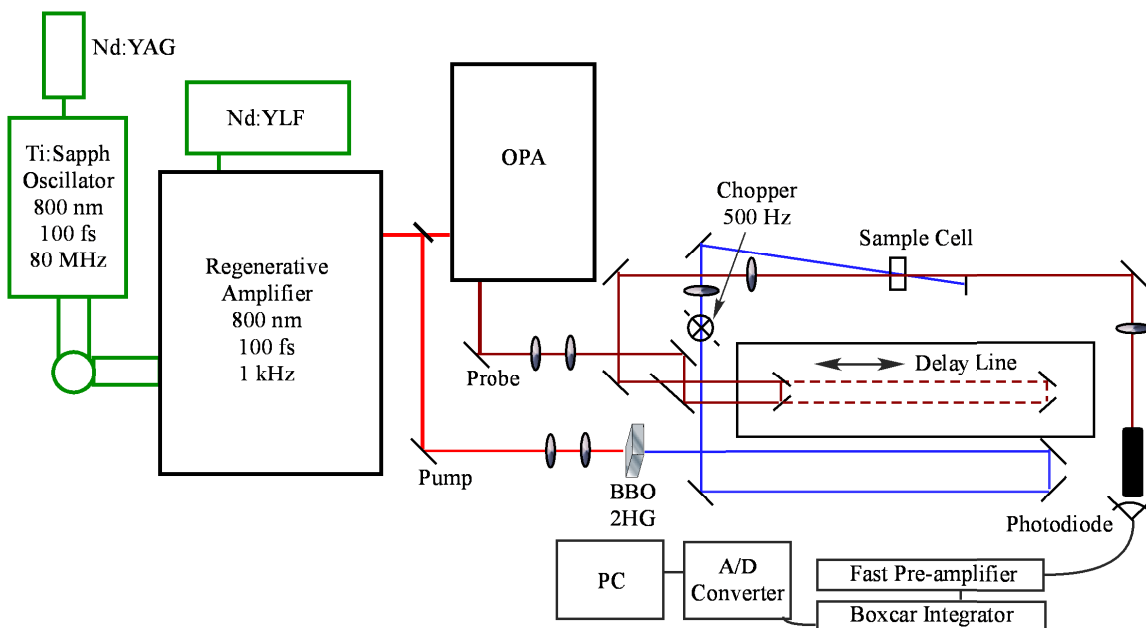
Figure 2.15. Optical layout of the femtosecond transient absorption pump-probe experiment. The pump beam is frequency-doubled for MEG experiments and left unaltered for non-MEG excitation. Probe pulses are tuned in the OPA. Pump and probe pulses are overlapped in the sample plane and the time delay is controlled by a micron-resolution delay stage. Signal with and without pump excitation is recorded to give change in transmittance.

2.6.2. Signal Detection and Characterization

A typical spot size for the probe beam was < 0.5 mm with an average energy of 0.5 µJ. The pump beam size was approximately 1 mm in diameter. It should be noted that for each sample, the energy of the probe beam was reduced until the signal at early times was linear with respect to the input energy so that no induced nonlinearities complicated the data analysis; however, the pump fluence was varied through the measurements both within a linear regime and a nonlinear regime. To obtain the transient absorption signal, the probe pulses were delayed with respect to the pump pulses via a linear translation stage controlled by a micron resolution stepper motor (Aerotech ATS-2060). The pump pulse repetition rate was decreased to 500 Hz (probe pulse

53

repetition rate was 1000 Hz) using an optical chopper to detect both pumped and unpumped contributions to the absorbance. The probe signal was collected on a fast InGaAs photodiode (Thorlabs DET410), and the pump signal was indexed on a fast Si photodiode (Thorlabs DET210). Both signals were sampled with a boxcar integrator (Stanford Research Systems SR250), converted to a digital signal through a National Instruments DAQ board, and analyzed on a PC. If necessary, the signals were amplified with a fast preamplifier (Stanford Research Systems SR445A).

The time resolution of the transient absorption experiment at the sample interface was determined by the cross-correlation of the pulses.[29] This was determined by overlapping the pump and probe pulses in a nonlinear lithium triborate (LBO) crystal at the sample interface. The sum frequency component of the overlap of the 800 nm pump and NIR probe pulses was detected on a fast silicon photodiode over a small change in probe pulse delay. Figure 2.16 shows the cross-correlation output data with the Gaussian fit profile. The full-width half maximum of this artifact is approximately 270 fs, which determines the time resolution of the experiment.
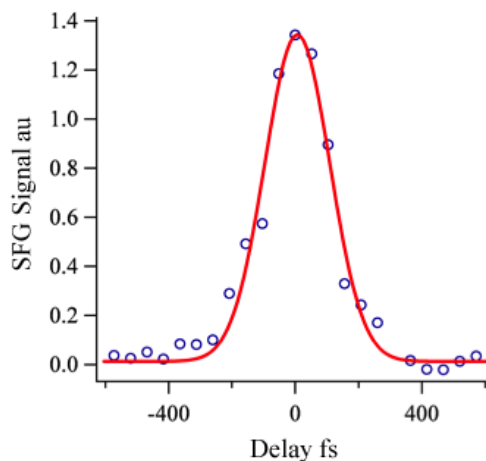
Figure 2.16. Cross-correlation artifact at the sample interface to determine the instrument temporal resolution. The artifact was generated as the sum frequency of the 800 nm pump and NIR probe pulses in a SFG crystal placed in the sample plane. Fitting this artifact yields a 270 fs full width half maximum.

2.6.3. Sample Handling and Considerations

All samples investigated in this dissertation were solutions of colloidal PbS nanoparticles (NPs) dispersed in appropriate solvents. All NP samples were degassed under nitrogen or prepared in a nitrogen atmosphere and sealed in 2 mm path length cuvettes unless otherwise specified. In order to reduce any effects due to photocharging of the NPs or other artifacts arising from multiple laser shots repeatedly sampling the same NP population, the samples were stirred vigorously throughout the transient absorption experiments.[30,31] Finally, multiple repeated scans of each shot-averaged decay profile were taken. This was done not only for data repeatability and averaging of the traces but also to ensure that no photodamage to the samples had occurred especially in the case of high fluence measurements.[32]

2.7. CONCLUSIONS

This chapter describes the basic concepts of and the specific layout of the laser apparatus used for experiments in this dissertation. An overview of general laser cavities including Ti:Sapphire lasing was presented as a building block for the transient absorption (TA) experiment, the time resolution of which is on the order of 270 fs. Additionally, basic principles that allow for the generation of amplified short laser pulses (ie. Q-switching, mode-locking, and regenerative amplification) were described. Also, the relevant nonlinear frequency generation techniques used to generate the desired pump and probe components of the TA experiment were discussed in detail. Lastly, the layout of the TA experiment was presented along with any important sample handling considerations.

The TA experiment and relevant optical components described in this chapter was used to collect data regarding charge carrier generation and recombination in the variously capped PbS nanoparticles of Chapters III and V. Specifically, this chapter serves as a primer in the state of the art equipment used in the next chapter (Chapter III). In Chapter III, the effect of ligand exchange from oleic acid to sodium 2, 3-dimercaptopropane sulfonate was investigated for multiple exciton generation and recombination.

CHAPTER III

THE EFFECT OF AN IONIC LIGAND ON MEG IN PbS NANOPARTICLES

3.1. INTRODUCTION

Pb-based nanoparticles (NPs) have been recently studied as materials for solar conversion due to their size-tunable NIR absorbance and strong absorption through the visible spectrum.[1-5] Several types of NPs including PbS, PbSe and PbTe NPs have been investigated for multiple exciton generation (MEG) as a way to bypass the Shockley-Queisser limit of photoconversion efficiency.[4,6-21] While MEG has been reportedly efficient in lead chalcogenide NPs,[6,8,18,20] in order to enhance the efficiency of a solar cell, the extraction of charge carriers from the NP into a device must be competitive with the relaxation of multiexcitons which relies heavily on the NP surface ligands.

As described in Chapter I, the surface of a NP has been hypothesized to play a large role in the electronic and optical properties of the crystal due to the high surface to volume ratio of the NP.[22,23] While there have been a few studies to investigate how the surface of the NP affects exciton dynamics[11,20,23], studies to directly probe the effect of the NP ligand shell on phenomena such as MEG are missing or fail to uncover effects on MEG due solely to the ligand shell. Understanding exactly how the ligand shell contributes to MEG will lead to quicker realization of devices capable of utilizing the promising properties of semiconductor NPs for enhanced solar conversion.

The research discussed in this chapter details ligand effects on multiple exciton generation (MEG). In this investigation, oleic acid (OLA) was substituted for 2, 3-dimercaptopropanesulfonate (DMPS) and the effect of these ligands on the generation and decay of multiple and single excitons was measured. In order to investigate this phenomenon, dynamical measurements were made using transient absorption spectroscopy. This technique probes the ultrafast decay components for single and multiple excitons. Additionally, analysis of the raw kinetic data yields information on relative populations of excitons over time, MEG quantum yields (QYs), and fractions of trapped charge carriers. The material in this chapter was co-authored with Dr. David R. Tyler who acted as my advisor during this investigation and Dr. Thomas Novet who provided the starting PbS-OLA NPs for this study.

3.2. CHOICE OF LIGANDS

Because we are trying to elucidate the direct effect of the ligand on MEG, we determined that solution phase samples were of interest primarily due to the fact that, in solution, the effective concentration of NPs is less than in a film, which decreases the likelihood that interparticle distance is affecting MEG. During our initial investigations of nanoparticle ligand-shell substitution reactions, we found that substitution of PbS-OLA nanoparticles by neutral organic thiol ligands led to precipitation of the nanoparticles or to opaque solutions in a wide variety of solvents, rendering the NPs unsuitable for our transient absorption measurements. It was necessary therefore to find a ligand, other than one of the neutral thiols, which would allow the NPs to remain

suspended in a transparent solution. A literature search revealed that substitution of oleic

acid-capped nanoparticles by 2,3-dimercaptopropane sulfonate (DMPS) yielded stable

nanoparticles in solution, particularly under anaerobic conditions[24]. This same study

suggested that, once the DMPS is coordinated to the NP, the ionic ligands repel one

another, thereby maintaining a minimum interparticle distance that reduced the

probability of precipitation brought on by agglomeration. Most importantly, this study

determined that thin film devices made with the PbS-DMPS NPs showed enhanced

photoresponse in the NIR compared to PbS-OLA films, where no photocurrent was

detected under the same conditions. This enhanced photoactivity was primarily attributed

to the reduced interparticle spacing in the PbS-DMPS films over PbS-OLA films.

Transient absorption studies of the PbS-OLA and PbS-DMPS nanoparticles could reveal

additional information regarding the differences in photoresponse of the films, such as

enhancements of MEG quantum yields or longer exciton lifetimes. The synthetic ease of

the DMPS-for-OLA substitution reaction, combined with the encouraging thin film

photocurrent results, was a strong incentive to carry out this study using the DMPS and

OLA NP systems.

3.3. EXPERIMENTAL METHODS

All reagents and solvents were obtained from Sigma-Aldrich except D_2O, which

was purchased from Cambridge Isotope Laboratories. Lead sulfide NPs were synthesized

by preparing a lead precursor solution according to the method of Hines and Scholes.[1] To

synthesize the parent oleic acid-capped particles, a solution consisting of 4 ml octadecene

and 4 ml oleic acid was prepared and 0.3 g PbO was added to the mixture. The solution was heated under vacuum to 100 °C for 30 minutes to dissolve the PbO and to drive off H_2O. The solution was subsequently heated to the appropriate injection temperature (100 ºC to 150 ºC) for the desired particle size and held at that temperature for at least 30 minutes.

While the lead solution was heating, a sulfur precursor solution of 0.167 ml hexamethyldisilathiane and 4 ml octadecene was degassed under nitrogen. When the lead solution reached the desired injection temperature, the sulfur precursor was quickly injected into the flask and allowed to cool to room temperature. Removal of excess ligand and octadecene was completed by repeated precipitation in acetone, centrifugation of the particles, and dispersion in small amounts of toluene.[1] Near-infrared (NIR) characterization of the particles was accomplished using a Perkin-Elmer Lambda 19 UV/vis/NIR spectrophotometer. Particle size and monodispersity were measured using a FEI Titan 80-300 TEM in STEM mode (PbS-OLA NP d = 5.0 ± 0.7 nm).

Ligand exchange on the PbS-OLA particles was accomplished according to literature precedent.[24] D_2O was chosen as the solvent over H_2O due to its suppressed NIR absorption. Equal volumes of PbS-OLA solutions (25 mg/ml) and the 2,3-dimercaptopropanesulfonate sodium salt dissolved in D_2O (78 mM) were stirred until phase transfer of the particles was complete (approximately 1 hour). The ionically functionalized NPs were centrifuged to break emulsions formed during stirring and phase transfer. The PbS-DMPS particles were then precipitated from D_2O using acetonitrile, centrifuged, and resuspended in D_2O. The particles were characterized by NIR absorbance spectroscopy and TEM imaging (PbS-DMPS NP d = 5.2 ± 0.9 nm).

3.3.1. Pump-Probe Experiment

The optical setup used for obtaining the pump-probe transient absorption data was described in Chapter II. In this study, the photon fluence of the pump beam at 800 nm excitation was varied so that the average number of photons absorbed per nanoparticle at the front face of the cuvette, N_{abs}, was less than 3 to ensure the measurement and decay of only biexcitons and single excitons. The traces obtained at 400 nm excitation were collected at fluences that corresponded to a N_{abs} range of 0.06-1. This was accomplished by introducing neutral density filters into the beam path. Additionally, the spot size diameters for the pump and probe beams were 1.0 mm and 0.5 mm respectively.

3.3.2. Sample Preparation and Handling

Solvents were degassed with nitrogen prior to use. Samples were prepared by dispersing NPs in an appropriate solvent at a desired concentration. Sample solutions were placed in 10 mm path length cuvettes equipped with stir bars and PTFE stoppers. To ensure removal of oxygen, PbS-DMPS solutions were degassed a second time before transferring to cuvette in the latter studies. The headspaces of all cuvettes were filled with nitrogen, and the cuvettes were taped and sealed for the duration of the femtosecond experiments.

As a special note, transients taken for stirred and static solutions of both PbS-OLA and PbS-DMPS sometimes showed an appreciable difference in the ratio of early to late population components. Also, as previously mentioned, there have been recent

reports outlining the observation of ligand-dependent photocharging of NP solutions.[25] For these reasons, all of the samples used for MEG determination in this study were stirred to uncover the true MEG yields and dynamics for each sample.

3.4. RESULTS AND DISCUSSION

Raw transient absorption traces at varied pump fluences obtained for 800 nm excitation (Figure 3.1a) were fit using a global, least-squares fitting routine. The subsequent analysis was performed according to the procedure outlined by Ellingson, *et al*.[18] Within this analysis, the time constants for single exciton (τ_X) and biexciton (τ_{MX}) recombination were global parameters and were varied for at least four kinetic traces until the best fit results were obtained. The resulting time constants revealed a single exciton lifetime of 80 ns and a faster biexciton time constant of 436 ps. The amplitudes for these variable fluence traces at 800 nm excitation ($< 2E_g$) are the Poisson amplitudes, which are influenced by N_{abs}. Upon extracting the amplitudes and exciton lifetimes in the case where MEG does not occur ($h\nu < 2E_g$), raw transients for MEG excitation can be analyzed. Figure 3.1b shows the variable fluence traces for the excitation of PbS-OLA at 400 nm ($3.35E_g$). In this case, the curves were fit by constraining τ_X and τ_{MX} to the extracted values obtained above; however, the amplitudes of these curves are no longer strictly Poissonian and now contain components of MEG. Extraction of the MEG quantum yield will be detailed later.
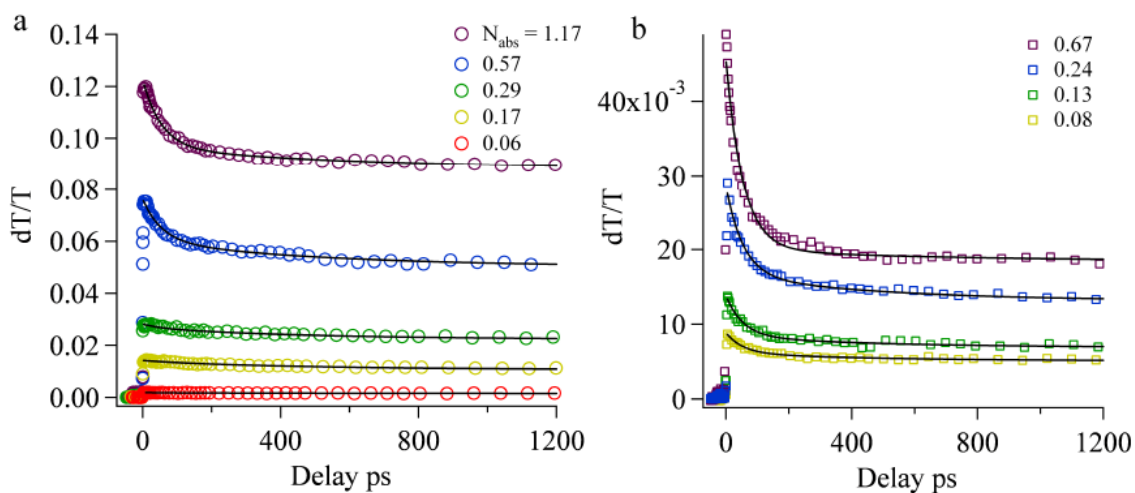
Figure 3.1. Transient decay curves for PbS-OLA NPs excited at (a) 800 nm (1.55 eV, 1.68E_g); (b) 400 nm (3.11 eV, 3.35E_g), with various pump intensities.

3.4.1 Ligand Exchange and Transient Absorption of PbS-DMPS Nanoparticles

Ligand exchange reactions were carried out on PbS-OLA nanoparticles with 2,3-dimercaptopropane sulfonate (PbS-DMPS). The PbS-DMPS NPs were characterized by TEM imaging and NIR absorption spectroscopy to confirm their size and exciton absorbance (see Experimental section). The red shift in the NIR spectrum for the PbS-DMPS NPs compared to PbS-OLA NPs (Figure 3.2) is accounted for by the change in dielectric constant of the solvent[24] and not by a change in particle size, as confirmed by TEM imaging.

63
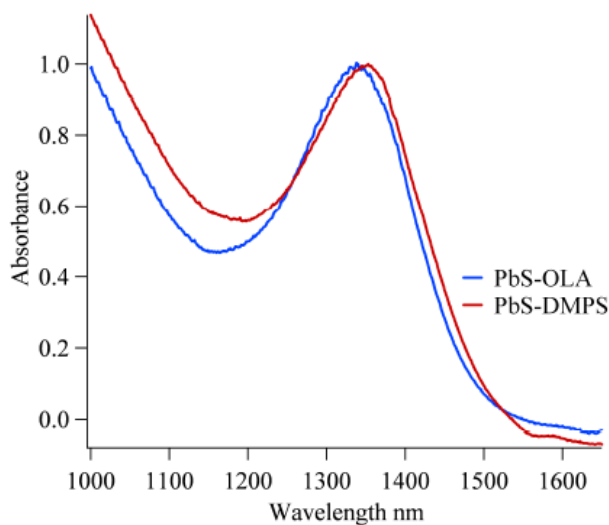
Figure 3.2. Near-IR absorbance spectra showing the 1st exciton absorption (1S$_h$-1S$_e$) for parent PbS-OLA nanoparticles (blue line) compared to ligand exchanged PbS-DMPS particles (red line).

Ultrafast decay curves for a single batch of PbS-DMPS particles were obtained for 800 nm and 400 nm excitation (1.69 and 3.38 times the bandgap energy, respectively) at various pump fluences. The raw traces for both excitation wavelengths are shown in Figure 4. It is interesting to note that the transient dynamics recorded for PbS-DMPS at 400 nm excitation (Figure 3.3b) are very different from the oleic acid capped particles under MEG conditions.
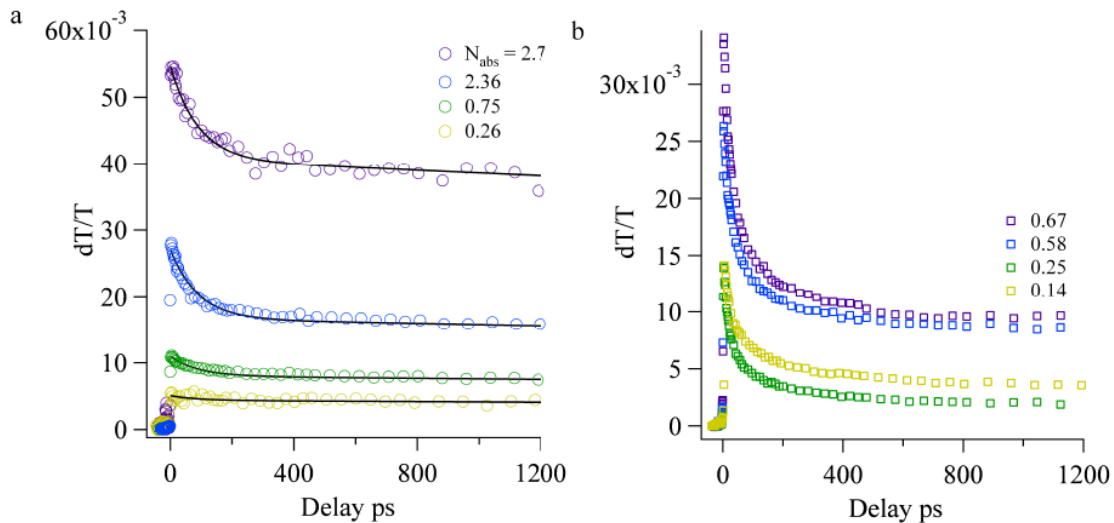
Figure. 3.3. Variable fluence transient curves and curve fits for PbS-DMPS under (a) 800nm and (b) 400 nm excitation.

At first glance, it appears that the PbS-DMPS nanoparticles excited under MEG conditions have a greatly enhanced MEG signature compared to the PbS-OLA NPs (the ratio of populations at early and late times; 2.5 and 3.4, respectively). However, experiments showed that the enhanced MEG in the PbS-DMPS NPs is likely attributable to NP decomposition leading to enhanced trapping. After 1 to 3 days in the sealed cuvettes, the particles precipitated out of solution. The precipitation time was loosely correlated to the care taken to remove oxygen in the samples. In order to investigate this phenomenon further, a second ligand exchange was performed from the same PbS-OLA parent batch but with care taken to remove O_2 from the PbS-DMPS product before sealing it in the sample cuvettes. Additionally, the PbS-DMPS and PbS-OLA NPs were monitored by NIR absorbance spectroscopy throughout the MEG laser experiments to ensure that the laser experiments were not carried out on decomposed NPs.
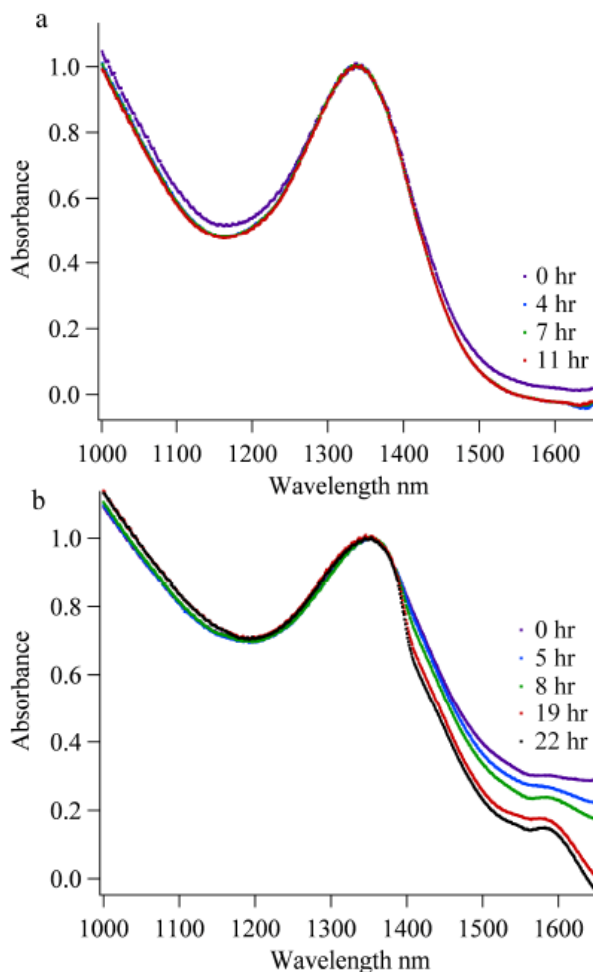
Figure. 3.4. Time-lapse absorbance spectra of (a) PbS-OLA nanoparticles and (b) ligand exchanged PbS-DMPS particles throughout the transient absorption experiments.

In the case of PbS-OLA NPs, shown in Figure 3.4a, there is no change in the $1S_h$-$1S_e$ (1st exciton) absorbance over the course of the femtosecond experiments. (It should be noted that there is a blue shift of the exciton absorbance in these NPs compared to freshly prepared NPs. This change is most likely due to some oxidation of the NP core[26] causing a change in size of the nanoparticles. Nevertheless, there is no evidence of the particles changing during the course of the MEG data collection.) In contrast to the PbS-OLA solution, the PbS-DMPS NPs do change during the MEG experiment (Figure 3.4b):

the first exciton absorbance peak narrows and appears almost multi-modal within one day.

To eliminate the effects of NP decomposition during the MEG experiments, only transient spectra taken within the first 8 hours following sample preparation were used in the data analyses. Additionally, the samples were degassed a second time prior to sealing the cuvettes. Results of the MEG experiments on PbS-DMPS NPs prepared under these anaerobic conditions are shown in Figure 3.5. Note there is no apparent decomposition in the spectra of the PbS-DMPS NPs.
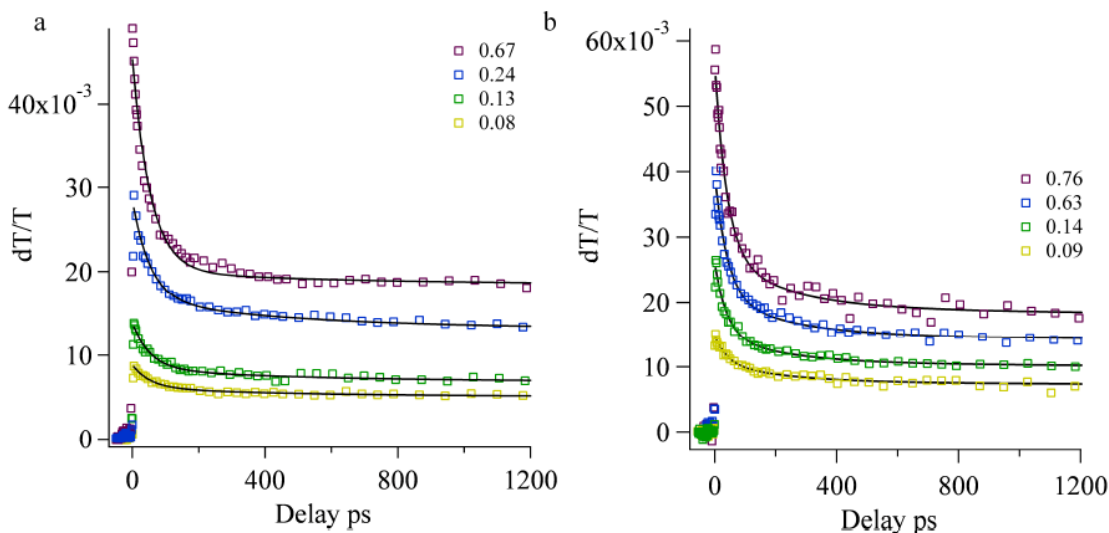
Figure 3.5. Decay curves for PbS-OLA and batch 2 of the PbS-DMPS particles excited under MEG conditions.

The global fitting procedure described previously was used to fit the raw transient data for PbS-DMPS. Time constants extracted from the non-MEG curve fits are listed in Table 1 and compared to those obtained for PbS-OLA. Also shown in Table 3.1 are the MEG quantum yields (QYs) for the PbS-DMPS and PbS-OLA particles. In determining QY, the ratio of short and long time signal (A/B) is plotted as a function of N_{abs} (Figure

67

3.6). Fits for the curves for 800 nm excitation assume Poisson statistics for the

absorption of photons by the NPs. The curves for 400 nm excitation are non-Poissonian

but are fit by allowing for the adjustment of the quantum yield (QY) which accounts for

the enhanced amplitudes due to MEG. By extrapolating these fits back to vanishing

photon fluence and dividing out the contribution of the 800 nm excitation curves, the

MEG QY for each particle set was determined.

Sample	τ_{MX} /ps	τ_X /ns	MEG Yield
PbS-OLA	436 ± 45	80	1.4 ± 0.1
PbS-DMPS	223 ± 65	36	1.5 ± 0.1

Table 3.1. Characteristic lifetimes of bi- (τ_{MX}) and single (τ_X) exciton decays and MEG efficiencies for PbS-OLA and PbS-DMPS.
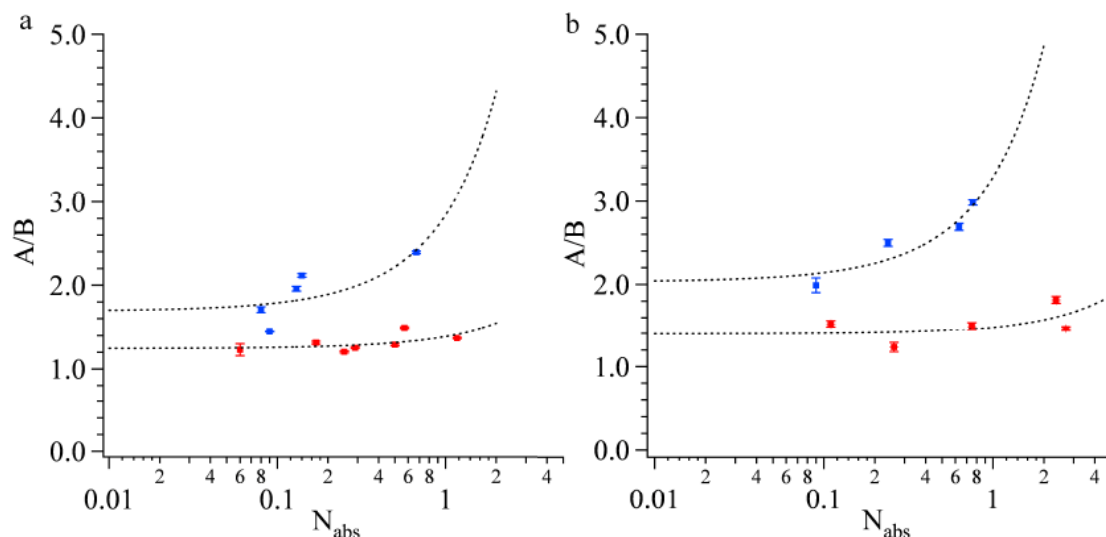
Figure 3.6. Ratios of early to late time signals versus the average number of photons absorbed per nanoparticle at the front face of the sample cuvette (N_{abs}) for PbS-OLA (a) and PbS-DMPS (b) particles.

Note in Table 3.1 that even the more rigorously deoxygenated PbS-DMPS NPs experience faster decay dynamics than their PbS-OLA parent batch; however, the MEG QY for each particle set is the same within experimental error. The time constants for multi- and single-exciton decay for the PbS-DMPS particles are less than half that of the PbS-OLA particles, indicating that the ligand has an effect on MEG and exciton recombination.

The origin of the ligand effect on the decay dynamics is unknown. One suggestion is that the faster decay rates for exciton recombination in the DMPS system are due to the negative charge on the ligand. It is suggested that the electron is electrostatically repelled by the anionic ligand shell. This would prevent delocalization of the electrons over the surface of the NP, spatially confining them to the core, which causes them to recombine with holes more quickly. A related hypothesis is that the

ligand effect can be attributed to the different ligating atoms in the two ligands. The

DMPS ligand binds through sulfur instead of oxygen. Because oxygen is more

electronegative than sulfur, it is more likely to accept electron density and therefore more

likely to delocalize the electronic wave function over the surface of the NP, which would

lead to slower electron-hole recombination rates. A final suggestion is that the

differences in the decay dynamics may be due to a solvent effect. Previous studies

suggested that the solvent can affect electron dynamics in NPs that have significant trap

state densities[26] but does not play as significant a role in passivated NPs.[27] The NPs used

in this investigation are passivated by the ligands, leading to the conclusion that solvent

effects may not be of great consequence. Investigations are underway in our laboratory

to probe further these ligand effects and to provide insight into their origin.

In one final note, while the PbS-OLA particles did not exhibit signs of

photooxidation during the laser studies, it is possible they might have undergone

oxidation prior to the laser studies and prior to ligand exchange. It is also possible that

having pre-oxidized particles during the ligand exchange facilitates the oxidation of the

ligand or prevents satisfactory passivation of the NPs, leading to the precipitation of the

NPs. During the course of our investigation, it was reported by Klimov *et al.* that

oxidation of the NP core has a slight effect on MEG dynamics.[7] In the same manner, if

oligosulfide formation of the DMPS ligand occurs due to oxidation then a coordination

site (or dangling bond) can open up on the surface of the particle. Both the oxidation of

the nanoparticle core and the presence of dangling bonds can contribute to electron-

trapping states on the NP surface. Correcting for a trapping factor in such a case provides

a better assessment of true MEG yields.

3.5. CONCLUSIONS

PbS NPs with oleic acid and 2,3-dimercaptopropane sulfonate ligands were investigated to determine how the NP ligand shell affects MEG and exciton recombination dynamics. Experiments showed striking differences between the PbS-DMPS samples prepared in the presence of oxygen and those prepared anaerobically. With oxygen present in the samples, the kinetic decay curves exhibited large false MEG-type signatures and enhanced recombination rates, due to the photooxidation and degradation of the NPs and the ensuing increase in the number of non-radiative decay pathways. Rigorous removal of oxygen from the samples produced kinetic decay curves with time constants for PbS-DMPS NPs that were significantly shorter than those of the PbS-OLA NPs. The origin of the differences in the exciton recombination decay rates is unknown, but it is speculated that it may be due to the ionic functionality of the DMPS ligand or to the different ligating atoms of the OLA and DMPS ligands.

This initial investigation into the effect of the ligand shell on MEG gives further credence to the idea that the ligand shell is an important parameter to control if NPs are to be used as solar converters. For this reason, experiments to decouple effects due to the donor atom or to the secondary ligand shell must be completed. Chapter IV shows the ligand exchange route taken to afford particles of different surface capping. In particular, Chapter IV details the experimental conditions necessary to provide PbS NPs capped with various ligands containing thiol and amine headgroups used in Chapter V for the investigation of the ligand donor atom on MEG.

CHAPTER IV

LIGAND EXCHANGE REACTIONS ON PbS NANOPARTICLES USING AN INTERMEDIATE LIGAND

4.1. INTRODUCTION

The surface chemistry of a nanoparticle (NP) is undoubtedly important when considering NPs for device applications. For example, the interfaces between the NP and components of the device must be optimized to prevent interfacial losses. Additionally, the NP ligand shell must provide stability to the NP to prevent NP decomposition within a device. In a solar cell, careful selection of the ligand shell could potentially maximize carrier generation, carrier lifetime and can possibly facilitate the extraction of charge carriers from the NPs into the cell.

PbS NPs are excellent candidates for solar applications due to their tunable absorbance over the NIR and high absorbance through the visible region of the solar spectrum[1]; however, fundamental research into the design of ligands for specific applications is currently limited by the existence of few synthetic routes to ligand-exchanged PbS NPs. In this chapter, we discuss a novel route to ligand-exchanged PbS nanoparticles through a sodium 3-mercaptopropane sulfonate (MPS) ligand intermediate. Through this intermediate ligand, an adaptable synthetic scheme was created to bind various amines and thiols to PbS nanoparticles affording easily tunable ligand structures

that are solution processable. This chapter contains material that is co-authored by Dr. David R. Tyler who acted as my advisor during this investigation.

4.2. MOTIVATION

It is fairly well known that long-chain ligands such as oleic acid and oleylamine can stabilize NPs of various types and sizes.[2-7] In fact, ligand exchange reactions and the synthesis of NPs in the presence of varying ligands have yielded differently capped NPs for various uses. In terms of semiconductor NPs as solar materials, it is beneficial to either have a ligand system that is short in order to reduce the inter-particle distance between NPs or to use a ligand that can actually facilitate charge transfer from the NPs into the device matrix.

In lead chalcogenide NP systems, there have been a limited number of ligand exchanges to afford new NPs for investigation in devices or for fundamental studies on how the ligand affects processes within the NP. In particular, few solution-phase exchanges have been precedented in the literature[8-10] considering that NPs for device fabrication and other fundamental measurements such as photoluminescence studies should ideally be readily solublized in appropriate solvents. In other ligand exchange reactions, however, products must be trapped onto a substrate[11] or are solid-state reactions on NP films[12] which are less desirable for batch scale-up if NPs are to be used on an industrial scale.

When we began investigating ligand exchange reactions on PbS NPs, it was quickly realized that there are few instances of ligand exchange on these types of NPs in

the literature and that a versatile exchange route to a number of different types of ligands was not necessarily available. It was also realized that in order to afford ligand exchange, reaction conditions that promoted only a forward reaction and reactions involving NP starting materials with poorly passivating ligand shells (amines, phosphines and phosphine oxides) seemed to yield successful exchange results.[6,13-15] With this in mind, we began a study to discover a more general and versatile route to obtain solution processable PbS NPs functionalized with an assortment of ligands containing thiol and amine headgroups.

4.3. EXPERIMENTAL METHODS

Unless stated otherwise, all manipulations were carried out in either a N_2-filled Vacuum Atmospheres Co. glove box or on a Schlenk line using N_2. Organic solvents used for the ligand exchanges were either subjected to multiple freeze pump thaw cycles to remove oxygen prior to use, or were dried and deoxygenated by passing them through commercial columns of CuO, followed by alumina under argon atmosphere. H_2O was degassed by purging with N_2. Commercially available reagents were used as received.

The PbS-OLA nanoparticles used for ligand exchange were synthesized according to literature precedent.[2] Purification of the nanoparticles was accomplished through a series of cleaning steps including precipitation, centrifugation and resuspension in suitable solvents. Nuclear magnetic resonance spectra were recorded on a Varian Unity/Inova 300 MHz (^{1}H, 299.94 MHz). The ^{1}H chemical shifts were referenced to TMS (0.00 ppm). Infrared spectra were recorded on a Nicolet magna 560 FT-IR with

74

OMNIC software. Samples were prepared as thin films on NaCl plates. NIR spectra were recorded on a Perkin-Elmer Lambda 19 UV/Vis/NIR spectrometer or a Hewlett-Packard 8453 UV/Vis spectrometer. TEM images were taken on a FEI Titan 80-300 TEM in STEM mode. Particle size analysis was accomplished with ImageJ software.

4.3.1. Biphasic Ligand Exchange

For the ligand exchange reactions in this chapter, the particles were reacted under biphasic conditions to afford the various amine and thiol-exchanged particles. The first biphasic reaction was run according to literature precedent to yield the PbS-MPS intermediate particles from oleic acid-capped particles (PbS-OLA).[8] In this case, PbS-OLA NPs are suspended in toluene at concentrations between 5 and 15 mg/ml while excess MPS ligand is dissolved in an equal volume of H_2O (200 mM). The solutions are combined, stirred and degassed under a stream of N_2 for 30 minutes. The reaction proceeds to completion when the PbS NPs migrate into the aqueous phase due to the binding of the ionic MPS ligand to the particles. Once the intermediate PbS-MPS particles are obtained, they are cleaned once by precipitation in acetonitrile followed by centrifugation above 3500 rpm for 10 minutes. The resulting pellet is dried over a stream of N_2.

The desired thiol or amine-capped PbS NPs were obtained by dissolving excess organic ligand (400-600 mM) in an appropriate solvent, typically toluene, and reacted in the same manner described above with an equal volume of an aqueous PbS-MPS NP solution (5 to 15 mg/ml). Once again, the reaction is complete when the PbS particles

bind to the desired ligand and migrate into the organic phase. Once the particles are in the correct phase, micelles are broken by centrifugation above 3500 rpm. The product NPs are then extracted with toluene and are purified by precipitation in acetone or ethanol, centrifugation and suspension in toluene (or chloroform).

Hexanethiol-capped PbS nanoparticles - ^{1}H NMR (300 MHz, CDCl$_3$): δ = 3.6, 1.9, 1.3, 0.9, ppm; IR (thin film on NaCl): ν = 2956-1850, 1457, 1377, 721 cm^{-1}; UV-Vis (toluene, as synthesized): λ_{max} = 932 nm.

Propanethiol-capped PbS nanoparticles - ^{1}H NMR (300 MHz, CDCl$_3$): δ = 0.8 ppm; UV-Vis (toluene, as synthesized): λ_{max} = 928 nm.

Methylbenzenethiol–capped PbS nanoparticles - ^{1}H NMR (300 MHz, CDCl$_3$): δ = 2.29 ppm; UV-Vis (toluene, as synthesized): λ_{max} = 895 nm.

Dodecylamine-capped PbS nanoparticles - ^{1}H NMR (300 MHz, CDCl$_3$): δ =2.8, 1.6, 1.3, 0.9 ppm; UV-Vis (toluene, as synthesized): λ_{max} = 927 nm; UV-Vis (dried, in toluene): λ_{max} = 894 nm.

Tetradecylamine-capped PbS nanoparticles - UV-Vis (toluene, as synthesized): λ_{max} = 915 nm.

4.4. RESULTS AND DISCUSSION

4.4.1. Ligand Exchange With Thiols

The native synthesis of the PbS NPs used in this study yielded oleic acid-capped NPs (PbS-OLA NPs), which are highly soluble in an assortment of organic solvents such as hexanes, chloroform and toluene. While PbS-OLA particles are extremely stable,

likely due to the bidentate binding of the carboxylate group to the Pb atoms on the NP surface, ligand exchange from OLA has proven to be difficult. In cases of exchanges with thiols where reaction conditions should lead to the desired products (thiophilicity of Pb and excess ligand concentration), bound OLA is still observed in the ^{1}H NMR spectrum after days of stirring.   Additionally, insoluble and unidentifiable black precipitates form in these reactions, leading to the conclusion that clean ligand exchange is not occurring. Because of the difficulty of removing OLA from the NP surface and the precedent in other NP systems of using weakly binding ligands as starting materials (such as trioctylphosphine and trioctylphosphine oxide), we decided to use a less stable intermediate ligand than oleic acid to access a variety of solution-phase PbS-L NPs. The intermediate ligand chosen was sodium 3-mercaptopropane sulfonate (MPS), which is known to remove OLA in a biphasic reaction to yield water-soluble PbS-MPS particles.[8] PbS-MPS particles are fairly stable (especially under anaerobic conditions) and could provide a nice platform for other biphasic ligand exchange reactions increasing the likelihood that successful exchanges would occur.

In order to afford the PbS-MPS NPs used in the subsequent ligand exchange reactions, a biphasic reaction of PbS-OLA NPs dispersed in toluene is reacted with an equal volume of the MPS dissolved in H_2O. The reaction proceeds under a N_2 atmosphere yielding PbS-MPS NPs. The PbS-MPS particles are cleaned to remove excess ligand and are stored as a solid under inert atmosphere to avoid decomposition. The PbS-MPS particles are then reacted in a second biphasic reaction with various thiol ligands in order to achieve solution processable PbS-L NPs (Figure 4.1). The ligands chosen for this investigation are listed in Table 4.1.
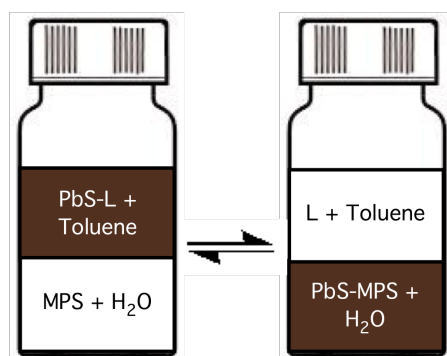
Figure 4.1. Schematic of the biphasic ligand exchange reactions used for PbS-OLA to PbS-MPS (forward reaction) and for PbS-MPS to PbS-L particles (backward reaction).

Ligand	Structure	Abbreviation
Methylbenzenethiol		MBT
Propanethiol		PT
Hexanethiol		HT
Dodecanethiol		DDT
Octadecanethiol		ODT

Table 4.1. Thiol ligands used in the biphasic exchange reactions with PbS-MPS NPs.

The secondary biphasic reactions are run with PbS-MPS NPs solublized in H_2O and excess organic ligand dissolved in toluene. Because these reactions are biphasic,

78

visual progress of the reaction is observed. Migration of the particles into the organic phase happens almost instantaneously for most ligands. The reactions were allowed to proceed for one hour to ensure phase transfer was complete. In some cases, migration of the NPs did not occur in one hour. In these instances, a second dose of ligand was added to the reaction mixture to promote the NP phase transfer.

The biphasic exchange yields PbS NPs with longer alkyl chain thiol ligands including octadecanethiol (ODT) and dodecanethiol (DDT); however, from a device standpoint, shorter ligands are more valuable than long chain, insulating ligands. For instance, it has been shown that substitution of oleic acid for shorter ligands has improved the photoresponse of simple devices made from NPs. Additionally, having solution-processable NPs with short chain ligands is desirable for large-scale production of devices and ease of characterization. Because of these considerations, the focus of this discussion is centered on coordination of hexanethiol (HT), propanethiol (PT) and methylbenzenethiol (MBT) to PbS NPs.

^{1}H NMR spectroscopy was used to monitor the binding of thiol ligands to the PbS NPs. Characteristic broadening and downfield shifts of ^{1}H signals provides a good spectroscopic handle to monitor the ligand exchanges. Protons on the ligand are broadened because of the geometrical constraints associated with binding to a large object that tumbles slowly on the NMR timescale; broadening of a signal provides clear evidence that the ligand is bound to the NP. Figure 4.2 shows the ^{1}H NMR spectrum for free hexanethiol ligand and NPs capped with hexanethiol. In the ^{1}H spectrum of the PbS-HT particles, all of the methyl and methylene proton signals through the ligand chain are broadened, indicative of ligand binding to the NP.

Although it is difficult to assign peaks due to overlapping signals of methylene protons, the shape of the signal at 1.3 ppm in the PbS-HT spectrum indicates that there is likely little or no thiol proton signal (which appears at 1.2 ppm). Because the distribution of the peak is more heavily weighted downfield, it is possible that the thiol was deprotonated in order for coordination to the NP to occur. (Note that the concentration of NPs in the NMR samples is important in order to resolve signals due to protons on the ligand chains. At minimum 10 mg of PbS-L samples were used to obtain the spectrum shown here.)
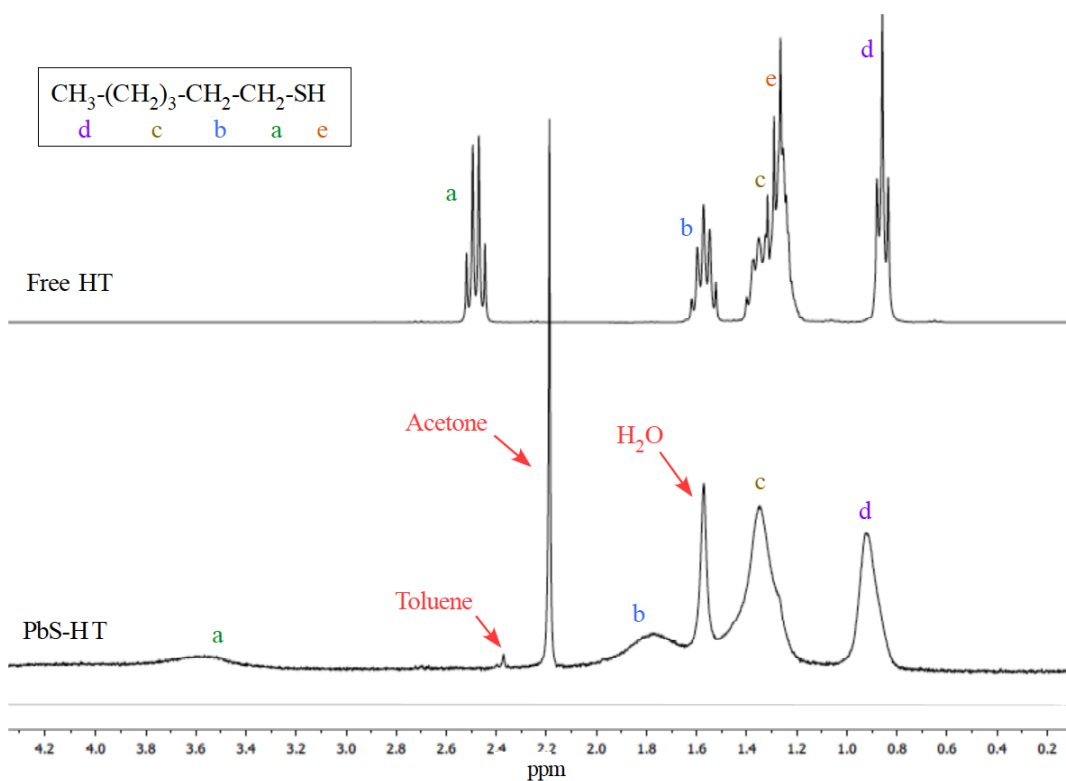
Figure 4.2. ^{1}H NMR spectra of free Hexanethiol ligand and ligand-exchanged PbS-HT NPs.

^{1}H NMR is an excellent technique to observe ligand binding to NPs; however, it does not provide information about NP size. Because electronic and optical properties of

80

NPs are tunable by size, a key parameter of ligand exchange reactions is the preservation

of the average particle size and the particle size distribution. For semiconductor NPs, the

particles have a characteristic absorbance for the creation of an exciton (a bound electro-

hole pair). In PbS and PbSe NPs, this exciton absorbance appears in the NIR. Figure 4.3

shows the NIR absorbance of the parent PbS-MPS and various as synthesized thiol-

exchanged particles. Note that there are small shifts in the exciton absorbance for some

of the NP samples.
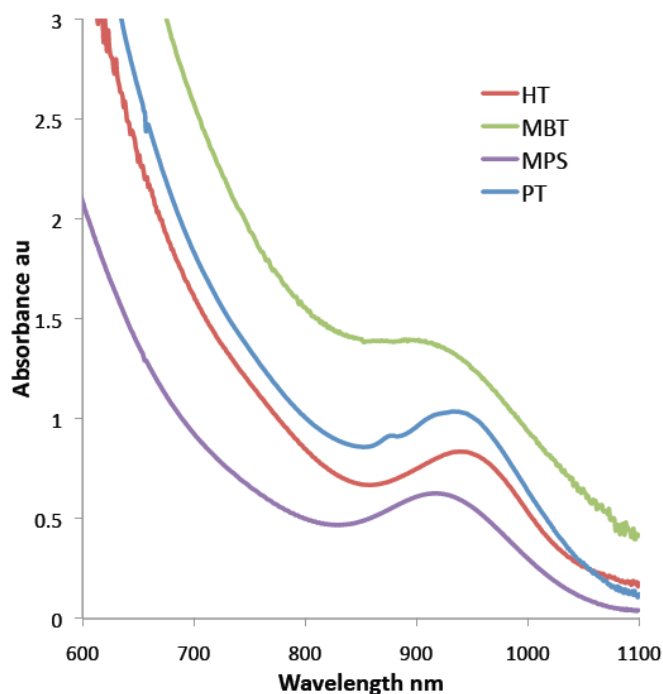
Figure 4.3. NIR absorbance spectra of various thiol-capped PbS NPs showing exciton absorbances near 930 nm.

It has been shown that PbS-MPS NPs are typically red-shifted from PbS-OLA

NPs after the first ligand exchange reaction.[8] This is most likely due to the change in

dielectric constant of the solvent.[8] Exchanging MPS for a different organic ligand and suspending the product NPs in low dielectric organic solvents should restore the exciton and show a blue shift of the particles relative to the PbS-MPS absorbance. This is not the case here. Because an appreciable amount of H_2O is typically observed in the ^1H NMR spectrum, the shifted spectra for exchanged particles could be due to the presence of H_2O in the solvent. Additionally, the red shift could indicate a slight size redistribution of the NPs. TEM images for the PbS-MPS and PbS-HT NPs as shown in Figure 4.x reveal that size distributions of both sets of particles are slightly broadened but within experimental error, and the sizes of the PbS-MPS and PbS-HT particles are similar (diameters of 2.5 ± 0.7 nm and 2.8 ± 0.7 nm respectively).
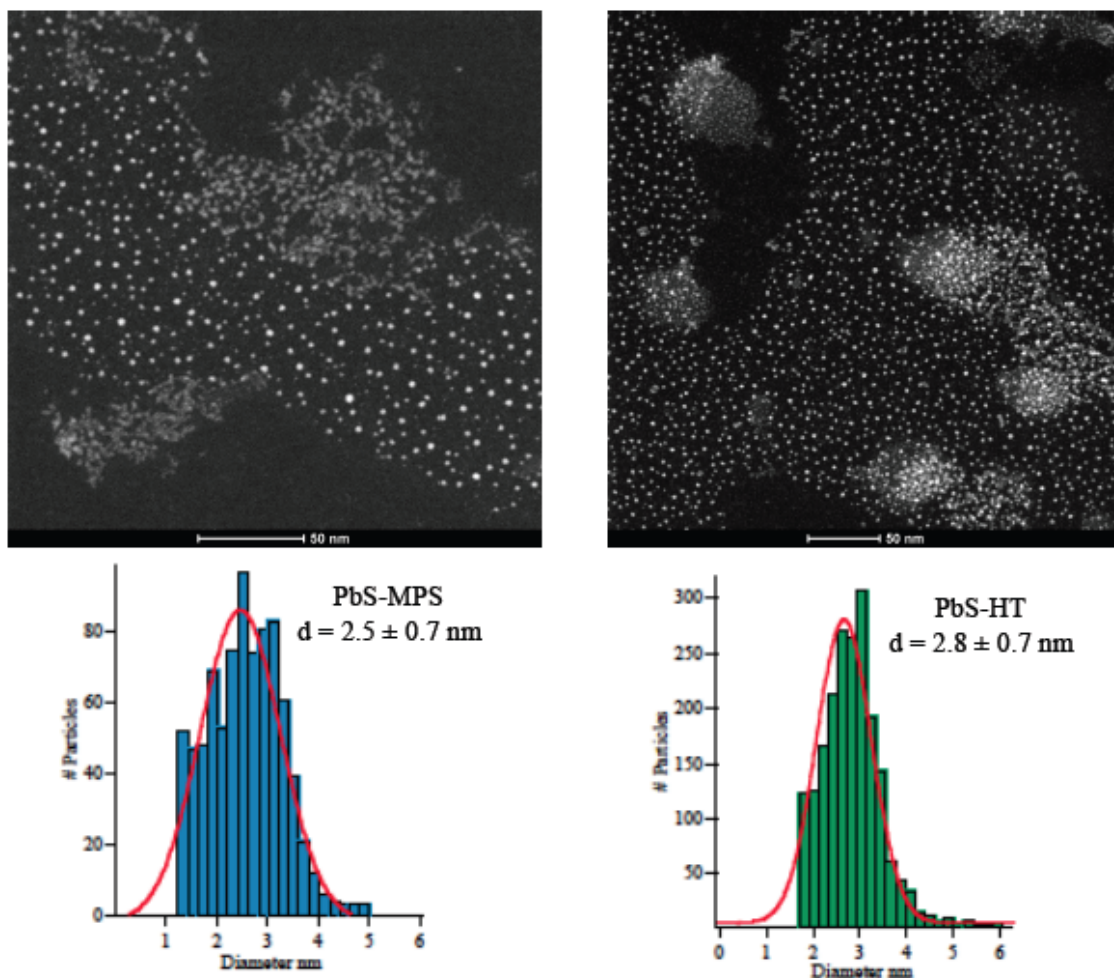
Figure 4.4. TEM images taken in STEM mode and resultant size distribution histograms of PbS-MPS (d = 2.5 ± 0.7 nm) and PbS-HT (d = 2.8 ± 0.7 nm) particles.

If H_2O is indeed transferred into the organic phase during the biphasic reactions, a legitimate concern is the transfer of some PbS-MPS particles or free MPS along with the H_2O. Although the ^1H NMR spectra recorded show only the desired bound ligands, we performed IR spectroscopy on the clean NPs to be sure no MPS was detected. The main absorptions seen in the IR spectrum of Figure 4.5 are due to C-H stretches (2956-2850 cm^{-1}) and C-H bends (1457 cm^{-1}, 1377 cm^{-1}). There is an absence of a strong absorption at ~1051 cm^{-1} that is indicative of an S-O stretch of MPS, thus it is unlikely that free MPS

or PbS-MPS is present in the extracted products. Lastly, the IR spectrum for PbS-HT particles lacks the thiol S-H stretch near 2250 cm^{-1} indicating the HT has indeed been deprotonated and is likely coordinated through to the NPs through a lead-thiolate bond.
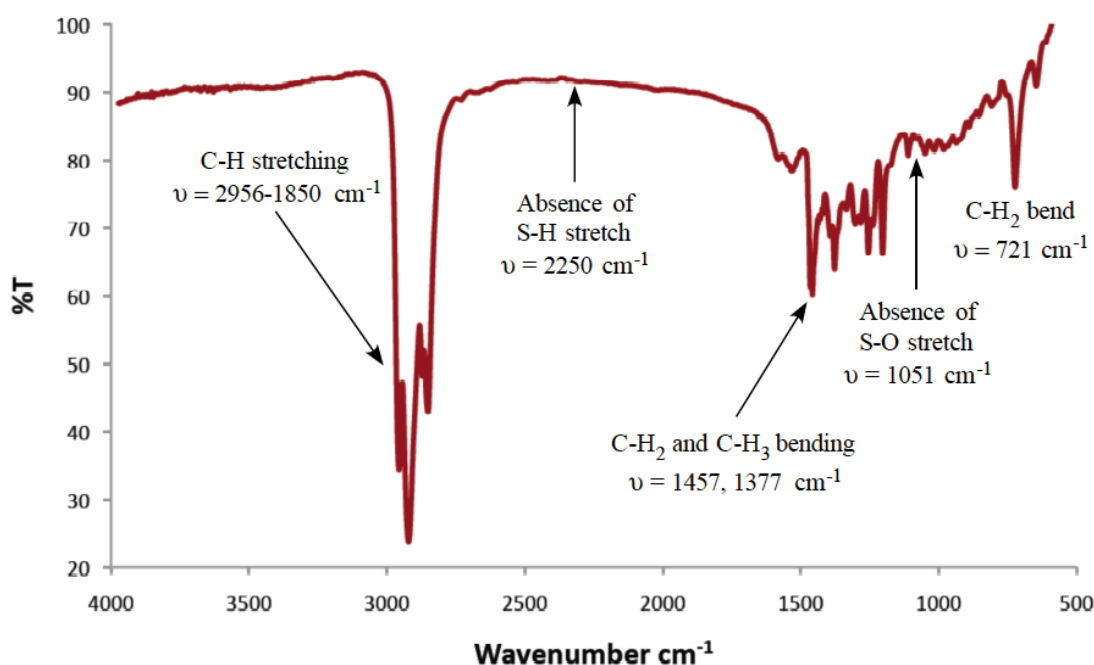
Figure 4.5. IR spectrum of a film of PbS-HT NPs on NaCl. The film was dried under a stream of N$_2$ to remove solvent prior to data acquisition.

Reactions with PT and MBT yielded initially soluble NPs, which were characterized by NIR spectroscopy as seen above (Figure 4.3). As the particles were cleaned to remove excess ligand, they became increasingly less soluble. Because of the incredibly low solubility of PbS-MBT and the presumed broadening of peaks, no signals were detected in the aromatic region of the ^{1}H NMR spectrum; however, a very small singlet was observed at 2.33 ppm, which could correspond to a shifted methyl proton signal of the coordinated MBT (uncoordinated MBT exhibits a singlet at 2.29 ppm). Additionally, the PbS-PT ^{1}H spectrum was dominated by dipropyl disulfide with shifts at

1.01 ppm, 1.71 ppm and 2.68 ppm (reported values are 1.0, 1.7 and 2.6 ppm respectively[16]). One broad singlet was observed at 0.84 ppm, which could be due to the terminal methyl protons of coordinated PT, but further characterization is necessary. Investigation into other possible cleaning conditions to preserve particle solubility are underway; however, these results suggest that there could be a finite ligand length associated with the solubility of PbS NPs.

4.4.2. Ligand Exchange With Amines

The ligand exchange reactions for amine-capped PbS NPs were run in the same manner as described for the thiol-capped particles. Despite the weaker Pb-N bond (with respect to a Pb-S bond), biphasic reactions with certain amine ligands proceeded to completion in the presence of excess ligand. Table 4.2 shows the amine ligands chosen for this investigation.
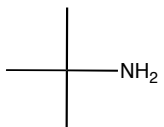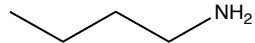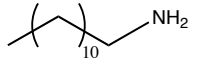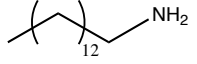
Ligand	Structure	Abbreviation
t-butylamine		*t*BA
n-butylamine		nBA
Dodecylamine		DDA
Tetradecylamine		TDA

Table 4.2. Various amine ligands chosen for biphasic reactions with PbS-MPS NPs.

In the biphasic amine reactions, long-chain amines including TDA and DDA proceeded to completion typically within minutes and yielded optically transparent NP solutions. Figure 4.6 shows the ^{1}H NMR spectrum of cleaned PbS-DDA particles.
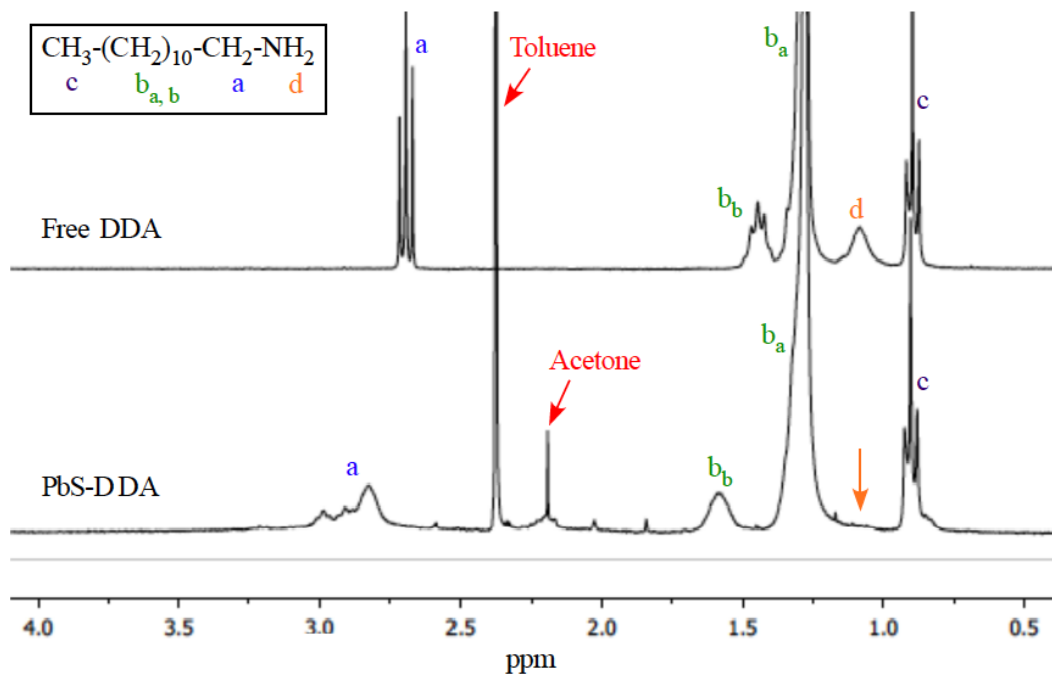
Figure 4.6. ^{1}H NMR spectrum showing free DDA ligand and ligand-exchanged PbS-DDA NPs. Note the disappearance of the amine protons at 1.2 ppm and broadening of signals close to the NP indicating coordination of DDA through the amine headgroup.

The ^{1}H NMR spectrum of PbS-DDA particles shows signals of the protons along the DDA chain. Perhaps the most convincing argument for the binding of DDA to the PbS NPs is seen from the disappearance of the amine ^{1}H shift at ~1.1 ppm in the PbS-DDA spectrum. If DDA binds to Pb, it must be through nitrogen coordination. In order to bind, a proton transfer from the amine to the previously bound MPS ligand would occur to liberate MPS from the NP. This results in a decrease (or disappearance) in the amine [1]H.

Additionally, the protons that are nearest to the NP when bound through the nitrogen atom show broadened and shifted signals. This is due to the geometrical constraints associated with binding to a large object that tumbles slowly on the NMR

timescale. Consequently, protons in the ligand chain that are further away from the particle are not shifted or broadened. For example, the terminal methyl proton signal is unaltered and appears as a triplet at 0.89 ppm. Singlets for residual H_2O, acetone and the methyl protons of toluene used for cleaning the NP samples are visible in the ^1H spectrum but do not obstruct the assignment of signals due to the bound ligands.

It should be noted that when removing excess ligand through the usual purification route, all of the amine-capped particles became increasingly less soluble. Because the Pb-N bond is relatively weak, it is assumed that not only excess ligand, but also bound ligand is removed in the purification process. In a similar manner, subjecting the PbS-amine solids to vacuum results in insoluble material presumably also due to the removal of bound amine ligand. Thus for optical measurements, excess ligand was left in the NP solutions.

Once again, while coordination of amines to Pb is easy to determine by ^1H NMR, the NMR spectrum shows no indication of NP size. NIR absorption spectroscopy was used to monitor the exciton absorbance for each ligand-exchanged batch of NPs. Figure 4.7 shows the NIR absorption spectra for various amine-capped PbS NPs compared to the parent MPS particles (and the as synthesized OLA NPs).
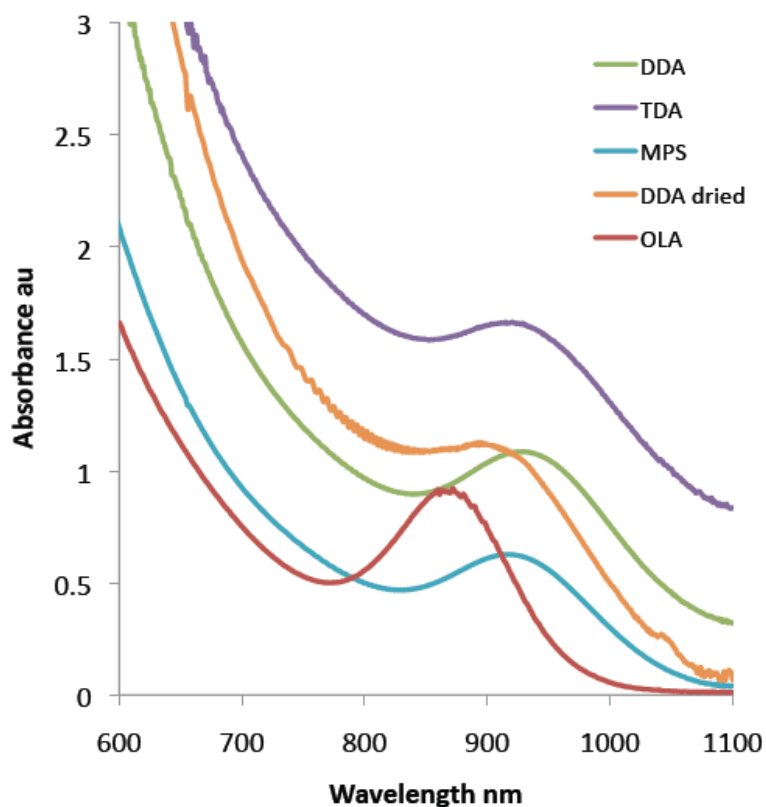
Figure 4.7. NIR spectra for parent PbS-OLA and PbS-MPS NPs and various amine-capped NPs via the biphasic exchange. Note some broadening of the exciton in the MPS reaction.

The NIR spectra for ligand exchanges from PbS-MPS to various amines show the existence of an exciton indicating the preservation of NP structure. Like in the thiol exchanges, it is apparent from the as-synthesized spectra of PbS-DDA and PbS-TDA particles (green and purple traces respectively) that the exciton absorbance is shifted from the parent batch of PbS-OLA particles (red trace). The previously stated hypothesis for this is that some amount of H_2O is brought into the toluene phase presumably through micellular interactions with the large excess of free DDA. Because it is more difficult to clean the amine-capped particles, an alternative technique was used to determine if the red shift of the exciton peak was actually due to the presence of H_2O altering the

89

dielectric environment of the NPs. To test this, the as-synthesized PbS-DDA particles

were dried over a small amount of anhydrous $MgSO_4$. The $MgSO_4$ was then removed by

running the NP solution through a 0.22 μm filter. As seen in Figure 4.6, a blue shift of

the exciton absorbance from 927 nm to 894 nm (orange spectrum) was observed after the

first drying. This indicates that the preservation of the red shift after ligand exchange is

indeed likely due to the presence of H_2O in the extracted NPs.

For the device implications listed above, short amine ligands were reacted with

PbS-MPS. While shorter thiol ligands like hexanethiol and propanethiol yielded solution

processable NPs, no reaction was observed with *t*-butylamine or n-butylamine over the

course of 12 hours. It is possible that *t*-butylamine is too sterically bulky to sufficiently

bind to the NP surface to induce the phase change; however, n-butylamine has greatly

reduced steric bulk and still shows no sign of biphasic reaction. Ideally, if the NPs are

capped with only the amine ligands, the surface becomes hydrophobic and the NP

transfers phase into the organic layer. A standing hypothesis for the lack of reaction seen

with these short amines is that because both *t*-butylamine and n-butylamine are miscible

with H_2O and the organic phase, perhaps there is no driving force for full substitution of

the NPs and thus, the NPs do not transfer phase.   Further investigation into reaction

conditions for the substitution of MPS for short chain amines is underway.

4.5. CONCLUSIONS

This chapter highlights the versatile ligand exchange reactions of PbS-MPS NPs

with various organic ligands to afford a wide variety of ligand-substituted PbS NPs. The

MPS intermediate ligand was chosen because the biphasic MPS reaction successfully removes oleic acid from the natively synthesized PbS-OLA particles. Additionally, the MPS ligand provides a nice platform for a second series of biphasic reactions, affording a convenient synthetic route to other organically passivated NPs. Long chain amines and an assortment of alkyl thiols (as well as a few aromatic thiols) were substituted onto the PbS NPs via the biphasic route. In all, this chapter provides a much-needed exchange route to variously capped PbS NPs which can be further studied for the direct effect of the ligand shell on processes that are important to the implementation of NPs in semiconductor devices. In Chapter V, the use of this synthetic route afforded NPs to study the affect of the type of donor atom on MEG processes.

CHAPTER V

LIGAND DONOR ATOM EFFECTS ON MEG IN PbS NANOPARTICLES

5.1. INTRODUCTION

As described in Chapter III, the surface ligands of a semiconductor nanoparticle (NP) can have an effect on the generation and decay of charge carriers within the NP.[1-4] In particular, within Chapter III, a detailed analysis of the difference in multiple exciton generation (MEG) for oleic acid-capped PbS NPs versus the same NPs capped with the sodium 2, 3-dimercaptopropane sulfonate was determined. While there was no appreciable difference in MEG yield, there was an appreciable difference in the decay rates of multi and single excitons. Working hypotheses of these distinct dynamical differences are attributed to two ligand characteristics: 1) the difference in ligating atom between the two ligands (oxygen versus sulfur) or 2) the secondary ligand structure affecting the delocalization of the excitons within the NPs (organic versus ionic ligand shells).

The research discussed in this chapter details ligand effects on MEG specific to the identity of the ligand donor atom (hypothesis 1 above). In this investigation, oleic acid, oleylamine, dodecylamine and dodecanethiol ligands were investigated on PbS NPs to determine if the coordinating atom of the ligand shell affects the measured parameters

of MEG. In order to investigate this phenomenon, dynamical measurements were taken

using transient absorption (TA) spectroscopy. This technique probes the ultrafast decay

components for single and multiple excitons as related to the induced change in optical

density due to the measured time-dependent populations of excitons after excitation.

Analysis of the raw kinetic data yields information exciton decay dynamics and MEG

quantum yields (QYs), with respect to the ligand shell. This material is coauthored with

Dr. David R. Tyler who acted as my advisor during the investigation.

5.2. CHOICE OF LIGANDS

Because of the ease of solvation of long alkyl chain-capped NPs and the biphasic

synthesis developed for the long chain ligand exchanges, the ligands chosen for this study

were oleylamine (OLAm), oleic acid (OLA), dodecanethiol (DDT) and dodecylamine

(DDA). Direct comparisons of MEG yield and exciton recombination rates can be made

regarding the ligating atom (donor atoms) of these particular ligand sets. The carboxylate

binding of OLA can be directly compared to the amino functionality of OLAm while

DDT and DDA yield a comparison of sulfur versus nitrogen-based functionalities.

Using OLAm and DDA which have identical secondary ligand structures to OLA and

DDT respectively allows for a general comparison of all three donor headgroups on

MEG. Additionally, previous studies of intraband electron dynamics have been reported

on CdSe NPs in the presence of many of these ligands.[2] In the CdSe NPs, the affect of the

surface on the intraband relaxation of electrons was hypothesized to result from changes

in surface polarity where DDA and OLA exhibited faster intraband relaxation than

amines or phosphines. It should be noted that no discussion of MEG yield or interband (exciton recombination) dynamics was discussed in the above investigation.

5.2.1. Lauric Acid Ligand Exchange Reactions

Incidentally, because of the ease of exchange for both PbS-DDT and PbS-DDA particles, the initial goal of this study was to compare lauric acid to these ligands. This would ensure a direct comparison of the donor atoms of the ligand shell with identical secondary structures. It was discovered, however, that via the same exchange route, lauric acid did not undergo biphasic ligand exchange. Even in the case of extremely high ligand concentration (> 1000-fold excess by weight), no migration of PbS-MPS particles to the organic phase was observed after one month.   In an attempt to drive the reaction forward, lauric acid was deprotonated in toluene using NaH. This resulted not unexpectedly in an unusable gel.[5] Ion exchange with KCl was performed to obtain the micelle phase of deprotonated lauric acid. This laurate mixture was used to try to obtain the PbS-LA particles. Unfortunately, the reaction mixture remained in a micelle phase and was unable to be separated using conventional methods without destroying the integrity of the NPs (i.e. creating in an insoluble white precipitate). Because of the difficulty associated with the lauric acid exchange, the investigation of oxygen as a donor atom was accomplished through the use of oleic acid-capped particles (PbS-OLA) using oleylamine and dodecylamine ligands to eliminate differences in secondary structure comparisons to the other ligands.

5.3. EXPERIMENTAL METHODS

5.3.1. Synthesis of PbS-OLA NPs

Solvents in this investigation were dried on commercial columns of CuO followed by alumina under argon atmosphere or subjected to several freeze-pump-thaw cycles to eliminate oxygen prior to use. H_2O used within these experiments was degassed by purging with N_2 and exposed to vacuum prior to use. The reagents and solvents were obtained from Sigma-Aldrich and used as received. Unless otherwise stated, all manipulations were carried out in a N_2-filled glove box by Vacuum Atmospheres Co. or on a standard Schlenk line using N_2.

The lead sulfide NPs were synthesized according to literature precedent.[6] In short, the oleic acid-capped particles were prepared via a solution containing 4 ml octadecene and 4 ml oleic acid. PbO (0.3 g) was added to this solution which was heated under vacuum to 100 °C for 30 minutes. The temperature of the lead precursor solution was raised to a desired injection temperature (100 ºC to 150 ºC) and allowed to equilibrate for 30 minutes.

Simultaneously, a sulfur precursor solution of 0.167 ml hexamethyldisilathiane and 4 ml octadecene was degassed under nitrogen. After the lead solution was thermally equilibrated, the sulfur precursor was quickly injected into the lead solution. The mixture was then allowed to cool to room temperature. The NP solutions were cleaned of excess ligand through repeated cycles of precipitation in acetone, centrifugation and

resuspension in toluene.[6] A Perkin-Elmer Lambda 19 UV/vis/NIR spectrophotometer was used to determine the Near Infrared (NIR) absorbance of the particles.

5.3.2. Ligand Exchange

Ligand exchange on the PbS-OLA particles to afford the intermediate particles was accomplished according to literature precedent.[7] A solution of PbS-OLA NPs was prepared (typically between 8 and 25 mg/ml) and combined with an equal volume of a 200 mM solution of 3-mercaptopropane sulfonate (MPS) in H_2O. The biphasic solution was degassed under a stream of N_2 and stirred until the particles migrated from the organic phase to the aqueous phase (1 hr). Centrifuging for 10 minutes at or above 3500 rpm broke emulsions formed during the phase transfer reactions. The PbS-MPS particles were cleaned of excess ligand by precipitation with acetonitrile, centrifugation, and resuspension in H_2O.

A second biphasic reaction yielded the desired organically soluble ligands with varying ligating atoms. A typical ligand exchange procedure was run with a 400 mM solution of ligand in toluene. The ligand solution was added to an equal volume of PbS-MPS nanoparticles suspended in H_2O at a concentration of 5-15 mg/ml. The toluene-solublized NPs were extracted from the aqueous layer and diluted to an appropriate concentration. In order to ensure the solubility of the NPs used in the transient absorption experiments, excess ligand was left in the NP solutions. The exciton absorbance of each NP sample was determined by NIR spectroscopy (Perkin-Elmer Lambda 19 UV/Vis/NIR spectrometer).

5.3.3. Transient Absorption Spectroscopy

The transient absorption experiment used to measure the MEG yield and exciton recombination in the NP samples is described in detail in Chapter II.

5.3.4. Sample Preparation and Handling

Oleic acid-capped NPs were used as received by placing a sample into a 2 mm path length cuvette containing a stir bar and filling the headspace with nitrogen. The ligand-exchanged NP samples were placed into 2 mm path length cuvettes equipped with stir bars while in a nitrogen-filled glovebox. These cuvettes were sealed with a PTFE stopper and removed from the nitrogen box where they were then wrapped with PTFE (Teflon) tape and sealed with paraffin wax. All reported transients for the determination of MEG yields and appropriate time constants in this study were taken while the samples were stirring to prevent photoionization of the samples which would result in overestimation of MEG yield and complication of the resolved exciton dynamics.[8]

5.4. RESULTS AND DISCUSSION

A ligand exchange reaction was carried out on PbS-OLA NPs to afford intermediate particles capped with 3-mercaptopropane sulfonate (PbS-MPS).[7] Once the PbS-MPS NPs were obtained, reverse biphasic ligand exchange reactions were run to afford the desired organic ligand functionality. The organic functionalized particles were

used as synthesized in the MEG experiments. The excess ligand in the reaction mixtures was deliberately not removed to ensure that the particles remained solublized throughout the TA experiments. Additionally, having excess ligand in the solutions should force the solution equilibrium toward the binding of ligands to the NPs, ideally creating well-passivated NP samples for MEG study.

OLA, DDA, DDT and OLAm ligands were used to determine the effect of the donor atom on the generation and decay of excitons in PbS NPs. From the absorption spectrum, the sizes of the NPs were calculated according to the formalism of Moreels, *et. al.*[9] All of the NP sizes were determined to be between 4.9 and 5.2 nm in diameter (PbS-OLA = 4.9 ± 0.4 nm; PbS-DDA, PbS-DDT = 5.1 ± 0.4 nm; and PbS-OLAm = 5.2 ± 0.3 nm). Figure 5.1 shows the absorption of the 1st exciton in the NIR for each sample analyzed.
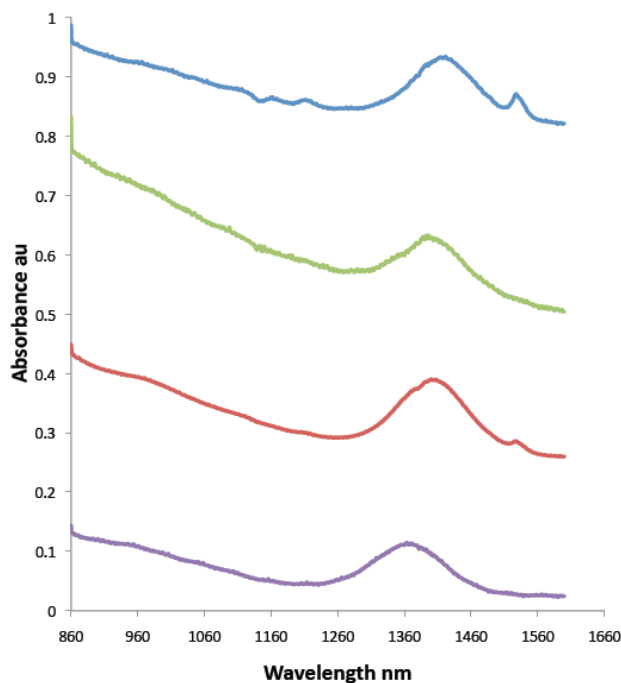
Figure 5.1. Representative NIR absorbance spectra showing the 1st exciton absorption (1S$_h$-1S$_e$) for PbS-OLA nanoparticles (purple) compared to ligand exchanged PbS-DDA (red line), PbS-DDT (green) and PbS-OLAm (blue) NPs.

5.4.1. MEG With Oxygen and Nitrogen Donor Atoms

The first investigation with regard to the effect of the ligand donor atom on MEG was the substitution of oleylamine (OLAm) for oleic acid (OLA) to investigate nitrogen and oxygen coordinating atoms. Kinetic traces for the excitation of each sample of PbS NPs were collected at various pump fluences with photon energies both below and above the threshold for MEG in PbS nanocrystals while the probe energy in each case was tuned to the NIR exciton absorbance of the NP samples. The sub-MEG threshold traces are collected in order to model the decay of the single and biexciton signatures in the absence of MEG. For all of the samples investigated herein, the sub-threshold excitation

wavelength of 800 nm corresponds to < 2E_g whereas the above threshold excitation (400 nm) corresponds to ~3.5E_g for each NP sample (typical 1st exciton absorbance between 1340 nm and 1440 nm).

The traces for both PbS-OLA and PbS-OLAm particles in the absence of MEG and in the presence of MEG are shown in Figures 5.2 and 5.3 respectively. From the sub-threshold, variable fluence measurements, the time constants for the single exciton decay (τ_X) and the biexciton decay (τ_{XX}) are extracted as global parameters according to the description of Ellingson, *et. al.*[10] The values for the extracted biexciton time constants are 250 ps for PbS-OLA NPs and 89 ps for PbS-OLAm NPs as reported in Table 5.1.
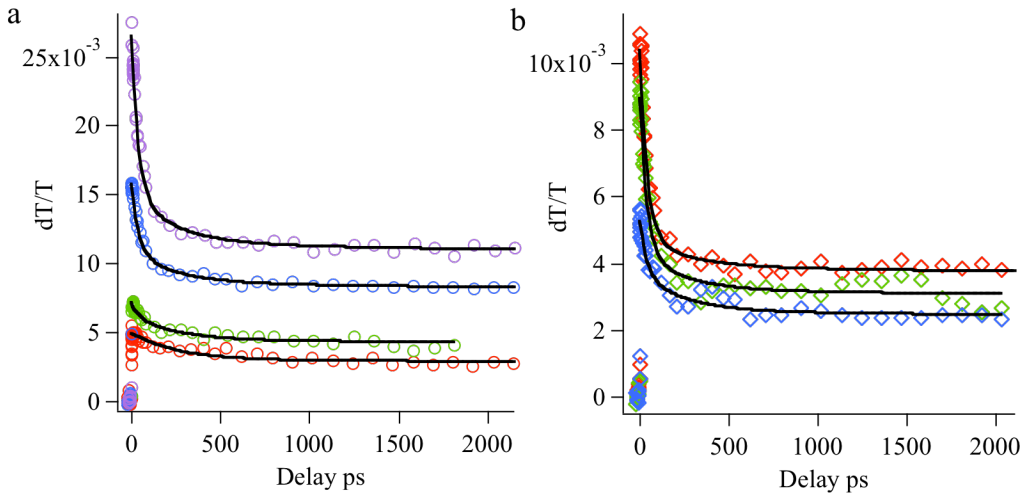
Figure 5.2. Variable fluence transient decay curves and best curve fits for PbS-OLA NPs excited at (a) 800 nm (1.55 eV, 1.68E_g); (b) 400 nm (3.11 eV, 3.35E_g).

100

Figure 5.3. Variable fluence transient decay curves and best curve fits for PbS-OLAm NPs excited at (a) 800 nm (1.55 eV, 1.68E_g); (b) 400 nm (3.11 eV, 3.35E_g).

In addition to the single and biexciton recombination rates, the MEG quantum yields (QY) were also determined for PbS-OLA and PbS-OLAm NPs. In determining QY, the ratio of short and long time signal (A/B, 3 ps and 1500 ps respectively) is plotted as a function of the input photon fluence measured at the front face of the sample cuvette (Figure 5.4a and 5.4b). Fits of the calculated A/B ratios for 800 nm excitation assume Poisson statistics for the absorption of photons by the NPs and are fit by Equation 1 as suggested by Ellingson *et. Al.*

$$\frac{A}{B} = \frac{QY\, \delta\, J_{pump}\, \sigma_{pump}}{\left(1 - \exp\left(-J_{pump}\, \sigma_{pump}\right)\right)} \qquad 1$$

The curves for 400 nm excitation are non-Poissonian but are also fit to Equation 1 by allowing for the adjustment of the quantum yield (QY), which accounts for the enhanced amplitudes due to MEG. By extrapolating these fits back to low photon

101

fluences (10^{12} photons cm^{-1}) and dividing out the contribution of the sub-MEG threshold excitation, the MEG QY for each particle set was determined. The MEG yields are reported in Table 5.1 and shown in Figure 5.4. A discussion of the MEG dynamics and respective yields is presented later.

Figure 5.4. Ratios of early to late time signals versus the input pump photon fluence at the front face of the sample cuvette (J_{pump}) for PbS-OLAm and PbS-OLA.

5.4.2. MEG With Nitrogen and Sulfur Donor Atoms

To ascertain the effect of the coordination of nitrogen versus sulfur, ultrafast decay curves for batches of PbS-DDA and PbS-DDT particles were obtained in the same manner as outlined above. The raw traces for both excitation wavelengths of each particle sample are shown in Figures 5.5 (DDA) and 5.6 (DDT) for various input pump fluences. The same global fitting routine as described for the PbS-OLA and PbS-OLAm NPs was employed, and the time constants for single and biexciton decays were extracted

from the raw data. The time constants determined from the global fits are reported in

Table 5.1.
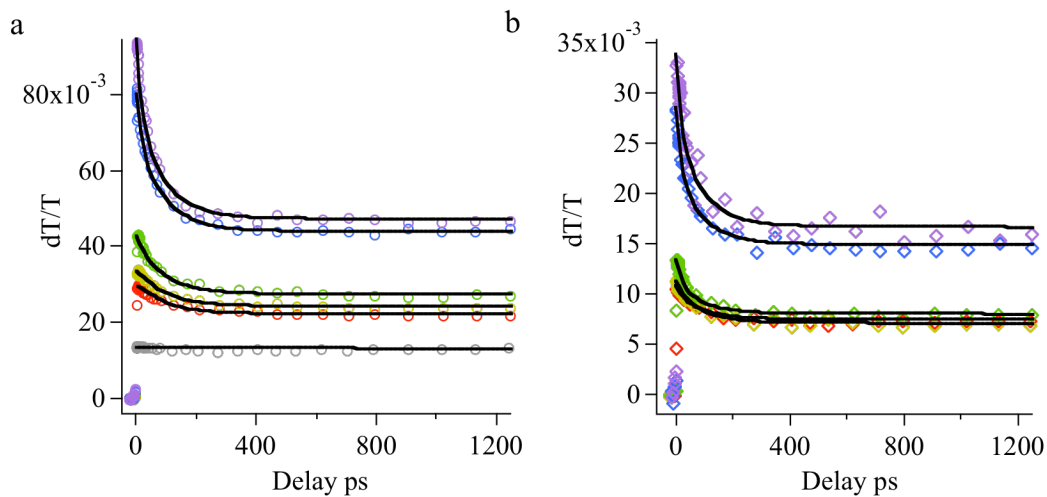
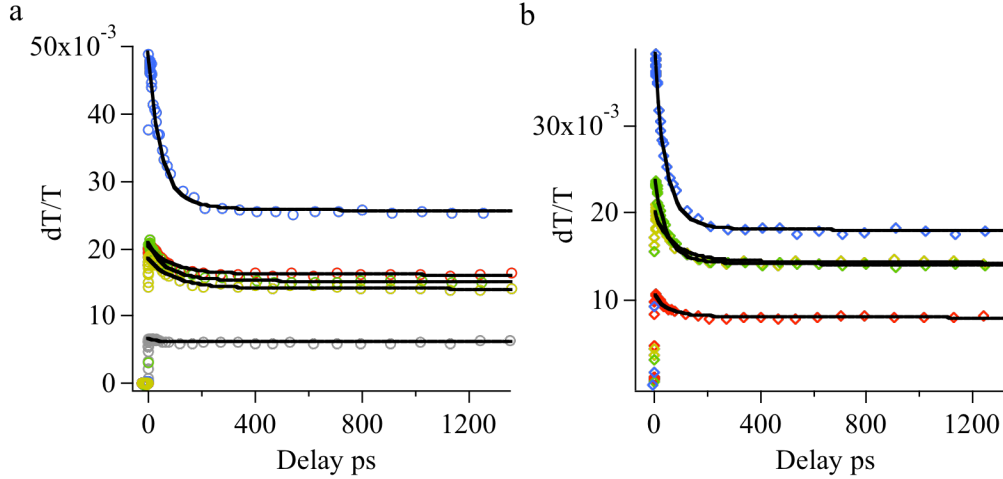**Figure 5.5.** Variable fluence transient decay curves and best curve fits for PbS-DDA NPs excited at (a) 800 nm and (b) 400 nm.
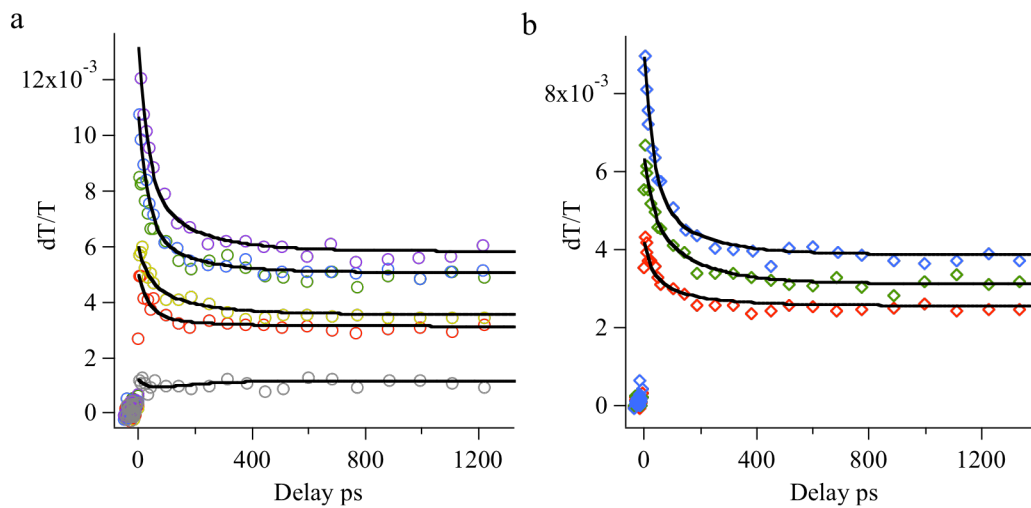
Figure 5.6. Variable fluence transient curves and curve fits for PbS-DDT under (a) 800 nm and (b) 400 nm excitation.

Also shown in Table 5.1 are the MEG quantum yields (QYs) for the PbS-DDA and PbS-DDT particles. The MEG QY for these two sets of NPs was determined in the same manner as described above. The respective plots of A/B ratios as a function of photon fluence are shown in Figure 5.7. It is interesting to note that the MEG yield is effectively nonexistent for the PbS-DDT sample investigated here.

Sample	τ_{XX}/ps	τ_X/ns	MEG Yield
PbS-OLA	250 ± 13	61	1.1 ± 0.2
PbS-OLAm	89 ± 20	90	1.3 ± 0.2
PbS-DDA	88 ± 4	160	1.3 ± 0.2
PbS-DDT	165 ± 20	110	1.0 ± 0.3

Table 5.1. Time constants for biexciton (τ_{XX}) and single exciton (τ_X) recombination and MEG quantum yields for variously capped PbS-NPs.
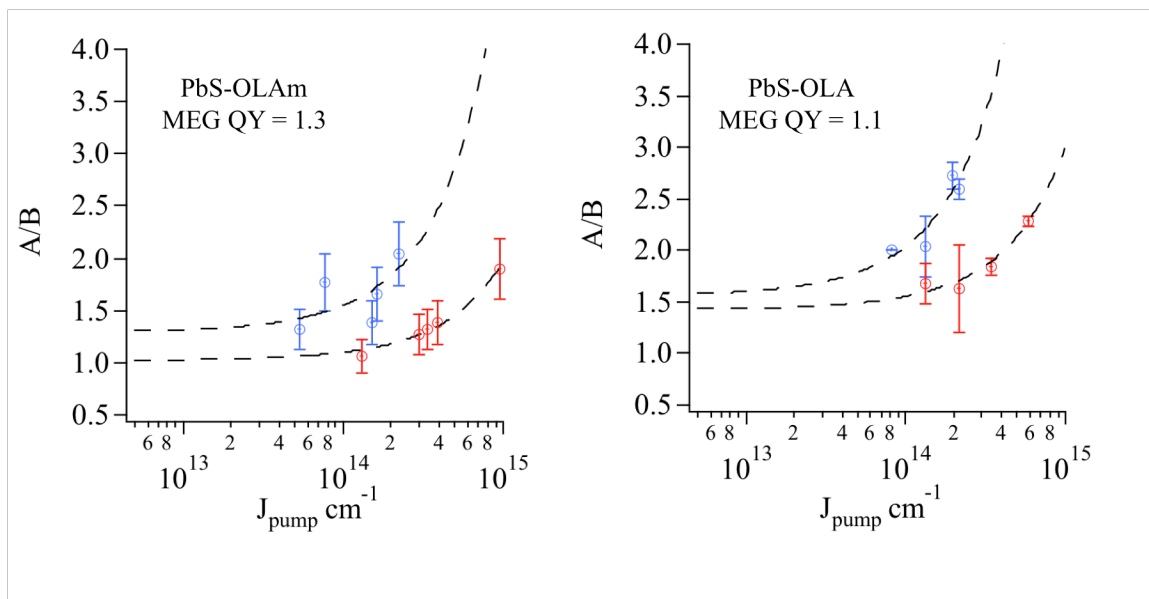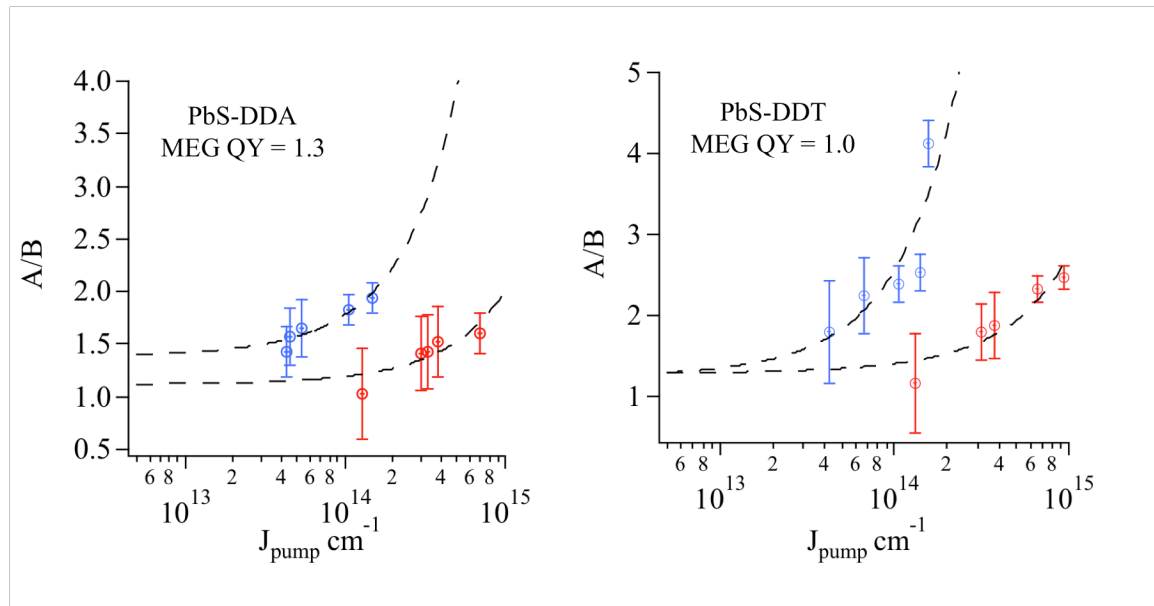

Figure 5.7. Ratios of early to late time signals versus the input pump photon fluence at the front face of the sample cuvette (J_{pump}) for PbS-DDA and PbS-DDT particles.

104

In putting this information together, a comparison of the two amine-capped sets of particles can be made in order to determine the effect of long chain amine ligands on MEG. For the PbS-DDA particles, the time constant for biexciton decay is the same as for the PbS-OLAm particles (88 ps). It is not unreasonable that the biexciton time constant for both of the amine-capped particles is the same within experimental error since the two ligand structures are quite similar. The only difference in the secondary ligand structure of OLAm and DDA is the unsaturation at the 9th carbon in OLAm. This unsaturation is likely too far removed from the surface of the particle to be of any consequence to exciton dynamics or MEG yields. Because of this result, an analogous comparison between OLA and DDT can be made due to the fact that the secondary ligand structure differences in OLA and DDT should be negligible with respect to MEG.

Comparing all of the data with regard to the ligand donor atom reveals that the biexciton decay is strongly influenced by the ligand shell. The trend observed is that the natively synthesized OLA particles show the longest biexciton decay followed by the thiol-passivated particles while the amine-coated NPs show an even larger reduction in the biexciton time constant. In thinking about the results, the biexciton decay must follow a trend related to the ligand donor atom.

The difference seen in decay rate between PbS-OLA and PbS-DDT mimics that of the exchange of OLA for 2, 3-dimercaptopropane sulfonate as described previously.[3] This suggests that the sulfur donor atom could be responsible for the decreased rate of biexciton decay. The previously reported hypothesis suggests that the difference in electronegativity of the sulfur and oxygen atoms alters the delocalization of the charge carriers over the surface of the particle and may be responsible for the differences in

exciton decay rates. In terms the electronegativity of the donor atom, the fast decay of biexcitons for the amine-capped particles is slightly puzzling. The Pauling electronegativity for nitrogen is between that of oxygen and sulfur.[11] Therefore, if this hypothesis holds true, the PbS-amine decay rates should fall between PbS-OLA and PbS-DDT. Because this is not the case, an alternative explanation is probably necessary.

Another hypothesis comes from the investigation of intraband dynamics of CdSe NPs using similar ligands. The trend in the electron relaxation follows the polarity of the metal-ligand bond according to hard-soft acid-base theory (HSAB).[2] In HSAB theory, the trend in polarizability of the lone pairs on the deprotonated ligands dictates that carboxylates are hard bases while thiolates are soft. Because the Cd^{2+} ions are soft acids, the ligand-metal bond for thiols is less polarizable leading to lengthened intraband relaxation for the CdSe NPs. Pb^{2+} ions are also borderline soft acids. This leads to the trend that the polarity of the metal-ligand bonds in the PbS NPs should be as follows: Pb-O > Pb-N > Pb-S.[12,13] If the exciton recombination follows the trend of HSAB as in the CdSe investigation, the dynamics of the amine-capped particles should lie between that of PbS-DDT and PbS-OLA. This is not the case. Additionally, the results of this investigation follow the opposite trend in bond polarity for PbS-OLA and PbS-DDT NPs thus the recombination of biexcitons in PbS NPs does not necessarily correlate in the same manner to metal-ligand polarizability as with the CdSe NPs.

Another consideration for the dynamical differences observed with OLA, OLAM, DDA and DDT ligands on MEG is the solution equilibrium of ligand binding. For the solution equilibrium argument, it is possible that the ligands are binding and dissociating from the NP during the TA experiments. OLA is a bidentate ligand requiring the

dissociation of both oxygen atoms from the surface to yield unpassivated NPs; however, the DDA, OLAm and DDT ligands are all monodentate where only one dissociation event must take place for the desorption of a ligand. Because excess ligand was present in the solutions, this equilibrium should lie toward the binding of the ligands to the NPs; however, the amine and thiol NPs crash out of solution within a few days after the TA experiments whereas PbS-OLA NPs do not. Thus, the decreased recombination rates could be accounted for by the dissociation of ligands creating a fraction of trapped electrons or holes in the NP sample volume. This should be seen in the low fluence, sub-MEG threshold excitation curves; however, these curves exhibit the usual flat dynamics attributed to single exciton recombination rendering this hypothesis unlikely. Nonetheless, an investigation on this equilibrium argument by monitoring MEG and trapping rates as a function of ligand concentration in solution could provide information on the amine systems. Additionally, MEG experiments on NP films with these ligands would discern whether or not this solution equilibrium affects MEG (provided the ligands are of similar sizes and do not allow for changes in interparticle distances).

A final explanation for the differences in biexciton dynamics is the pKa of the ligands. The pKa trend for the ligands follows the decay trend where amines are much more basic than the compared thiols and carboxylic acids. With this in mind, the pKa of amines in water is nearly 35 in comparison to 15 for thiols and nearly 2 for carboxylic acids. The Despite the fact that this changes in organic solvent, it is unlikely that deprotonation of the amine occurs before coordination to the NPs. In this case, the NP may in fact have a charged surface leading to the decrease in the biexciton recombination time constant for the amine-capped particles.

5.5. CONCLUSIONS

The results of this investigation confirm that biexciton decay rates in PbS NPs are altered by the NP surface. While the MEG yields are similar for the ligand-exchanged particles, the observed trend in biexciton decay rates obeys the following order: DDA=OLAm > DDT > OLA. While the differences in MEG dynamics still remains a mystery, a previous hypothesis regarding the electronegativity of the donor atom effecting MEG dynamics still holds for sulfur and oxygen in this investigation. Amines were chosen to bridge the gap in electronegativity to prove this hypothesis; however, the recombination of biexcitons in the amine-capped particles does not follow the electronegativity trend. It is possible that the amines dissociate from the NP surface more rapidly than OLA or DDT where an increase in the amount of surface trapping can account for the faster decay rates; however, this is unlikely as the low fluence, sub-MEG threshold dynamics do not reveal large signatures due to enhanced surface trapping. Lastly, biexciton decay dynamics appears to trend with ligand pKa which may reveal that when the amines are bound to the NP surface, they bind without losing a proton yielding a charged NP surface. This charged surface might be responsible for the observed decrease in biexciton lifetime for the amine-capped particles. Further investigation on the role of amine ligands is necessary to conclude the true effect of the donor atom on MEG in PbS nanoparticles.

CHAPTER VI

CONCLUSIONS AND OUTLOOK

6.1. CONCLUSIONS

This dissertation outlines the phenomenon of multiple exciton generation (MEG) in PbS nanoparticles (NPs) from the standpoint of enhancing the conversion efficiencies of solar cells. Because MEG creates multiple charge carriers per photon absorbed in semiconductor NPs, it has been suggested as a method to bypass the inherent limits of photoconversion for bulk solar cells, the Shockley-Queisser limit. Before NPs can be optimized for incorporation into devices, however, an understanding of the parameters that affect MEG must be investigated. This dissertation focused on MEG in PbS NPs and the subsequent recombination of excitons as a function of the NP surface, or ligand shell.

A general conclusion of the ligand manipulations of PbS NPs is that any time oleic acid (OLA) is substituted off of the NPs, the measured biexciton decay constant is decreased meaning that biexcitons recombine faster for all of the ligand-substituted particles than for the parent particles (PbS-OLA). While the true origin of this phenomenon still remains unknown, the hypothesis for this enhanced decay rate is that the ligand-substituted particles do not passivate the NP surface as efficiently as OLA leading to an increase in the number of available surface-mediated decay routes.

A study on the substitution of an ionic ligand (2, 3-dimercaptopropane sulfonate, MPS) on PbS NPs revealed that while the MEG yield does not change for the PbS-MPS particles, the biexciton decay rate is nearly doubled with respect to the PbS-OLA particles. Additionally, the substitution of OLA for dodecanethiol (DDT), another thiol-bound ligand in a separate investigation, showed a similar decrease in the biexciton time constant leading to the conclusion that the ligating atom might be responsible for much of the change in biexciton decay rates for NPs. Substitution of two different amines for OLA leads to even faster decay rates of biexcitons than that of thiol substitution. The trend seen in the increased decay rates for the substituted NPs has been hypothesized to follow that of ligand binding efficiency where the amine ligands are least likely to sufficiently passivate the NP due to weak nitrogen coordination to lead. While thiols should bind well to the PbS NP surface, they have been shown to decompose and thus are likely not as stabilizing as the bidentate coordination of OLA. Interestingly, the MEG yields for the NPs investigated in this dissertation do not vary much at all indicating that the generation of excitons relies on the core of the NP while recombination is a surface-mediated process.

As a brief interlude, the stability of OLA-capped particles was indirectly investigated as a function of the ligand exchange process. PbS-OLA NPs are robust, thus ligand exchange from OLA is not a trivial matter. To circumvent the issues with removing OLA from the NPs, biphasic reactions were used. By utilizing ionic ligand intermediates, a host of ligand-altered NPs were synthesized for the MEG studies.

6.2. OUTLOOK

There are a number of reasons to continue identifying and investigating parameters that affect MEG in NPs. With the information gleaned from the experiments performed in this dissertation, ligand exchange for thiols and amines may not be the best route to modification of the NP surface for solar processes due to the decrease in biexciton lifetimes associated with the surface modification. Because of the extended biexciton lifetimes seen for well-passivated carboxylic acid derivitized NPs, an interesting study would include synthesizing a host of differently substituted carboxylic acid ligands for investigation on MEG. By imparting electron withdrawing or electron donating capability to the NP surface, perhaps the dynamics of MEG could be selectively tuned. For example, selective ligand substitution could lead to bifunctional particles where excitons are spatially separated in the NP leading to easier extraction of the charge carriers. Lastly, if ligands with reactive substituents such as chlorides or bromides are placed on the NP surface, further chemistry could be performed on the NPs in order to tether them to polymer host matrices in order to minimize interfacial losses and facilitate carrier extraction leading to enhancements in cost-effective solar devices.

APPENDIX

APPLICATION OF THE TACHIYA FLUORESCENCE QUENCHING MODEL TO DESCRIBE THE KINETICS OF SOLID-STATE POLYMER PHOTODEGRADATION

A.1. INTRODUCTION

One strategy for reducing the persistence of plastics in the environment is to use plastics that photochemically degrade after use.[1-4] Mechanistic knowledge of polymer degradation reactions is essential for designing such plastics. Many mechanistic studies of polymer photodegradation include a kinetics investigation, and the interpretation of the kinetics data can reveal important insights about the environmental and molecular parameters that affect the onset of polymer degradation and the degradation rates.[5,6] Several challenging experimental problems hinder the rigorous experimental mechanistic exploration of polymer photodegradation.[7] To circumvent these mechanistic complexities and therefore make it less difficult to interpret data and obtain fundamental insights, we use polymers that have metal-metal bonds incorporated into the polymer backbone.[7,8] A thorough explanation of why we use these polymers is found in our previous publications[5-11] so it is simply noted here that irradiation of these materials causes the

metal-metal bonds to break and that subsequent trapping of the metal radicals with an appropriate radical trap (such as molecular oxygen or a carbon-chlorine bond) leads to net backbone cleavage (Scheme A.1).[8] The degradation reactions of these polymers can be conveniently monitored spectroscopically using the metal-metal bond chromophore. The degradation kinetics typically follow a biphasic decay in which there is a short, nonlinear component and a longer-lived, slowly evolving linear component.[2,7,12] This biphasic behavior is typical for many polymer photodegradation reactions (not just the polymers containing metal-metal bonds), and it led us to propose a model to explain the biphasic kinetics behavior.[7]

$$\sim\!\!\sim\!\!\sim M\!-\!M\!\sim\!\!\sim\!\!\sim$$

$$\Big\updownarrow h\upsilon$$

$$\sim\!\!\sim\!\!\sim M\cdot + \cdot M\!\sim\!\!\sim\!\!\sim$$

$$\Big\downarrow T$$

$$\sim\!\!\sim\!\!\sim M\!-\!T$$

$$T = O_2,\ R\text{-}Cl$$
$$M = Mo,\ W,\ Fe$$
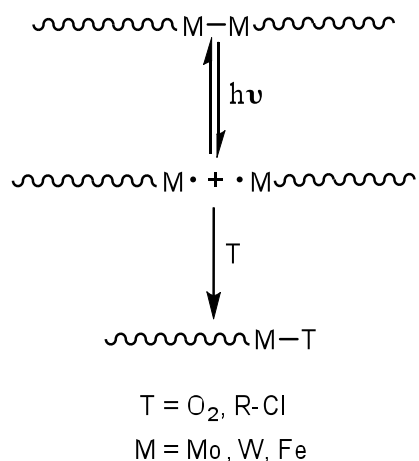
Scheme A.1. Photodegradation of a polymer containing metal-metal bonds in its backbone.

Our model to describe polymer photodegradation kinetics was inspired by Perrin's model of fluorescence decay rates.[13] The Perrin model was originally proposed to explain the nonlinear fluorescence quenching of small molecules embedded in solid

113

polymers, and it posits that the fluorescent molecules are present in one of two microenvironments (Figure A.1). In one microenvironment, a fluorescence quencher is within the "quenching sphere" of the excited molecule and this leads to quenching. In the second microenvironment, no quencher molecule is inside the quenching sphere, and no quenching will occur because diffusion into the quenching sphere is slow compared to the lifetime of the excited state.[13] The biphasic kinetics is attributed to the combination of the fast initial decay of the fluorescence due to quenchers within the quenching sphere and the slower decay that is attributed to the natural lifetime of the excited species that are in the microenvironment with no quencher.[7]

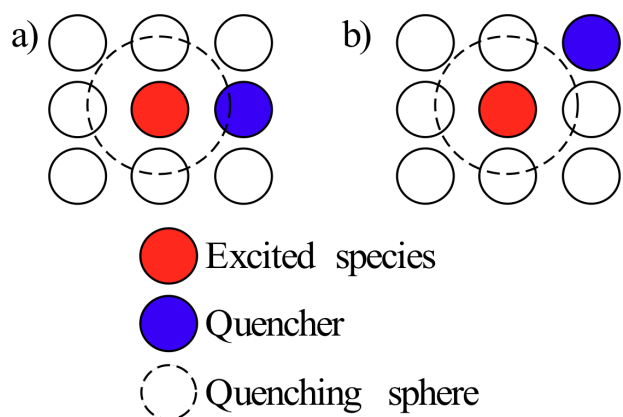**Figure A.1.** Physical description of the Perrin-like kinetic model (a) with the quencher in the quenching sphere and (b) with the quencher outside the quenching sphere.[7]

In our model of polymer photodegradation kinetics, the excited fluorescent species of the Perrin model is conceptually replaced by the photogenerated radicals, and radical traps replace the quencher molecules. Analogous to the Perrin model, the radicals

114

can exist in one of two environments (Figure A.2). In one microenvironment, a radical trap is present in the "reaction sphere" of the radical, and in the other microenvironment, no trap is present in the reaction sphere of the radical. To account for the slower (linear) part of the biphasic decay, it was proposed that diffusion of a trap into the reaction sphere during the lifetime of the radical occurred. A potential problem with this proposal is that diffusion is slow in the solid state and the lifetime of the radicals is short. For example, molybdenum radicals similar to those embedded in the polymer backbones can recombine in solution with a time constant on the order of 5 ps, as determined by ultrafast spectroscopy.[9] Consequently, diffusion of a trap into the reactive sphere of a radical may not be possible during the short lifetime of the metal radicals.

After publication of our model, Professor M. Tachiya suggested to us in a personal communication that a model involving a Poisson distribution of radical/trap environments (not just two) could account for the biphasic kinetics.[14,15] An important feature of Tachiya's suggestion is that it is not necessary to postulate that diffusion of a trap into the reaction sphere of the radical occurs during the lifetime of the radical in order to get biphasic behavior. In this note, we discuss the application of the Tachiya model to solid-state polymer photodegradation, and we compare the Tachiya model to the Perrin-like model. The material in this appendix was co-authored with Dr. David R. Tyler who acted as my advisor during this investigation, Dr. Bevin Daglen who performed much of the experimental research, and Dr. M. Tachiya who initiated this modeling investigation.

115
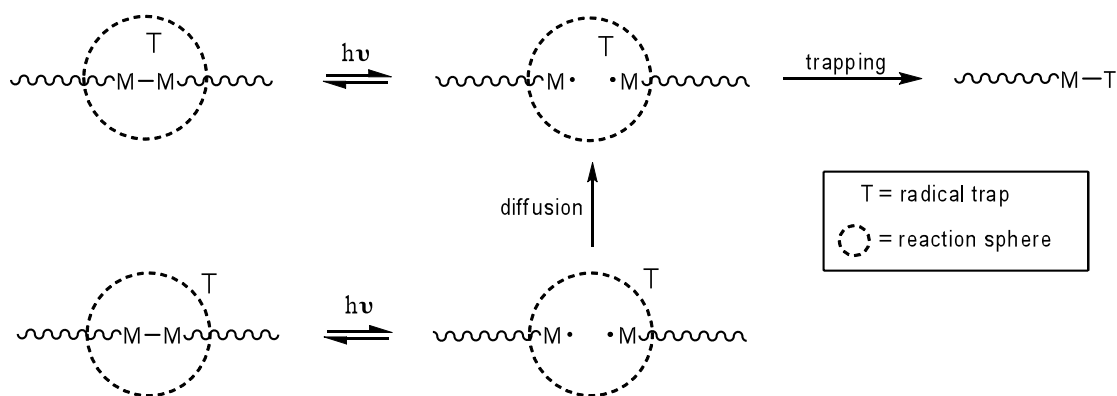
Figure A.2. Mechanistic description of the photodegradation of polymers according to the Perrin-like model.

A.2. EXPERIMENTAL SECTION

The polymer materials and experimental setup used to monitor photodegradation have been described previously.[7,10] Polyurethane and poly (vinyl chloride) (PVC) polymer samples containing molybdenum-molybdenum (Mo-Mo) bonds, polymers **1** and **2** (Figure A.3), were prepared according to literature procedure.[5,16] Irradiation of the polymers was carried out at 532 nm with a 200 W mercury arc lamp or a 5 mW frequency-doubled Nd:YAG laser to induce cleavage of the Mo-Mo bonds. The photodegradation process was monitored using an Oriel Merlin radiometry instrument described elsewhere.[10] The sample temperatures were regulated and transmittance of the samples was monitored at 3 s intervals over 50 min. Several scans were taken across the

sample films for reproducibility. The data were fit to the Perrin-like model[7] and to the

Tachiya model using Igor-ProCarbon software.

1

2

Figure A.3. Photoactive polymers used for photodegradation studies. Polymer 1 is a crosslinked PVC and polymer 2 is a polyurethane with a mixture of rigid and flexible linkages.

A.3. RESULTS AND DISCUSSION

The decay curves for the photochemical degradation of polymers **1** and **2** showed

biphasic behavior.[7] As summarized in the Introduction section, our original explanation

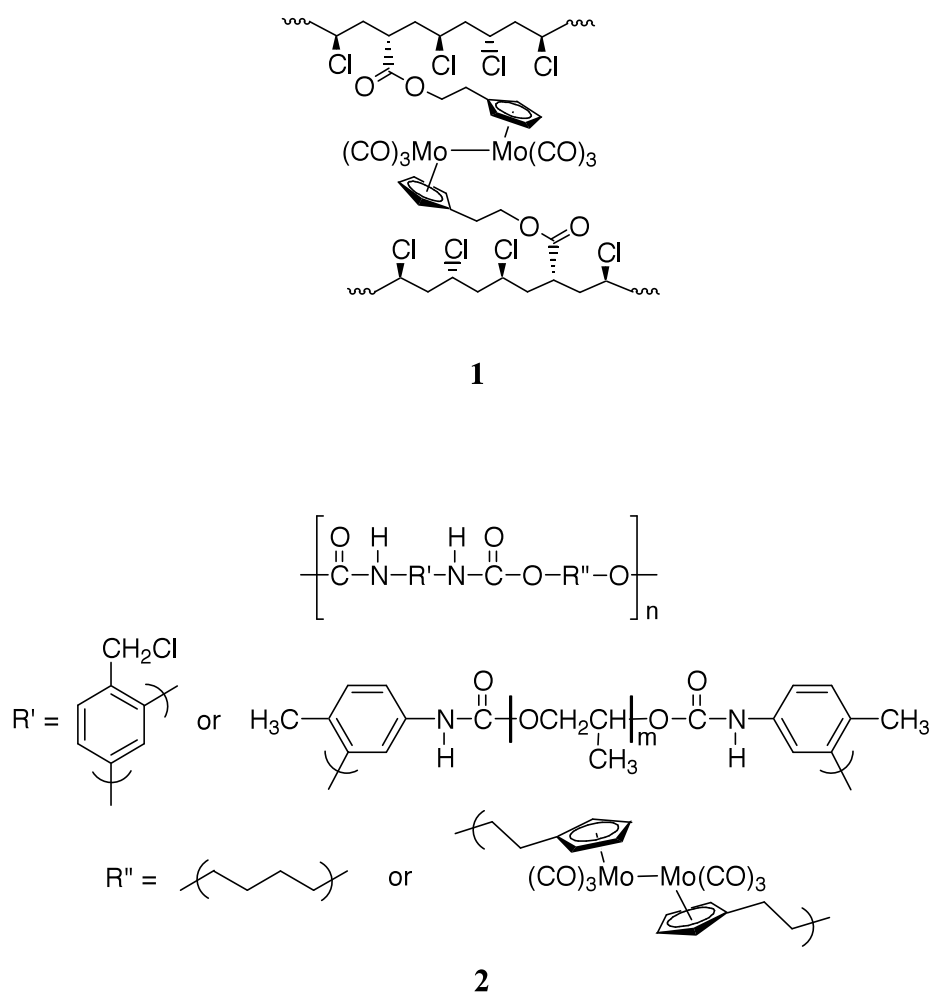for the observed biphasic photochemical degradation kinetics was based on a Perrin-like

model (Figure A.2).[7] Analysis of this model led to the rate expression in eq 1 where P

denotes the concentration of Mo-Mo bonds, k_1 and k_2 are constants, and X_0 and Y_0

represent the initial concentrations of Mo-Mo bonds in the two different

microenvironments. (Note that the observed rate of polymer degradation is the sum of

the rates for the radical trapping reactions in the two microenvironments.) Results of the

fits of the photodegradation traces for polymers **1** and **2** to eq 1 were previously reported

and they were quite good. [7]

$$[P] = X_0 - k_1 t + Y_0 e^{-k_2 t} \tag{1}$$

As mentioned in the introduction, a potential problem with the Perrin-like

mechanism is that diffusion of a trap into the reactive sphere of a radical may not be

possible during the short radical lifetime. To avoid this problem, yet still have biphasic

degradation kinetics, we propose an alternative mechanism based on the kinetics analysis

of fluorescence quenching by M. Tachiya.[14,15] The mechanism is outlined in eqs 2-4.

118

Note that, in this alternative mechanism, metal-metal bonds can only react if they have a trap in their reaction sphere *before* photolysis.

$$M_n\text{—}M_m \; + \; T \; \underset{}{\overset{\text{diffusion}}{\rightleftharpoons}} \; (M_n\text{—}M_m , T) \tag{2}$$

$$(M_n\text{—}M_m , T) \; \xrightarrow{h\nu} \; (M_n{}^\bullet , {}^\bullet M_m , T) \tag{3}$$

$$(M_n{}^\bullet , {}^\bullet M_m , T) \; \longrightarrow \; M_n\text{—}T \; + \; {}^\bullet M_m \tag{4}$$
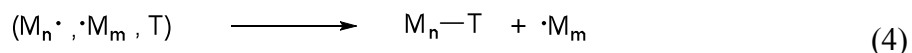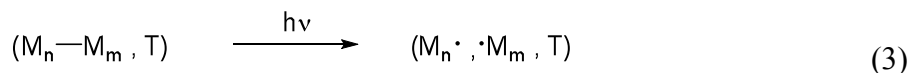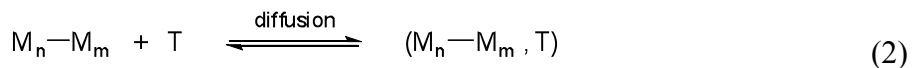
The kinetics analysis of this mechanism is analogous to a model originally developed by Tachiya to describe the luminescence quenching of excited species in micelles.[14,15] This model is shown in eqs 5 and 6. In these equations, $P_n{}^*$ stands for a micelle that contains an excited molecule and n quencher molecules, and T represents a quencher molecule.

$$P_n{}^* \; + \; T \; \underset{(n+1)k_-}{\overset{k_+}{\rightleftharpoons}} \; P_{n+1}{}^* \tag{5}$$

$$P_n{}^* \; + \; T \; \xrightarrow{nk_q} \; P_n \tag{6}$$
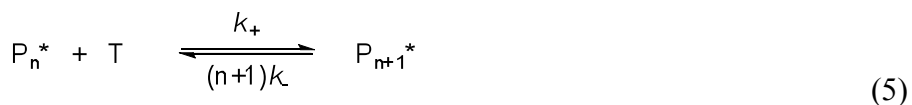
When applied to the mechanism in eqs 2-4, the symbol $P_n{}^*$ stands for the concentration of metal-metal bonds that have n radical traps within a volume V around each metal-metal bond, and the symbol T stands for a radical trap molecule. Equation 5

119

describes the entry and exit of a radical trap into and out of the volume V around the metal-metal bond. Equation 6 describes the process in which the metal-metal bond is cleaved with visible light and the resulting metal radical is captured by a radical trap. In his analysis of this mechanism, Tachiya arrived at two important conclusions. First, the distribution of the number of radical traps in the volume V around each metal-metal bond obeys a Poisson distribution. (See equation 8 of reference 15.) Second, the concentration of P* is given by the expression in eq 7, where k_q and k_- are the rate constants defined in equations 5 and 6 and n_{bar} is the average number of radical traps in the volume V.

$$\frac{P^*(t)}{P^*(0)} = \exp\left\{-\left[\frac{k_- k_q n_{bar}}{(k_- + k_q)}t\right] - \left[\frac{k_q^2 n_{bar}}{(k_- + k_q)^2}\right]\left[1 - e^{-(k_- + k_q)t}\right]\right\} \qquad (7)$$

Equation 7 was used to fit the photodegradation curves of polymers **1** and **2**. The resulting fits are shown in Figures 4 and 5 for temperatures ranging from 25-50°C. It is clear from both Figures A.4 and A.5 that the Tachiya model fits the data extremely well. Although an excellent fit in and of itself is not evidence for a mechanism, the pathway in eqs 2-4 avoids the need to have a step involving diffusion of a trap to a short-lived radical. The Tachiya mechanism seems more likely in this regard.

Figure A.4. Relative Mo-Mo concentration as a function of irradiation time at various temperatures for polymer **1** with fits to the Tachiya model (eq 7). The temperatures for each run are denoted in the plot.
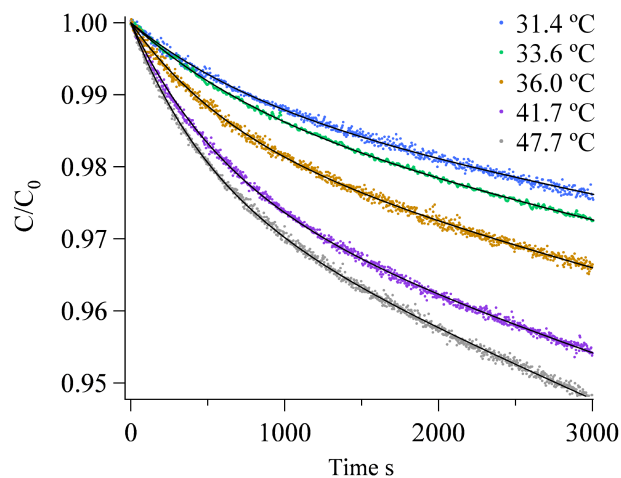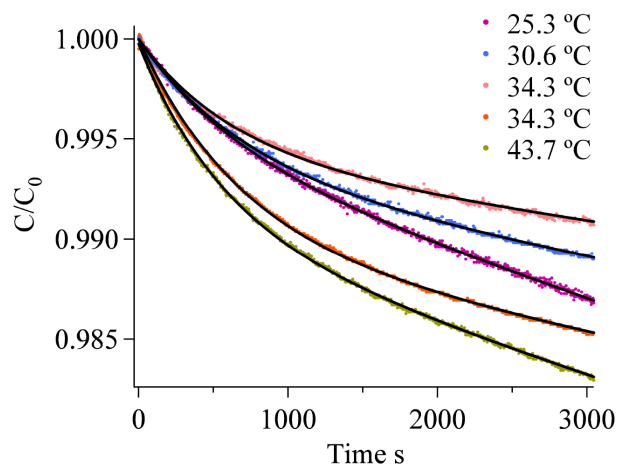

Figure A.5. Relative Mo-Mo concentration as a function of irradiation time at various temperatures for polymer **2** with fits to the Tachiya model (eq 7). The temperatures for each run are denoted in the plot.

121

Comparison of the Perrin-like and Tachiya fits provides further insights. Data for the first few minutes of several representative photodegradation reactions are plotted in Figure A.6. The corresponding fits for the Tachiya and Perrin-like models are also shown. Note that the Tachiya model fits the data more closely at these short times. In contrast, the Perrin-like model slightly underestimates the population of intact metal-metal bonds at the onset of the decay curve. In other words, the Perrin-like model overestimates the amount of initial radical trapping that occurs.   A very qualitative explanation of this result may be that the two-state Perrin model is less responsive than the Tachiya model, which has a continuum of trap distributions (a Poisson distribution) and is therefore able to fit the data better. (It is noted that Dorrance and Hunter showed that the distribution of quenching molecules (in our case radical traps) in kinetic models is an important parameter in describing the kinetics of systems.[17]) Although Figure 6 does show that the Perrin-like model overestimates the amount of initial photodegradation, this is true only for the first few minutes. At longer times, the Perrin-like model fits the data well.
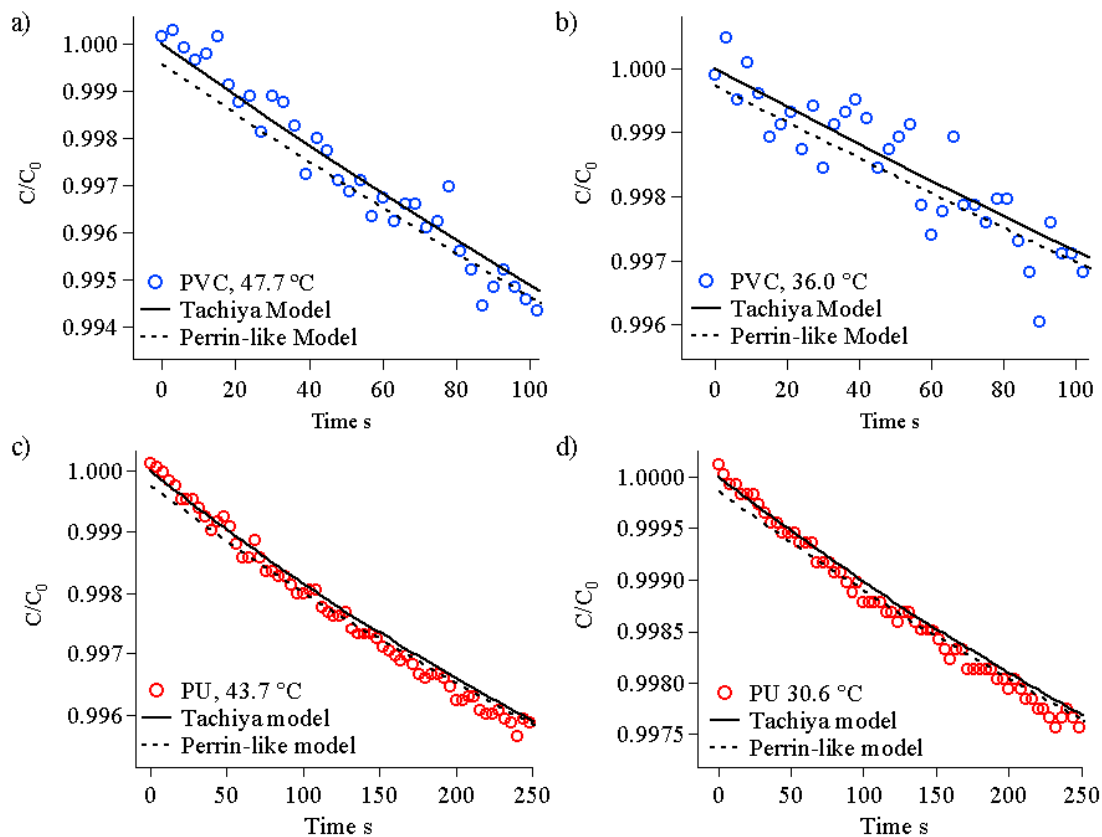
Figure A.6. Example comparisons of the Tachiya and Perrin-like models at early times fit to the degradation of Polymer **1** at (a) 47.7 °C and (b) 36.0 °C and Polymer **2** at (c) 43.7 °C and (d) 30.6°C.

A.4. CONCLUSIONS

In summary, the biphasic kinetics of a typical photochemical degradation reaction of a polymer can be interpreted using either a Perrin-like kinetics model (Figure 2) or a Tachiya-like model (eqs 2-4). The former model invokes a mechanism in which photoproduced radicals are formed in one of two microenvironments. In one microenvironment, a radical trap is present in the reaction sphere of the radical and in the

other microenvironment, no trap is present. In contrast, analysis of the Tachiya model

shows a Poisson distribution of radical traps around the radical. The Tachiya model

gives better fits to the experimental kinetics data at short reaction times. Although a

better fit does not necessarily favor the Tachiya model, from a mechanistic viewpoint the

Tachiya model would seem to be more likely because it does not require diffusion of a

radical trap to the short-lived radical, a process that would be slow in the solid-state in

comparison to the lifetime of the radical.

REFERENCES CITED

CHAPTER I

(1)   *International Energy Outlook Report 2010*; US Department of Energy.

(2)   Lewis, N. S. *Science* **2007**, *315*, 798 -801.

(3)   Shockley, W.; Queisser, H. J. *J. Appl. Phys.* **1961**, *32*, 510-519.

(4)   Sze, S. M. *Semiconductor Devices: Physics and Technology, 2nd Edition*; 2nd ed. Wiley, 2001.

(5)   Beard, M. C.; Ellingson, R. J. *Laser & Photonics Reviews* **2008**, *2*, 377-399.

(6)   Green, M. A. Emery, K. Hishikawa, Y.; Warta, W. *Progress in Photovoltaics: Research and Applications* **2010**, *18*, 346-352.

(7)   Vos, A. D. *J. Phys. D: Appl. Phys.* **1980**, *13*, 839-846.

(8)   Green, M. A. *Progress in Photovoltaics: Research and Applications* **2001**, *9*, 123-135.

(9)   Hanna, M. C. Lu, Z.; Nozik, A. J. *AIP Conf. Proc.* **1997**, *404*, 309-316.

(10)   Ross, R. T.; Nozik, A. J. *J. Appl. Phys.* **1982**, *53*, 3813-3818.

(11)   Prabhu, S. S. Vengurlekar, A. S. Roy, S. K.; Shah, J. *Phys. Rev. B* **1995**, *51*, 14233.

(12)   Yagi, S. Oshima, R.; Okada, Y. In *2009 34th IEEE Photovoltaic Specialists Conference (PVSC)*; IEEE, 2009; pp. 000530-000533.

(13)   Shrestha, S. K. Aliberti, P.; Conibeer, G. J. *Solar Energy Materials and Solar Cells* **2010**, *94*, 1546-1550.

(14)   O'Dwyer, M. F. Humphrey, T. E. Lewis, R. A.; Zhang, C. *Microelectronics Journal* **March**, *39*, 656-659.

(15)   Conibeer, G. J. Jiang, C.-W. König, D. Shrestha, S. Walsh, T.; Green, M. A. *Thin Solid Films* **2008**, *516*, 6968-6973.

(16)   Nozik, A. J. *Inorg. Chem.* **2005**, *44*, 6893-6899.

(17)   Nozik, A. J. *Physica E: Low-dimensional Systems and Nanostructures* **2002**, *14*, 115-120.

(18)   Klimov, V. I. *J. Phys. Chem. B* **2006**, *110*, 16827-16845.

(19)   Klimov, V. I. *Semiconductor and Metal Nanocrystals: Synthesis and Electronic and Optical Properties*; 1st ed. CRC Press, 2003.

(20)   Kolodinski, S. Werner, J H. Wittchen, T.; Queisser, H. J. *Appl. Phys. Lett.* **1993**, *63*, 2405-2407.

(21)   Schaller, R. D. Agranovich, V. M.; Klimov, V. I. *Nat. Phys.* **2005**, *1*, 189-194.

(22)   Klimov, V. I. *J. Phys. Chem. B* **2000**, *104*, 6112-6123.

(23)   Klimov, V. I. *J. Phys. Chem. B* **2006**, *110*, 16827-16845.

(24)   Nozik, A. J. *Nano Letters* **2010**, *10*, 2735-2741.

(25)   Franceschetti, A. An, J. M.; Zunger, A. *Nano Letters* **2006**, *6*, 2191-2195.

(26)   Zemke, J. M. Novet, T. E.; Tyler, D. R. *Can. J. Chem.* **2011**, *89*, 339-346.

(27)   Trinh, M. T. Houtepen, A. J. Schins, J. M. Hanrath, T. Piris, J. Knulst, W. Goossens, A. P. L. M.; Siebbeles, L. D. A. *Nano Letters* **2008**, *8*, 1713-1718.

(28)   Sykora, M. Koposov, A. Y. McGuire, J. A. Schulze, R. K. Tretiak, O. Pietryga, J. M.; Klimov, V. I. *ACS Nano* **2010**, *4*, 2021-2034.

(29)   Schaller, R. D. Sykora, M. Pietryga, J. M.; Klimov, V. I. *Nano Letters* **2006**, *6*, 424-429.

(30)   Nair, G. Geyer, S. M. Chang, L.-Y.; Bawendi, M. G. *Phys. Rev. B* **2008**, *78*, 125325.

(31)   Nair, G.; Bawendi, M. G. *Phys. Rev. B* **2007**, *76*, 081304.

(32)   Murphy, J. E. Beard, M. C. Norman, A. G. Ahrenkiel, S. P. Johnson, J. C. Yu, P. Mićić, O. I. Ellingson, R. J.; Nozik, A. J. *J. Am. Chem. Soc.* **2006**, *128*, 3241-3247.

(33)   McGuire, J. A. Sykora, M. Joo, J. Pietryga, J. M.; Klimov, V. I. *Nano Letters* **2010**, *10*, 2049-2057.

(34)   Luther, J. M. Beard, M. C. Song, Q. Law, M. Ellingson, R. J.; Nozik, A. J. *Nano Letters* **2007**, *7*, 1779-1784.

(35)   Gachet, D. Avidan, A. Pinkas, I.; Oron, D. *Nano Letters* **2010**, *10*, 164-170.

(36)   Ellingson, R. J. Beard, M. C. Johnson, J. C. Yu, P. Micic, O. I. Nozik, A. J. Shabaev, A.; Efros, A. L. *Nano Letters* **2005**, *5*, 865-871.

(37)   Beard, M. C. Midgett, A. G. Law, M. Semonin, O. E. Ellingson, R. J.; Nozik, A. J. *Nano Letters* **2009**, *9*, 836-845.

(38)   Pijpers, J. J. H. Hendry, E. Milder, M. T. W. Fanciulli, R. Savolainen, J. Herek, J. L. Vanmaekelbergh, D. Ruhman, S. Mocatta, D. Oron, D. Aharoni, A. Banin, U.; Bonn, M. *J. Phys. Chem. C* **2008**, *112*, 4783-4784.

(39)   Pijpers, J. J. H. Hendry, E. Milder, M. T. W. Fanciulli, R. Savolainen, J. Herek, J. L. Vanmaekelbergh, D. Ruhman, S. Mocatta, D. Oron, D. Aharoni, A. Banin, U.; Bonn, M. *J. Phys. Chem. C* **2007**, *111*, 4146-4152.

(40)   Schaller, R. D. Pietryga, J. M.; Klimov, V. I. *Nano Letters* **2007**, *7*, 3469-3476.

(41)   Ben-Lulu, M. Mocatta, D. Bonn, M. Banin, U.; Ruhman, S. *Nano Letters* **2008**, *8*, 1207-1211.

(42)   Gabor, N. M. Zhong, Z. Bosnick, K. Park, J.; McEuen, P. L. *Science* **2009**, *325*, 1367 -1371.

(43)   Zhang, J. Z. *Acc. Chem. Res.* **1997**, *30*, 423-429.

(44)   Guyot-Sionnest, P. Wehrenberg, B.; Yu, D. *J. Chem. Phys.* **2005**, *123*, 074709.

(45)   Patel, A. A. Wu, F. Zhang, J. Z. Torres-Martinez, C. L. Mehra, R. K. Yang, Y.; Risbud, S. H. *J. Phys. Chem. B* **2000**, *104*, 11598-11605.

(46)   Tyagi, P.; Kambhampati, P. *J. Chem. Phys.* **2011**, *134*, 094706.

(47)   McGuire, J. A. Joo, J. Pietryga, J. M. Schaller, R. D.; Klimov, V. I. *Acc. Chem. Res.* **2008**, *41*, 1810-1819.

(48)   Sykora, M. Koposov, A. Y. McGuire, J. A. Schulze, R. K. Tretiak, O. Pietryga, J. M.; Klimov, V. I. *ACS Nano* **2010**, *4*, 2021-2034.

(49)   Padilha, L. A. Robel, I. Lee, D. C. Nagpal, P. Pietryga, J. M.; Klimov, V. I. *ACS Nano* **0**, *0*.

(50)   Knowles, K. E. Tice, D. B. McArthur, E. A. Solomon, G. C.; Weiss, E. A. *J. Am. Chem. Soc.* **2010**, *132*, 1041-1050.

(51) Dubois, F. Mahler, B. Dubertret, B. Doris, E.; Mioskowski, C. *J. Am. Chem. Soc.* **2007**, *129*, 482-483.

(52) Gehl, B. Aleksandrovic, V. Erbacher, M. Jürgens, B. Schürenberg, M. Kornowski, A. Weller, H.; Bäumer, M. *ChemPhysChem* **2008**, *9*, 821-825.

(53) Woehrle, G. H. Brown, L. O.; Hutchison, J. E. *J. Am. Chem. Soc.* **2005**, *127*, 2172-2183.

(54) Sun, S. Murray, C. B. Weller, D. Folks, L.; Moser, A. *Science* **2000**, *287*, 1989 - 1992.

(55) Algar, W. R.; Krull, U. J. *ChemPhysChem* **2007**, *8*, 561-568.

(56) Beard, M. C. Midgett, A. G. Law, M. Semonin, O. E. Ellingson, R. J.; Nozik, A. J. *Nano Letters* **2009**, *9*, 836-845.

(57) Sambur, J. B. Novet, T.; Parkinson, B. A. *Science* **2010**, *330*, 63 -66.

(58) Moody, I. S. Stonas, A. R.; Lonergan, M. C. *J. Phys. Chem. C* **2008**, *112*, 19383-19389.

CHAPTER II

(1) Maiman, T. H. *Nature* **1960**, *187*, 493-494.

(2) Miller, D. R. Murnane, M. M. Scherer, N. F.; Weiner, A. M. *Ultrafast Phenomena XIII: Proceedings of the 13th International Conference*; 1st ed. Springer, 2003.

(3) McHale, J. L. *Molecular Spectroscopy*; 1st ed. Prentice Hall, 1998.

(4) *Ultrafast Phenomena XV*; Corkum, P. Jonas, D. M. Miller, R. J. D.; Weiner, A. M., Eds. Springer Berlin Heidelberg: Berlin, Heidelberg, 2007; Vol. 88.

(5) Stingl, A. Spielmann, C. Krausz, F.; Szipocs, R. *Opt. Lett.* **1994**, *19*, 204-206.

(6) Steinmeyer, G. Sutter, D. H. Gallmann, L. Matuschek, N.; Keller, U. *Science* **1999**, *286*, 1507 -1512.

(7) Squier, J. Salin, F. Mourou, G.; Harter, D. *Opt. Lett.* **1991**, *16*, 324-326.

(8) Fork, R. L. *Appl. Phys. Lett.* **1981**, *38*, 671.

(9)   Backus, S. Durfee, C. G. Murnane, M. M.; Kapteyn, H. C. *Rev. Sci. Instrum.* **1998**, *69*, 1207.

(10)   Fleming, G. R. *Chemical Applications of Ultrafast Spectroscopy*; Oxford University Press, USA, 1986.

(11)   Stingl, A. Lenzner, M. Spielmann, C. Krausz, F.; Szipocs, R. *Opt. Lett.* **1995**, *20*, 602-604.

(12)   Silfvast, W. T. *Laser Fundamentals*; Cambridge University Press, 1996.

(13)   Moulton, P. F. *J. Opt. Soc. Am. B* **1986**, *3*, 125-133.

(14)   Schafer, F. P. *Dye Lasers*; 3rd ed. Springer-Verlag, 1990.

(15)   Bridges, W. B. *Appl. Phys. Lett.* **1964**, *4*, 128.

(16)   Geusic, J. E. Marcos, H. M.; Van Uitert, L. G. *Appl. Phys. Lett.* **1964**, *4*, 182.

(17)   Rast, H. E. Caspers, H. H.; Miller, S. A. *Phys. Rev.* **1968**, *169*, 705.

(18)   Zhou, J. Taft, G. Huang, C.-P. Murnane, M. M. Kapteyn, H. C.; Christov, I. P. *Opt. Lett.* **1994**, *19*, 1149-1151.

(19)   McClure, D. S. *J. Chem. Phys.* **1962**, *36*, 2757.

(20)   Nelson, E. D. Wong, J. Y.; Schawlow, A. L. *Phys. Rev.* **1967**, *156*, 298.

(21)   Byvik, C.; Buoncristiani A. *IEEE J. Quantum Electron.* **1985**, *21*, 1619- 1624.

(22)   Grinberg, M. Mandelis, A. Fjeldsted, K.; Othonos, A. *Phys. Rev. B* **1993**, *48*, 5922.

(23)   Lamb, W. E. *Phys. Rev.* **1964**, *134*, A1429.

(24)   Hargrove, L. E. Fork, R. L.; Pollack, M. A. *Appl. Phys. Lett.* **1964**, *5*, 4.

(25)   Strickland, D.; Mourou, G. *Opt. Comm.* **1985**, *56*, 219-221.

(26)   Hecht, E. *Optics*; 4th ed. Addison Wesley, 2001.

(27)   Zhang, J.-Y. Huang, J. Y.; Shen, Y. R. *Optical Parametric Generation and Amplification*; CRC Press, 1995.

(28)   Bosenberg, W. R.; Tang, C. L. *Appl. Phys. Lett.* **1990**, *56*, 1819.

(29)   Ziólek, M. Lorenc, M.; Naskrecki, R. *Appl. Phys. B.* **2001**, *72*, 843.

(30) McGuire, J. A. Joo, J. Pietryga, J. M. Schaller, R. D.; Klimov, V. I. *Acc. Chem. Res.* **2008**, *41*, 1810-1819.

(31) McGuire, J. A. Sykora, M. Joo, J. Pietryga, J. M.; Klimov, V. I. *Nano Letters* **2010**, *10*, 2049-2057.

(32) Beard, M. C. Midgett, A. G. Law, M. Semonin, O. E. Ellingson, R. J.; Nozik, A. J. *Nano Letters* **2009**, *9*, 836-845.

CHAPTER III

(1) Hines, M. A.; Scholes, G. D. *Adv. Mater.* **2003**, *15*, 1844-1849.

(2) Murray, C. B.; Sun, S.; Gaschler, W.; Doyle, H.; Betley, T. A.; Kagan, C. R. *IBM Journal of Research and Development* **2001**, *45*, 47-56.

(3) Wehrenberg, B. L. Wang, C.; Guyot-Sionnest, P. *J. Phys. Chem. B* **2002**, *106*, 10634-10640.

(4) Murphy, J. E. Beard, M. C. Norman, A. G. Ahrenkiel, S. P. Johnson, J. C. Yu, P. Mićić, O. I. Ellingson, R. J.; Nozik, A. J. *J. Am. Chem. Soc.* **2006**, *128*, 3241-3247.

(5) Maria, A. Cyr, P. W. Klem, E. J. D. Levina, L.; Sargent, E. H. *Appl. Phys. Lett.* **2005**, *87*, 213112.

(6) Trinh, M. T. Houtepen, A. J. Schins, J. M. Hanrath, T. Piris, J. Knulst, W. Goossens, A. P. L. M.; Siebbeles, L. D. A. *Nano Letters* **2008**, *8*, 1713-1718.

(7) Sykora, M. Koposov, A. Y. McGuire, J. A. Schulze, R. K. Tretiak, O. Pietryga, J. M.; Klimov, V. I. *ACS Nano* **2010**, *4*, 2021-2034.

(8) Schaller, R. D. Sykora, M. Pietryga, J. M.; Klimov, V. I. *Nano Letters* **2006**, *6*, 424-429.

(9) Schaller, R. D. Pietryga, J. M.; Klimov, V. I. *Nano Letters* **2007**, *7*, 3469-3476.

(10) Roberti, T. W. Cherepy, N. J.; Zhang, J. Z. *J. Chem. Phys.* **1998**, *108*, 2143.

(11) Patel, A. A. Wu, F. Zhang, J. Z. Torres-Martinez, C. L. Mehra, R. K. Yang, Y.; Risbud, S. H. *J. Phys. Chem. B* **2000**, *104*, 11598-11605.

(12) Nozik, A. J. *Inorg. Chem.* **2005**, *44*, 6893-6899.

(13)   Nair, G. Geyer, S. M. Chang, L.-Y.; Bawendi, M. G. *Phys. Rev. B* **2008**, *78*, 125325.

(14)   Nair, G.; Bawendi, M. G. *Phys. Rev. B* **2007**, *76*, 081304.

(15)   Luther, J. M. Beard, M. C. Song, Q. Law, M. Ellingson, R. J.; Nozik, A. J. *Nano Letters* **2007**, *7*, 1779-1784.

(16)   Klimov, V. I. *J. Phys. Chem. B* **2006**, *110*, 16827-16845.

(17)   Gachet, D. Avidan, A. Pinkas, I.; Oron, D. *Nano Letters* **2010**, *10*, 164-170.

(18)   Ellingson, R. J. Beard, M. C. Johnson, J. C. Yu, P. Micic, O. I. Nozik, A. J. Shabaev, A.; Efros, A. L. *Nano Letters* **2005**, *5*, 865-871.

(19)   Ben-Lulu, M. Mocatta, D. Bonn, M. Banin, U.; Ruhman, S. *Nano Letters* **2008**, *8*, 1207-1211.

(20)   Beard, M. C. Midgett, A. G. Law, M. Semonin, O. E. Ellingson, R. J.; Nozik, A. J. *Nano Letters* **2009**, *9*, 836-845.

(21)   Beard, M. C. Knutsen, K. P. Yu, P. Luther, J. M. Song, Q. Metzger, W. K. Ellingson, R. J.; Nozik, A. J. *Nano Letters* **2007**, *7*, 2506-2512.

(22)   Zhang, J. Z. *Acc. Chem. Res.* **1997**, *30*, 423-429.

(23)   Guyot-Sionnest, P. Wehrenberg, B.; Yu, D. *J. Chem. Phys.* **2005**, *123*, 074709.

(24)   Moody, I. S. Stonas, A. R.; Lonergan, M. C. *J. Phys. Chem. C* **2008**, *112*, 19383-19389.

(25)   McGuire, J. A. Joo, J. Pietryga, J. M. Schaller, R. D.; Klimov, V. I. *Acc. Chem. Res.* **2008**, *41*, 1810-1819.

(26)   Stouwdam, J. W. Shan, J. van Veggel, F. C. J. M. Pattantyus-Abraham, A. G. Young, J. F.; Raudsepp, M. *J. Phys. Chem. C* **2007**, *111*, 1086-1092.

(27)   Sengupta, A. Jiang, B. Mandal, K. C.; Zhang, J. Z. *J. Phys. Chem. B* **1999**, *103*, 3128-3137.

CHAPTER IV

(1) Maria, A. Cyr, P. W. Klem, E. J. D. Levina, L.; Sargent, E. H. *Appl. Phys. Lett.* **2005**, *87*, 213112.

(2) Hines, M. A.; Scholes, G. D. *Adv. Mater.* **2003**, *15*, 1844-1849.

(3) Wang, W. Chen, X.; Efrima, S. *J. Phys. Chem. B* **1999**, *103*, 7238-7246.

(4) Tian, Y.; Fendler, J. H. *Chem. Mater.* **1996**, *8*, 969-974.

(5) Liu, J. Yu, H. Wu, Z. Wang, W. Peng, J.; Cao, Y. *Nanotechnology* **2008**, *19*, 345602.

(6) Smith, A. M. Duan, H. Rhyner, M. N. Ruan, G.; Nie, S. *Phys. Chem. Chem. Phys.* **2006**, *8*, 3895.

(7) Chen, S.; Liu, W. *Mater. Chem. Phys.* **2006**, *98*, 183-189.

(8) Moody, I. S. Stonas, A. R.; Lonergan, M. C. *J. Phys. Chem. C* **2008**, *112*, 19383-19389.

(9) McDonald, S. A. Konstantatos, G. Zhang, S. Cyr, P. W. Klem, E. J. D. Levina, L.; Sargent, E. H. *Nat. Mater.* **2005**, *4*, 138-142.

(10) Xu, J. Cui, D. Zhu, T. Paradee, G. Liang, Z. Wang, Q. Xu, S.; Wang, A. Y. *Nanotechnology* **2006**, *17*, 5428-5434.

(11) Sambur, J. B. Novet, T.; Parkinson, B. A. *Science* **2010**, *330*, 63 -66.

(12) Beard, M. C. Midgett, A. G. Law, M. Semonin, O. E. Ellingson, R. J.; Nozik, A. J. *Nano Letters* **2009**, *9*, 836-845.

(13) Knowles, K. E. Tice, D. B. McArthur, E. A. Solomon, G. C.; Weiss, E. A. *J. Am. Chem. Soc.* **2010**, *132*, 1041-1050.

(14) Woehrle, G. H. Brown, L. O.; Hutchison, J. E. *J. Am. Chem. Soc.* **2005**, *127*, 2172-2183.

(15) Dubois, F. Mahler, B. Dubertret, B. Doris, E.; Mioskowski, C. *J. Am. Chem. Soc.* **2007**, *129*, 482-483.

(16) García Ruano, J. L. Parra, A.; Alemán, J. *Green Chem.* **2008**, *10*, 706.

CHAPTER V

(1)   Beard, M. C. Midgett, A. G. Law, M. Semonin, O. E. Ellingson, R. J.; Nozik, A. J. *Nano Letters* **2009**, *9*, 836-845.

(2)   Guyot-Sionnest, P. Wehrenberg, B.; Yu, D. *J. Chem. Phys.* **2005**, *123*, 074709.

(3)   Zemke, J. M. Novet, T. E.; Tyler, D. R. *Can. J. Chem.* **2011**, *89*, 339-346.

(4)   Patel, A. A. Wu, F. Zhang, J. Z. Torres-Martinez, C. L. Mehra, R. K. Yang, Y.; Risbud, S. H. *J. Phys. Chem. B* **2000**, *104*, 11598-11605.

(5)   Yuan, Z. Lu, W. Liu, W.; Hao, J. *Soft Matter* **2008**, *4*, 1639.

(6)   Hines, M. A.; Scholes, G. D. *Adv. Mater.* **2003**, *15*, 1844-1849.

(7)   Moody, I. S. Stonas, A. R.; Lonergan, M. C. *J. Phys. Chem. C* **2008**, *112*, 19383-19389.

(8)   McGuire, J. A. Sykora, M. Joo, J. Pietryga, J. M.; Klimov, V. I. *Nano Letters* **2010**, *10*, 2049-2057.

(9)   Moreels, I. Justo, Y. De Geyter, B. Haustraete, K. Martins, J. C.; Hens, Z. *ACS Nano* **2011**, *5*, 2004-2012.

(10) Ellingson, R. J. Beard, M. C. Johnson, J. C. Yu, P. Micic, O. I. Nozik, A. J. Shabaev, A.; Efros, A. L. *Nano Letters* **2005**, *5*, 865-871.

(11) Zumdahl, S. S.; Zumdahl, S. A. *Chemistry*; 7th ed. Brooks Cole, 2007.

(12) Shriver, D. *Shriver and Atkins Inorganic Chemistry*; 4th ed. Oxford University Press, 2006.

(13) Miessler, G. L.; Tarr, D. A. *Inorganic Chemistry*; 3rd ed. Prentice Hall, 2003.

APPENDIX A

(1)   Rabek, J. F. *Polymer Photodegradation: Mechanisms and Experimental Methods*; Springer, 1995.

(2)   Rivaton, A. Gardette, J. Mailhot, B.; Morlat-Therlas, S. *Macromol. Symp.* **2005**, *225*, 129-146.

(3)   Schnabel, W. *Polymers and Light: Fundamentals and Technical Applications*; 1st ed. Wiley-VCH, 2007.

(4)   Scott, G.; Gilead, D. *Degradable Polymers: Principles and Applications*; Springer, 1995.

(5)   Daglen, B. Harris, J.; Tyler, D. *J. Inorg. Organomet. Poly. Mat.* **2007**, *17*, 267-274.

(6)   Daglen, B.; Tyler, D. *J. Inorg. Organomet. Poly. Mat.* **2009**, *19*, 91-97.

(7)   Daglen, B. C.; Tyler, D. R. *Macromolecules* **2008**, *41*, 9525-9531.

(8)   Tenhaeff, S. C.; Tyler, D. R. *Organometallics* **1991**, *10*, 473-482.

(9)   Oelkers, A. B. Scatena, L. F.; Tyler, D. R. *J. Phys. Chem. A* **2007**, *111*, 5353-5360.

(10)   Daglen, B. C. Harris, J. D. Dax, C. D.; Tyler, D. R. *Rev. Sci. Instrum.* **2007**, *78*, 074104.

(11)   Tyler, D. R. *Coord. Chem. Rev.* **2003**, *246*, 291-303.

(12)   Hwu, J. R.; King, K. Y. *Chem. Eur. J.* **2005**, *11*, 3805-3815.

(13)   Perrin, J. F. *Compt. Rend.* **1924**, 1978-1980.

(14)   Tachiya, M. *J. Chem. Phys.* **1982**, *76*, 340.

(15)   Tachiya, M. *Chem. Phys. Lett.* **1975**, *33*, 289-292.

(16)   Chen, R. Meloy, J. Daglen, B. C.; Tyler, D. R. *Organometallics* **2005**, *24*, 1495-1500.

(17)   Dorrance, R. C.; Hunter, T. F. *J. Chem. Soc., Faraday Trans. 1:* **1972**, *68*, 1312.